Design, Fabrication and Characterisation of Improved Tip-Enhanced Raman Spectroscopy Probes

Luke R. McCourt
B.Sci(Phys)(Hons)

A thesis submitted in fulfilment of the requirements for the degree of

Doctorate of Philosophy

School of Engineering
The University of Newcastle, Australia

May, 2022

This research was supported by an Australian Government Research Training Program (RTP) Scholarship

Statement of Originality

I hereby certify that the work embodied in the thesis is my own work, conducted under normal supervision. The thesis contains no material which has been accepted, or is being examined, for the award of any other degree or diploma in any university or other tertiary institution and, to the best of my knowledge and belief, contains no material previously published or written by another person, except where due reference has been made. I give consent to the final version of my thesis being made available worldwide when deposited in the University's Digital Repository, subject to the provisions of the Copyright Act 1968 and any approved embargo.

	31-5-2022
Luke R. McCourt	Date

Statement of Collaboration

I hereby certify that the work embodied in this thesis contains publications of which I am a joint author. I have included as part of the thesis a written declaration endorsed in writing by my supervisor, attesting to my contribution to the joint publications.

	31-5-2022
Luke R. McCourt	Date

By signing below I confirm that Luke R. McCourt contributed to the publications as described within the thesis.

	31-5-2022
Andrew J. Fleming	Date

Acknowledgements

I would like to thank my supervisors, Prof. Andrew Fleming, Dr. Michael Ruppert, Dr. Ben Routley, Assoc. Prof. Vicki Keast and Assoc. Prof. John Holdsworth for their guidance. I would also like to thank Dr. David Harcombe for assisting with the final proofreading, Dr. Sathish Clastinrusselraj Indirathankam for assisting with imaging and Dr. Renee Goreham for assisting with carbon nanotube sample preparation. Finally, I would like to thank my parents Robert and Leanne for their support throughout my education.

Contents

List of Publications

The research presented in this thesis has resulted in the following publications:

Journal Articles:

1. L. R. McCourt, M. G. Ruppert, B. S. Routley, S. C. Indirathankam, and A. J. Fleming, "A comparison of gold and silver nanocones and geometry optimisation for tip-enhanced microscopy," *Journal of Raman Spectroscopy*, vol. 51, no. 11, pp. 2208–2216, 2020.

2. L. R. McCourt, B. S. Routley, M. G. Ruppert, V. J. Keast, CI Sathish, R. Borah, R. V. Goreham, A. J. Fleming, "Single-walled carbon nanotubes as: One-dimensional scattering surfaces for measuring point spread functions and performance of tip-enhanced Raman spectroscopy probes," *ACS Applied Nanomaterials*, vol. 5, no. 7, pp. 9024–9033, 2022.

3. L. R. McCourt, B. S. Routley, M. G. Ruppert, A. J. Fleming, "Gold nanocones for collocated tip-enhanced Raman spectroscopy and atomic force microscope imaging," *Journal of Raman Spectroscopy*, Submitted.

4. M. G. Ruppert, B. S. Routley, L. R. McCourt, Y. K. Yong , A. J. Fleming, "Modulated-illumination intermittent-contact tip-enhanced Raman spectroscopy: Simultaneous imaging of surface and material properties," *Nature Communications*, Submitted.

5. N. Yadav, V. Patel, L. McCourt, M. Ruppert, M. Miller, T. Inerbaev, S. Mahasivam, A. Vinu, S. Singh, and A. S. Karakoti, "Tuning the enzyme-like activities of cerium oxide nanoparticles using triethyl phosphite ligand," *Biomaterials Science*, 2022.

6. C. Fang, Z. Sobhani, X. Zhang, L. McCourt, B. Routley, C. T. Gibson, and R. Naidu, "Identification and visualisation of microplastics / nanoplastics by Raman imaging (iii): Algorithm to cross-check multi-images," *Water Research*, vol. 194, p. 116913, Apr. 2021.

Conference Presentations:

1. L. R. McCourt, "Resolution and enhancement of probes for nearfield two photon apertureless lithography," in *Nanophotonics and Micro/Nano Optics International Conference 2019*, (Munich), p. 197, Sept. 2019.

List of Figures

List of Tables

List of Abbreviations

AFM	Atomic Force Microscopy
Ag	Silver
Au	Gold
BEM	Boundary Element Method
CNT	Carbon Nanotube
EDX	Energy-Dispersive X-Ray Spectroscopy
FEB	Focused Electron Beam
FEBID	Focused Electron Beam Induced Deposition
FIB	Focused Ion Beam
FIBID	Focused Ion Beam Induced Deposition
FWHM	Full Width at Half Maximum
LSPR	Localised Surface Plasmon Resonance
MIIC-TERS	Modulated-Illumination Intermittent-Contact Tip-Enhanced Raman Spectroscopy
PSF	Point Spread Function
SEM	Scanning Electron Microscope
SERS	Surface Enhanced Raman Spectroscopy
SWCNT	Single-Walled Carbon Nanotube
TERS	Tip-Enhanced Raman Spectroscopy

Abstract

Probes for tip-enhanced Raman spectroscopy (TERS) are currently constructed from silicon atomic force microscopy (AFM) cantilevers with a grainy silver coating. The grainy coating creates randomly dispersed metal nanoparticles that can concentrate incident light into a volume with a radius on the order of 10 nm. This locally enhanced light enables sub-diffraction limited optical microscopy and Raman spectroscopy; however, a number of issues arise from the random grain formation at the tip apex, including unreliable enhancement, an offset between TERS and AFM maps, suboptimal AFM and TERS resolution, and artefacts in the TERS images. Furthermore, silver probes corrode rapidly in ambient conditions, which limits the effective lifetime to one day or less. These issues significantly limit the performance and practicality of tip-enhanced microscopy and spectroscopy applications.

This thesis investigates the use of gold nanocone probes as an alternative to grainy silver-coated AFM probes. Rather than relying on random grain formation, gold nanocones are fabricated with dimensions that result in surface plasmon resonance at the intended illumination wavelength. Compared to silver coated probes, gold nanocones are chemically stable and result in only one centre of enhancement, which is located at the mechanical apex of the probe. These properties address many of the issues experienced with silver coated probes; however, gold nanocones must be designed to optimise the resolution and enhancement, and the probe fabrication becomes significantly more challenging.

This thesis describes the optical modelling, design, and fabrication of gold nanocone probes for improved tip-enhanced Raman spectroscopy in the visible spectrum. The gold nanocone probes are compared to commercially available TERS probes using a new method for performance measurement, which utilises single-walled carbon nanotubes as 1D scattering objects. Experimental results demonstrate that gold nanocone probes provide higher spatial resolution, artefact-free imaging, longer lifetime, and improved image contrast comparable to grainy silver probes.

The final contribution of this thesis is a new imaging mode for tip-enhanced Raman spectroscopy named modulated-illumination intermittent-contact TERS (MIIC-TERS). This mode combines the high enhancement of contact TERS with the lower shear forces of intermittent contact mode. MIIC-TERS is demonstrated using commercial probes and a gold nanocone probe.

Chapter 1

Introduction

This chapter introduces tip-enhanced Raman spectroscopy, describes the foremost difficulties associated with this technique, and outlines the scope of this thesis.

1.1 Motivation

First discovered in 1928, Raman scattering is a is a weak inelastic scattering of light from molecules where the energy shift between the incident and scattered light depends on vibrational modes, which are unique for a given chemical [1]. Since this discovery, Raman spectroscopy has been widely adopted for chemical identification. Examples include non-destructive substance identification in pharmaceuticals [2], extensive use in biology [3], biomedical sciences [4–6], food science quality control [7], and as a powerful measurement tool during chemical synthesis [8–10]. An issue with Raman spectroscopy is the low probability of Raman scattering occurring, which results in a poor signal-to-noise ratio and requires an intense input beam to overcome [11]. Furthermore, the spatial resolution of Raman spectroscopy is limited by the diffraction-limited spot of the light source.

Surface-enhanced Raman spectroscopy utilises a metal substrate where surface plasmons are excited to amplify the Raman scattering cross-section by orders of magnitude [12] and has been demonstrated to permit single-molecule detection [13]. Thus, surface-enhanced Raman spectroscopy allows significant improvements in the Raman signal-to-noise ratio. However, surface-enhanced Raman spectroscopy is diffraction-limited making it ill-suited to high-resolution microscopy [14].

Tip-enhanced Raman spectroscopy (TERS) is a variation of Raman spectroscopy that allows sub-wavelength resolution imaging. In TERS, surface plasmons are excited at a sharp metal tip that amplifies the Raman scattering intensity in its vicinity [15]. As the scattering enhancement is localised to the tip apex, the resolution of TERS is limited by the tip sharpness [16]. Metal coated atomic force microscope tips with apex diameters less than 20 nm are available and can be used to perform TERS imaging with an approximate resolution of 20 nm [8]. This is well below the approximately 250 nm diffraction limit of a visible light source. Thus, TERS is an ideal technique for producing high-resolution Raman maps of a surface [17]. Raman microscopy,

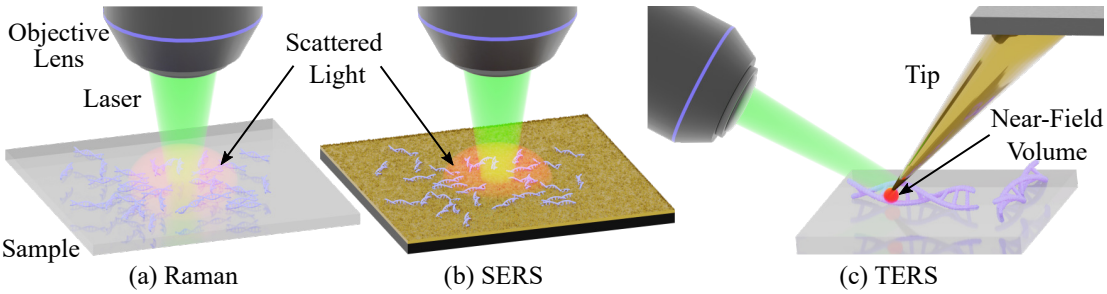

Figure 1.1: Illustrations of Raman spectroscopy modes. (a) Raman spectroscopy where the green, focused laser beam excites sample molecules within the focal volume. The molecules relax, producing low-intensity Raman scattered light shown as the red hemisphere. (b) Surface-enhanced Raman spectroscopy where the Raman enhancement in the focal volume is enhanced using a rough gold substrate. (c) Tip-enhanced Raman spectroscopy where surface plasmons at the tip apex create electromagnetic near-fields at the tip apex. The near-field enhances Raman scatter in the sub-diffraction-limited volume.

SERS and TERS are compared in Figure 1.1.

TERS relies on the excitation of a localised surface plasmon on the metallic tip. Localised surface plasmons are resonant oscillations of conduction electrons that are strongly confined to the surface. The magnitude and resonance wavelength of a localised surface plasmon depends on particle shape, size, surface morphology and material [18]. The Raman enhancement for a TERS probe is proportional to the magnitude of the plasmon resonance. The usable illumination wavelengths for TERS correspond to the resonance wavelength of the surface plasmons. Hence, tip design is paramount to TERS performance [19]. TERS is commonly performed using atomic force microscopy (AFM), which allows precise control over the tip-sample separation as the tip is scanned across the sample.

Commercially available TERS probes are typically made of a silicon AFM tip with a silver coating that forms a grainy surface. The lifetime, Raman signal-to-noise ratio and resolution of these probes are limited by the following issues:

- The silver coating tarnishes rapidly in ambient conditions and may only offer acceptable performance for a few hours or days [20].
- The tips have not been designed to support maximum localised surface plasmon amplitude at a specific illumination wavelength resulting in sub-optimal Raman enhancement.
- The tips typically exhibit inconsistent surface morphology due to the methods of applying the metal coating [21]. This results in inconsistent Raman enhancement with some tips producing no measurable enhancement at all [22]. The rough metal coating will also reduce the spatial resolution for TERS and AFM imaging and introduce an offset between these imaging techniques.

To compare the performance of presently available TERS probes and new probe designs, a repeatable experimental method is required to quantify performance. Current methods for measuring TERS electric field enhancement rely on estimating the spot size of the enhanced field

at the tip apex and assuming a constant Raman enhancement in this volume [23–25]. These approximations introduce uncertainty when measuring and comparing TERS tip performance. An improved measurement method would allow the probe point spread function (PSF) to be measured. Such a method would enable accurate comparisons between TERS probes and aid in the optimisation of future probes.

The work in this thesis will focus on two main objectives:

1. Designing and fabricating improved TERS probes that offer:
    - Improved lifetime through increased chemical stability
    - Improved Raman enhancement and signal-to-noise ratio
    - Improved spatial resolution for TERS and AFM imaging
2. Develop improved experimental methods for characterising tip performance. These methods will be used to verify and compare the performance of new TERS tip designs.

The first objective is achieved by using boundary element simulation to optimise gold nanocone TERS probe geometry. The probes are then fabricated using focused ion beam milling. The second objective is achieved using a novel method for identifying and using single-walled carbon nanotubes as one-dimensional TERS scattering objects to measure the probe PSF.

The proposed probe fabrication methods are expected to improve TERS imaging by providing lower noise and higher resolution TERS imaging. This is beneficial for applications that are limited by signal-to-noise and spatial resolutions, such as single-molecule detection during chemical synthesis, mapping of pathogens and other biological samples, and the detection of contamination in foods. In the following sections, Raman and TERS are introduced in more detail. Issues associated with TERS are discussed and potential solutions are proposed.

1.2 Raman Spectroscopy

Raman spectroscopy is a technique that measures the inelastic scattering of light from the vibrational states of a molecule. First discovered in 1928, Raman scattered light provides chemical information about the sample, allowing it to be identified [26].

Figure 1.2 illustrates three scattering mechanisms that may occur when light strikes a target. Rayleigh scattering (a) occurs when the molecule is excited to a virtual state before relaxing to its initial state. The scattered photon has the same energy as the incident photon, hence the process is elastic. Stokes Raman scattering (b) occurs when a molecule relaxes to a vibrational state higher than its initial state. The molecule has gained energy and hence the scattered photon will have less energy than the incident photon, which manifests as a red-shift. Anti-Stokes Raman scattering (c) occurs when the molecule relaxes to a vibrational state below its initial state, resulting in a scattered photon of increased energy, which is observed as a blue-shift. Anti-stokes scatter is a result of molecules being above the ground state due to thermal energy. As the majority of molecules will be in the ground state, Stokes scattering is the most common

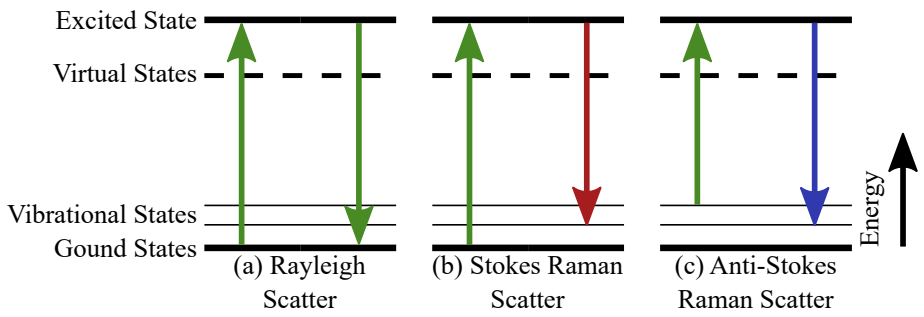

Figure 1.2: The energy levels of valence electrons excited by an incident photon for different scattering processes. (a) Elastic Rayleigh scattering. (b) Inelastic Stokes Raman scatter causing red-shift. (c) Inelastic anti-Stokes Raman scattering causing blue-shift.

form of Raman scatter [27]. Both Stokes and Anti-Stokes Raman scatter result in a wavelength shift, hence they are inelastic processes.

In Raman spectroscopy, the energy difference of incident and scattered photons is typically specified as a wavenumber ν with units of cm^{-1}

$$\Delta\nu\ (\mathrm{cm}^{-1}) = \left(\frac{1}{\lambda_0} - \frac{1}{\lambda_1}\right)\frac{10^7\,(\mathrm{nm})}{(\mathrm{cm})}, \tag{1.2.1}$$

where λ_0 is the incident wavelength and λ_1 is the scattered wavelength with both quantities measured in nm. Wavenumber is the unit conventionally used in Raman spectroscopy as it provides a convenient scale with most Raman scattering peaks occurring between zero to a few thousand cm^{-1}. Furthermore, the wavenumber scale is linear with energy, which is not the case for wavelength.

Raman scattering intensity is proportional to the change in molecular polarisation [28] and the locations of the Raman shift are dependent upon the molecular structure [26]. Hence, the Raman spectrum allows the chemistry of a sample to be determined.

Figure 1.3 shows the Raman spectrum for powdered single-walled carbon nanotubes on an aluminium slide, excited with a 785 nm laser. The vertical axis gives the number of counts from the spectrometer at the given Raman shift on the horizontal axis. Using this spectrum as an example for chemical investigation, the D-band ($1324\,\mathrm{cm}^{-1}$), G-band ($1575\,\mathrm{cm}^{-1}$) and 2D ($2613\,\mathrm{cm}^{-1}$) peaks identify the sample as a carbon nanotube. The position of these peaks, their relative intensities and additional peaks give information about defects and chemical processing [29]. Additionally, the radial breathing mode at $268\,\mathrm{cm}^{-1}$ allows the chirality and diameter of the nanotube to be determined [30, 31].

Figure 1.4 shows a schematic of a confocal Raman microscope. The input laser shown in green is focused through a narrow pinhole, passes through a beam splitter, and is focused by an objective lens onto the sample, which produces Raman scattered light. The Raman scattered light shown in red (or yellow when combined with the incident green light) is collected by the objective lens and reflected by the beam splitter. The incident green light is filtered out by the line filter and the filtered light is focused through a narrow pinhole. Scattered light that was produced out of the focal volume at the sample, shown in grey, will not be focused through the

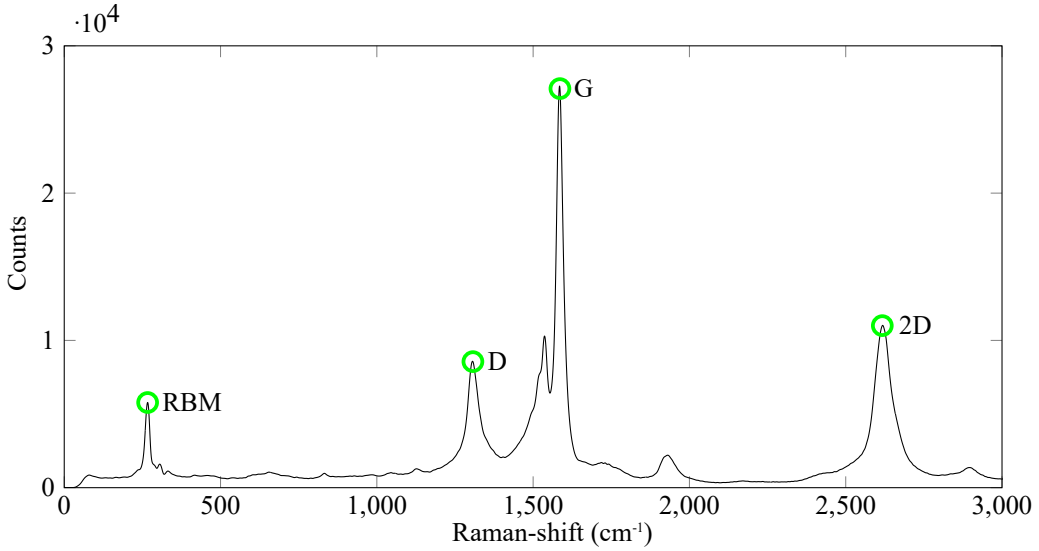

Figure 1.3: Raman spectrum of single-walled carbon nanotube excited with a 785 nm laser. The sample was prepared by scattering carbon nanotubes in powdered form on an aluminium microscope slide. The spectrum identifies the sample as a single-walled carbon nanotube and can be used to determine the diameter distribution and chirality of the nanotubes. The radial breathing mode, D-band, G-band and 2D bands are labelled.

pinhole. The remaining beam is collimated and passed to a spectrometer that separates the light based on its wavelength and outputs a Raman spectrum such as the one shown in Figure 1.3. The removal of out of focus light using the pinhole is an effective method for removing image blur, which results from the collection of out of focus light. Thus, the pinhole increases image resolution [32].

The probability of a scattering event is described by the scattering cross-section, which defines the area in which a photon must strike to initiate a scattering event. Raman scattering is a low probability event with a typical scattering cross-section of $10^{-29}\,\mathrm{cm}^2$ per molecule [33]. For comparison, typical cross-sections for infrared and ultra-violet absorption are approximately $10^{-21}\,\mathrm{cm}^2$ and $10^{-18}\,\mathrm{cm}^2$ per molecule respectively [28]. Hence, Raman spectroscopy is often limited by poor signal-to-noise. Several methods can increase the Raman cross-section. For instance, tuning the excitation wavelength to a molecules absorption band can increase the cross-section by over 2 orders of magnitude [34].

Raman signal intensity can also be greatly enhanced by utilising the near-field, which consists of an electromagnetic field that is strongly bound to a surface and decays according to the inverse cube law. The origins and properties of near-fields are described in more detail in Section 1.3. Surface-enhanced Raman spectroscopy (SERS) is a technique that excites the near-field by coupling into surface plasmons on a metal substrate. The localised electric field enhancement from the metal layer greatly enhances the Raman signal of the molecules on the surface. SERS has been reported to increase the Raman scattering cross-section by 7 orders of magnitude [35]. Similarly, surface plasmons can be excited on a sharp metal tip in tip-enhanced Raman Spectroscopy (TERS). TERS has been successfully combined with SERS to achieve a

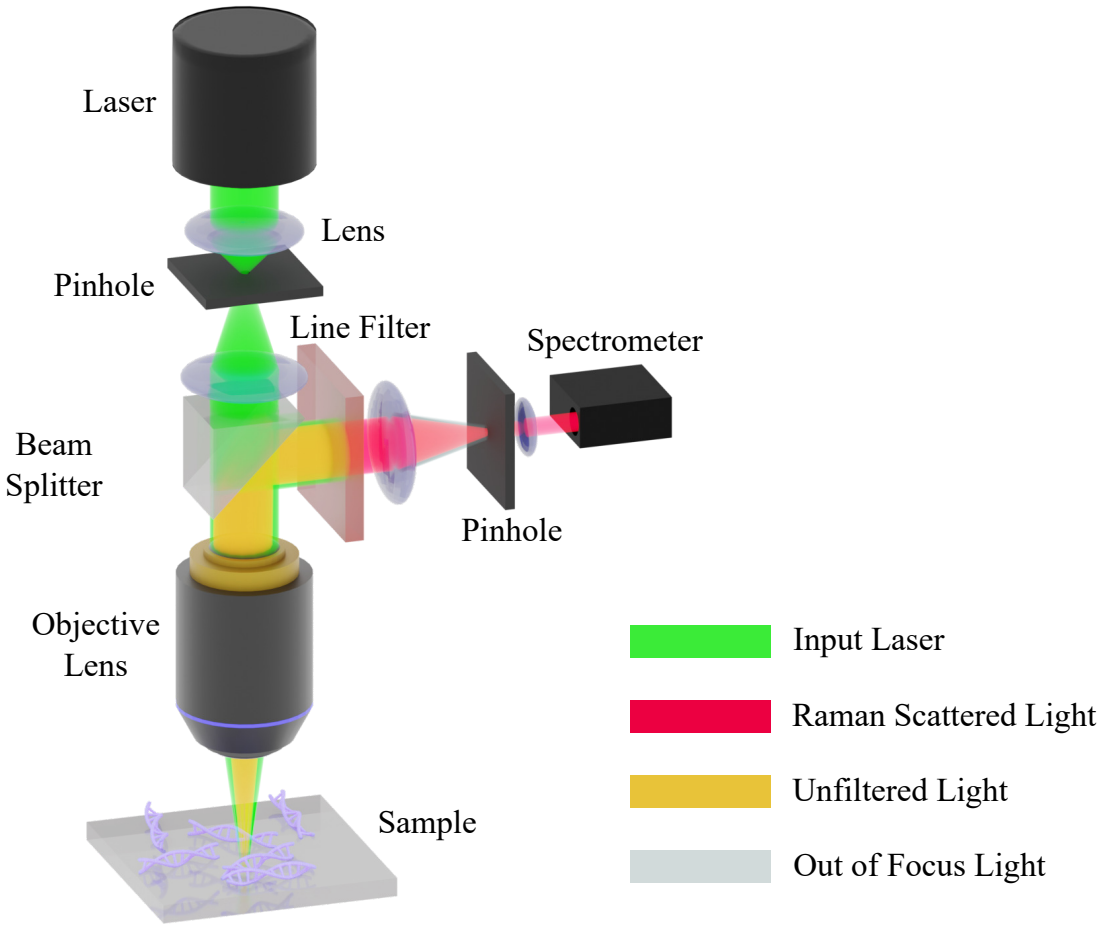

Figure 1.4: Schematic of confocal Raman microscope. Colours are a guide to differentiate between the input laser, scattered light and out of focus scattered light. The pinhole proceeding the spectrometer removes out of focus light, increasing image resolution compared to a non-confocal microscope.

further 3 orders of magnitude increase in Raman scattering cross-section [15]. These increases in scattering cross-section have a profound impact on the sensitivity of Raman spectroscopy with SERS [13] and TERS [36] able to achieve single-molecule detection.

Raman spectroscopy is widely used for non-destructive substance identification in pharmaceutical analysis, particularly for liquids, powders and gels as there is relatively little sample preparation required [2]. It is also used in food science to quantify pigment, dye, microorganism and packaging contamination levels in foods [7]. Furthermore, Raman spectroscopy has been used extensively in biomedical applications including measuring corneal hydration [37], identification of viral DNA fragments [3], detection of cancer [5], and has been used to determine the composition of kidney stones [4].

Abbe's diffraction limit gives the minimum resolvable distance for an optical system

$$d = \frac{\lambda}{2\mathrm{NA}}, \tag{1.2.2}$$

where λ is the wavelength of light and NA is the numerical aperture [38]. For modern optics operated in air, a good NA=1 is optimal and so

$$d \approx \lambda/2. \tag{1.2.3}$$

Figure 1.5 shows a Raman map produced by scanning a focused 638 nm laser over a sample of plastic nanoparticles. The image resolution is limited by the diffraction-limited spot size of the focused laser, which is approximately 300 nm. The resulting image is blurry and the boundaries of the nanoparticles cannot be clearly identified. This makes the technique ill-suited to imaging small nanoparticles and an alternative technique is required for higher resolution imaging. The spatial resolution can be greatly improved using near-field techniques, which are leveraged in tip-enhanced Raman spectroscopy. The origins, properties and application of near-fields are discussed in the following section. The application of near-fields to tip-enhanced Raman spectroscopy is described in Section 1.4.

1.3 Near-field Enhancement

One method for overcoming the diffraction limit is to use an optical near-field. This section details two methods for producing a near-field. The first method couples light through a sub-wavelength aperture. The second method excites surface plasmons on a metallic tip. The origins of surface plasmons are also discussed. Derivations are provided in Appendix B, which are adapted from [39, 40].

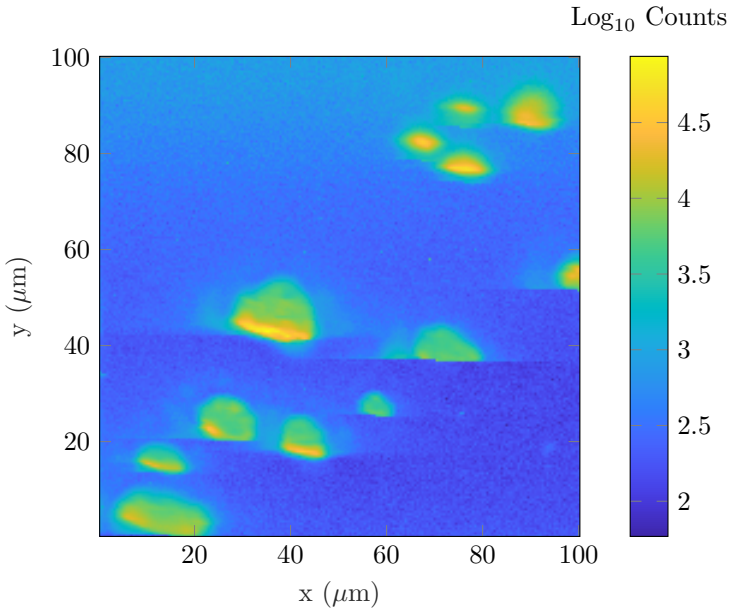

Figure 1.5: Raman map of polystyrene nanoplastic particles on a glass microscope slide imaged using a 638 nm laser. The spectrum is integrated over 1332 - 1368 cm^{-1} and the colour represents the total number of counts from the spectrometer. Each pixel is 0.5 × 0.5 μm. The resolution of this image is poor with the particles showing blurred edges and little information about the structure can be determined. Line artefacts are present in this image and consist of discrete horizontal scars. These artefacts are due to optical drift.

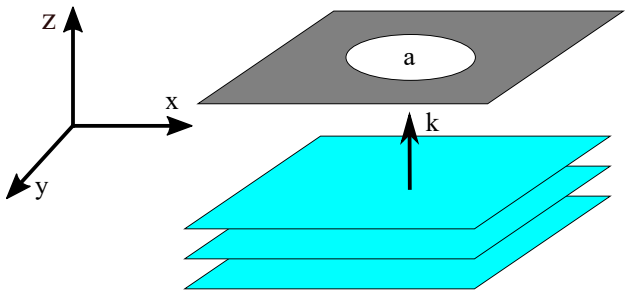

Figure 1.6: Illustration of light being coupled through a sub-wavelength aperture of diameter a and angular wavenumber k. An evanescent electric field is created at the aperture and is known as the near-field. Beyond two wavelengths the near-field contribution is negligible and the far-field dominates. This phenomenon can be utilised for near-field applications such as TERS. The narrow aperture can be achieved with a metal-coated tapered optical fibre.

1.3.1 Sub-wavelength Aperture

Consider a two-dimensional, perfect conductor in the x-y plane with a small circular aperture of diameter a and a plane wave travelling in the z-direction as shown in Figure 1.6. There are two possibilities for the resulting angular wavenumber $k = \frac{2\pi}{\lambda}$ through the aperture as derived in Appendix B.2. They are as follows:

1. $k_z > 0$, which forms a radiative wave that will propagate.
2. $k_z < 0$, which will decay exponentially from the aperture. This is often referred to as the evanescent wave or near-field.

At large distances from an aperture, the radiative wave will dominate. This typically occurs beyond two wavelengths and is known as the far-field. Within one wavelength, the evanescent wave contributes significantly, and this region is known as the near-field [41]. The relationship between the electric and magnetic fields is more complex in the near field, simplifying in the far-field where they become orthogonal to one another and the direction of propagation [42].

The near field contains an increased power density, which decays exponentially away from an aperture. This can be used in near-field applications to circumvent the diffraction limit. Near-fields are used in imaging techniques such as TERS, where the localised field from a metallic tip improves the Raman signal by several orders of magnitude [15].

1.3.2 Surface Plasmons

The collective oscillations of conduction electrons are responsible for the absorption and scattering of light from metals, giving them their colours [43]. These collective oscillations are known as surface plasmon resonances and are responsible for the near field enhancement from metallic probes. The oscillations can be excited by an electron beam or electromagnetic radiation. Only electromagnetic radiation excitation is considered in this thesis as tip-Enhanced Raman spectroscopy is performed using a focused laser beam. The theoretical background for the formation of surface plasmons is given in Appendix B.3 and a summary of the results are discussed here.

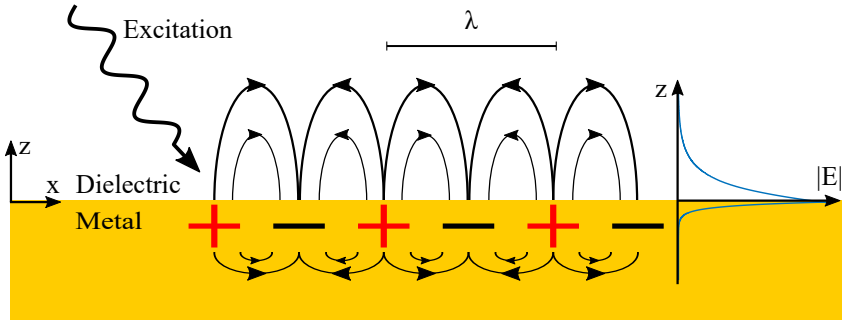

Figure 1.7: Illustration of a surface plasmon resonance at the metal-dielectric interface of a bulk metal. Positive and negative surface charges are represented as + and - respectively. Electric field lines are represented by →. The collective surface charge oscillations are excited by the incident electric field. The graph shows the electric field strength $|E|$ as a function of z-position. The field strength drops exponentially in the metal layer, typically decaying to $1/e$ intensity after tens of nm, i.e. the skin depth. The field also decays rapidly in the dielectric layer as the electric field is strongly bound to the metal-dielectric interface.

Surface plasmons are electromagnetic waves that propagate along the interface between a metal and dielectric interface when the metal has a negative real permittivity [44]. A negative real permittivity is a common property of metals in the visible and near-infrared. Meanwhile, the losses of a plasmon are proportional to the imaginary permittivity. Figure 1.7 shows the formation of a surface plasmon at the interface between a bulk metal and a dielectric. The excitation electric field oscillates the conduction electrons on the surface forming a surface plasmon. The electric fields decay exponentially in the z-axis. In the metal layer, electric field propagation is forbidden due to the negative real permittivity. The penetration of the electric field can be characterised by the skin depth δ which gives the depth at which the radiation intensity falls to $1/e$ of its original value or 37%. Hence, the electric field is strongly confined to the metal-dielectric interface.

When the size of a particle approaches or is smaller than the wavelength of the excitation light, surface plasmons will be confined to the particle. Hence, there will be no propagating modes, only standing waves known as a localised surface plasmon resonance (LSPR). Figure 1.8 shows the formation of a localised surface plasmon resonance on a gold nanosphere. The electric field from the incident electric field causes oscillations of the conduction electrons on the particle surface. The coulomb attraction between the negative electrons and positive ions provides the restoring force. At resonance, these charge oscillations result in an enhancement of the electric field in proximity to the surface and increase the particles optical absorption.

The material properties and geometry of the nanoparticle control the plasmon response including the number of supported modes, excitation frequencies and near-field enhancement strength. Analytic solutions exist for spheroids, infinite cylinders and shells with sizes well below the excitation wavelength [18]. However, the analytic solutions become inaccurate when the particle size increases as de-phasing of the excitation occurs at the particle surface. Furthermore, analytic solutions do not exist for arbitrary shapes. Thus, numerical methods are needed to model plasmon responses of nanoparticles. Chapter 2 details the modelling of surface plasmons

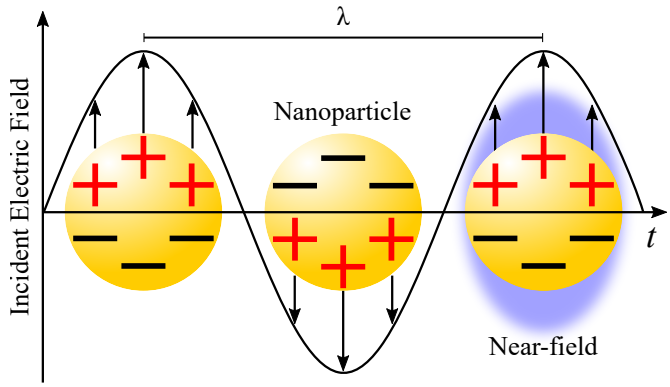

Figure 1.8: Illustration of a localised surface plasmon resonance on a gold nanoparticle. Positive and negative surface charges are represented as + and - respectively. The collective surface charge oscillations are excited by the incident electric field such as an electron of electromagnetic wave. At the particles resonance wavelength, the charge oscillations produce a near-field that is bound to the surface.

on metallic nanoparticles using the boundary element method.

1.4 Tip-Enhanced Raman Spectroscopy

Tip-enhanced Raman spectroscopy (TERS) is an imaging technique that overcomes the diffraction-limited resolution and low signal-to-noise of Raman spectroscopy [45]. TERS is performed by probing a sample with an optical near-field. This differs from Raman spectroscopy where a focused laser beam is used. Similar to far-field Raman spectroscopy, the wavelength shift between the illumination source and scattered light provides chemical information about the sample. TERS has been demonstrated with resolutions significantly below the diffraction limit [45, 46]. Furthermore, the near-field results in increased Raman signal to the point that single-molecule detection is possible [13]

One method for producing the near-field required for TERS is to couple light through a narrow aperture as described previously. Typical examples of aperture probes are tapered optical fibres coated with a reflective metal [47], or, an AFM probe with a narrow aperture drilled through the tip [48]. Light is focused into the structure and the resulting near-field is used to probe the surface [49]. The optical resolution is proportional to the aperture radius and the power throughput scales with the sixth power of aperture radius [50]. This severely limits the power throughput when high resolutions are required [51]. Figure 1.9(a) shows the electric field distribution through an aperture probe. The simulation reveals that the spatial dimensions of the near-field are approximately equal to the aperture diameter. Furthermore, there is a decreased enhancement through the aperture indicating a loss of optical power.

A second method produces the required near-field by exciting an LSPR on the surface of a scanning metallic tip as described previously. This is known as an apertureless probe and has been adopted in the literature and industry due to the increased power throughput compared to aperture TERS [52]. Apertureless probe power is limited by the temperature at which the

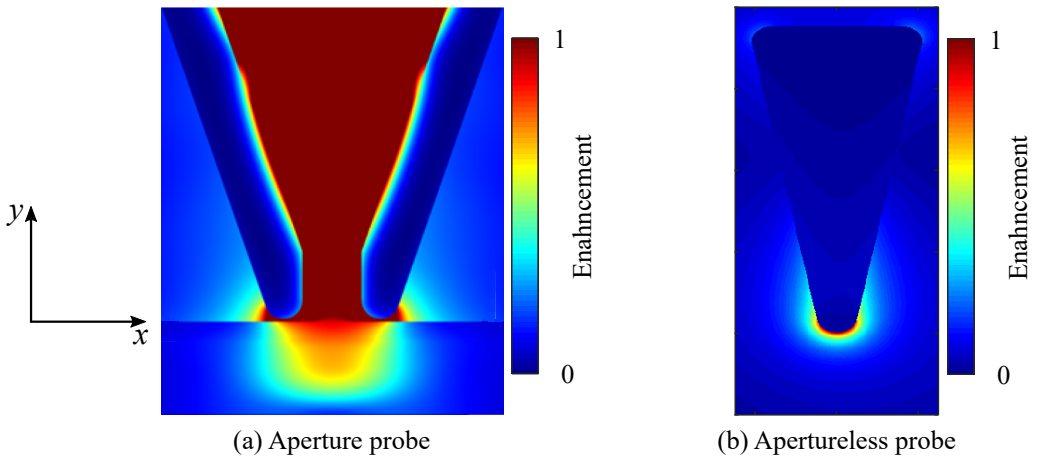

Figure 1.9: Simulations showing the electric field enhancement for (a) aperture [51] and (b) apertureless TERS probes. For (a), a plane wave is coupled through the top of the structure and exits through the aperture onto a substrate. For (b), a plane wave propagating in the x-axis with polarisation in the y-axis excites a surface plasmon, which results in significant enhancement at the tip apex. The colour shows the enhancement of the electric field.

probe will be destroyed. The apertureless probe must be designed such that an LSPR is formed at the excitation wavelength [22]. The LSPR excitation wavelength and near-field intensity are dependent upon tip geometry, material properties and surface morphology [18]. Hence, the tip design is paramount to TERS performance. Figure 1.9(b) shows the electric field distribution for an apertureless probe excited at its resonance frequency. The maximum enhancement occurs at the tip apex, which can be used to effectively probe a surface during TERS. The spatial dimensions of the near-field give the optical resolution and are proportional to the tip apex diameter [19]. Due to the major disadvantages associated with aperture probes, these will not be discussed further.

The operation principles of TERS with an apertureless probe are illustrated in Figure 1.10. A focused laser beam excites an LSPR on a metallic nanoparticle located at the end of an AFM tip. The resulting near-field enhances Raman scatter of the sample within a small volume located at the tip apex. Due to the near-field confinement at the tip apex, the tip must be kept close to the sample. Typically, the tip will be in contact with the sample or within a few nm. The scanning tunnelling microscope and atomic force microscope offer nanometre resolution z-axis control, which is ideal for TERS. In this thesis, an atomic force microscope is used to control the position of a TERS tip as it is scanned over a sample. A more technical description of AFM is given in Chapter 4.1, while a detailed comparison of TERS operation modes is given in Chapter 7.

Figure 1.11 shows a TERS map of multi-walled carbon nanotube bundles on a gold substrate, acquired using a silver-coated AFM probe illuminated with a 638 nm laser. Bundles of nanotubes are visible with a diameter of 25 nm, well below the diffraction-limited spot of the 638 nm laser. Comparing the TERS map to the far-field Raman map shown in Figure 1.5 it is clear that TERS

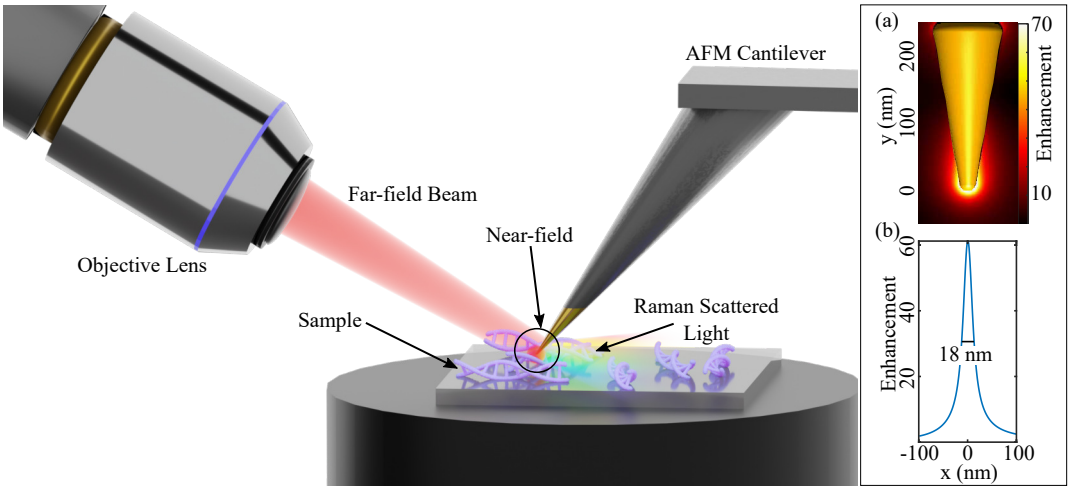

Figure 1.10: The operating principle of TERS, where a laser is focused onto a metallic tip, exciting an LSPR. This produces a near-field that is kept close to the sample using an AFM system resulting in increased Raman scattering in the near-field volume. (a) Simulated electric field enhancement for a gold nanocone. The enhancement at the tip apex amplifies Raman scattering in a small volume. (b) Electric field enhancement 1 nm below a gold nanocone with the spot diameter (full width half maximum) showing the spatial confinement of the field (black line). The small spot diameter enables sub-diffraction-limited resolution.

offers superior resolution and is well suited for imaging nanometre-scale structures. There are many examples of TERS images displaying sub-diffraction-limited resolution [8,16,25,53], where the optical resolution is reported to be similar to the tip apex diameter [15].

1.4.1 Origins of Enhancement

Figure 1.12 shows the Raman signal from a sample of C_{60} with a TERS probe in contact with the sample, and when retracted. The Raman peaks labelled with squares show significant amplification when the tip is in contact with the sample. There are several mechanisms that contribute to the overall enhancement of the TERS signal. This section describes the signal enhancement observed for TERS in terms of the non-resonant and localised surface plasmon resonance effects.

Non-Resonant Enhancement

Non-resonant enhancement, also known as the lightning-rod effect, is a result of electric field line concentration near highly curved surfaces and results in enhancement of the electric field [54]. Non-resonant enhancement does not require a negative real permittivity or a small imaginary permittivity. It is dependent on the geometry with the maximum amplification limited by the modulus of the real dielectric function. Consider a silicon AFM cantilever with a smooth gold coating. Assuming the tip is multiple microns long, the LSPRs will be dampened significantly due to a high imaginary permittivity at the resonance wavelength. Hence, the enhancement will be primarily due to non-resonant enhancement.

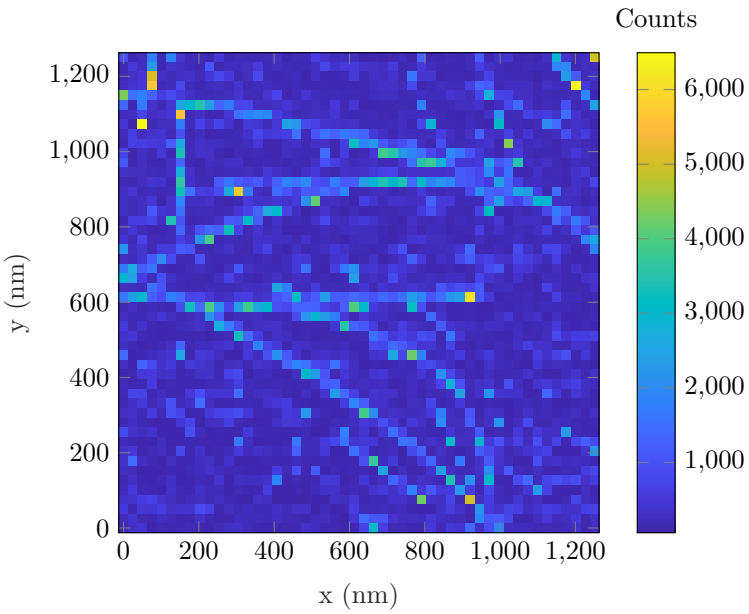

Figure 1.11: TERS map of carbon nanotube bundles on a gold substrate imaged using a 638 nm laser, integrated over 2657 - 2696 cm^{-1}. Each pixel is 25 × 25 nm. This image displays sub-diffraction-limited resolution as neighbouring bundles can be differentiated to distances below the approximately 319 nm diffraction-limited laser spot.

Rough metal surfaces are observed to increase Raman enhancement. One aspect of this can be explained by non-resonant enhancement. The surface roughness features are much smaller than the excitation wavelength, hence the electric field enhancement due to the lightning rod effect will be greatest near the sharp surface features [55, 56]. Molecules on these sharp features will exhibit greatly enhanced Raman signals. For example, the enhancement and spatial resolution are improved at the edges of gold nanodisks [57]. However, non-resonant enhancement is small in comparison to enhancement due to resonant plasmon effects [58, 59].

Localised Surface Plasmon Enhancement

The excitation of localised surface plasmons on metal nanostructures can occur on both the scanning metallic tip and a metal substrate (SERS). When localised surface plasmons are excited efficiently, the resonant enhancement becomes far more significant than non-resonant enhancement [60]. The work presented in this thesis focuses on resonant enhancement as it dominates non-resonant enhancement under optimal conditions for TERS [61].

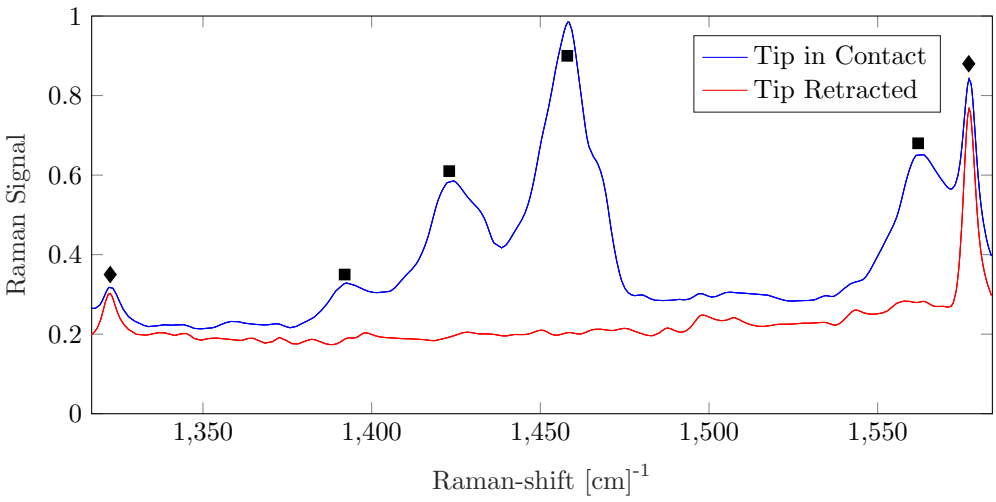

Figure 1.12: Raman spectra of C_{60} measured with a tuning fork set-up. The blue trace is collected with a gold tip in contact with the sample. The red trace is collected with the tip retracted. The square identify the Raman peaks showing significant amplification with the tip in contact. The diamonds indicate the bands of the lens immersion oil. Data was adapted from [15].

Tip-Sample Effects

Tip-sample interactions also affect enhancement and spatial resolution. Further spatial confinement and increased enhancement are achieved with plasmon-excition coupling [62, 63] and the formation of tip-sample-tip gap modes [64–66], while at small tip-sample separations quantum effects begin to reduce confinement [67]. In addition, the sample chemistry influences the scattering efficiency. For example, predominantly covalent nanoparticles have been shown to have significantly higher scattering cross-sections compared to ionic nanoparticles due to an increased polarisability, resulting in a two order of magnitude increase in the enhancement factor [68]. Highly anisotropic molecules such as nanotubes are sensitive to polarisation [69]. Finally, Raman enhancement is dependent on conduction electron properties [70, 71].

1.5 Commercial TERS Probes

Commercially available TERS probes consist of a silicon AFM probe with a metal coating applied that forms a rough grain-like structure. The metal coating is typically silver as it has been shown to offer good electric field enhancement over the visible wavelengths [72].

A scanning electron microscope (SEM) image of a commercially available TERS probe tip is shown in Figure 1.13(a). The tip is silicon with a thin layer of silver. The surface appears relatively smooth with minor bumps due to the low silver content of the tip, measured at 22% mass content using energy dispersive x-ray spectroscopy (EDX). This tip had poor conductivity in the SEM due to the low metal content. The poor conductivity resulted in surface charging,

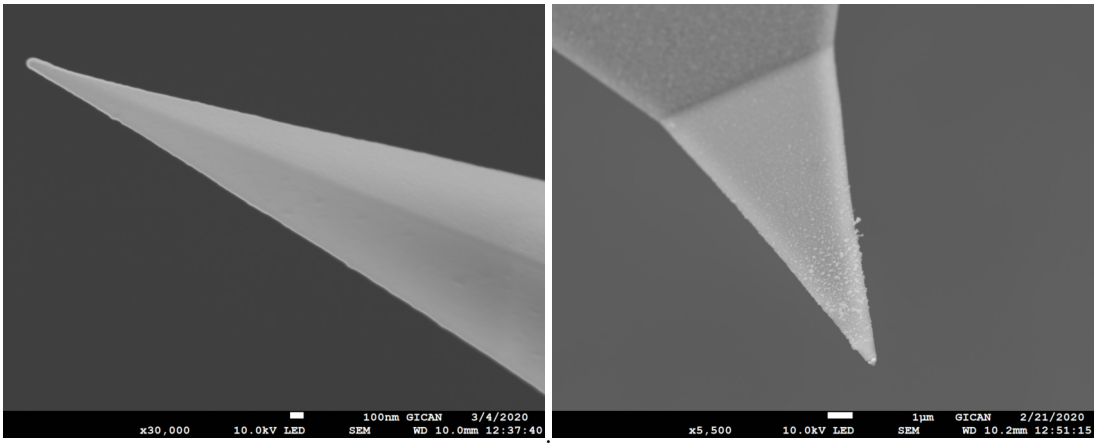

Figure 1.13: SEM images of commercially available TERS probes. (a) Silver coated Nauga-Needles NN-TERS-T probe, which appears relatively smooth and has an average silver mass percentage of 22% determined using EDX. Of the 4 examples of this tip that were tested, none produced a measurable Raman enhancement at 638 nm or 785 nm illumination wavelengths. (b) Silver coated Omni-TERS probe with an average silver mass of 33% as confirmed using EDX and the surface appears grainy. This tip was used to produce the TERS map shown in Figure 1.11

which limited the achievable image resolution. Hence, the surface may be more grainy than it appears in the image shown. Importantly, after testing 4 of these tips, none were able to produce a measurable Raman enhancement with a laser wavelength of 638 nm or 785 nm. This is an example of a commercially available TERS probe with too little metal content to function adequately. Furthermore, no optimal operation wavelength was given for this probe and was not provided upon request.

An SEM image of a second commercially available TERS tip is shown in Figure 1.13(b). This tip also consists of a silicon AFM tip with a thin layer of silver. The surface of this tip is noticeably more granular than the previous example, with islands of silver forming. The silver mass content was measured to be 33% using EDX. These tips have been used to successfully enhance Raman signals and acquire Raman maps such as the one shown in Figure 1.11. The disadvantages of these tips are the inconsistent performance from tip to tip, poor lifetimes, an offset between AFM topography and Raman maps, and sub-optimal TERS resolution due to the relatively large apex diameter. These issues are discussed in more detail in the following subheadings.

Random Nanoparticle Formation

Metal layers produced using vacuum deposition or electrodeposition [73] tend to form grainy surface layers. For plasmon applications, these surfaces yield high electric field enhancement. However, the formation of metal grains and nanoparticles cannot be directly controlled [22]. For example, it cannot be guaranteed that a nanoparticle of a certain size will be formed at the mechanical tip apex. This leads to several issues.

Figure 1.14(a) illustrates a grainy TERS tip, where a nanoparticle is not present at the tip apex. This will separate the mechanical tip apex and the near-field. The separation of the two results in an offset between the TERS and AFM maps. Furthermore, the presence of more than one nanoparticle at the apex will distort the electric field distribution [74] and create imaging artefacts [75].

The random formation of nanoparticles is one cause of the unreliability of TERS probes. With a thin metal layer, there is a high chance that a metal nanoparticle will not form at the tip apex. If there are no nanoparticles in the vicinity of the tip apex then no Raman enhancement will be observed. It is believed that the tip shown in Figure 1.13(a) did not produce a Raman enhancement because the silver layer was not thick enough to ensure a nanoparticle at the tip apex. This is supported by the low silver mass content of 22%. On the other hand, a thick metal layer will increase the likelihood that a nanoparticle will form at the tip apex. However, a thicker metal layer increases the tip diameter, which will reduce the TERS and AFM resolution. This is illustrated in Figure 1.14(a) where the physical size of the tip apex results in a lower resolution AFM image. The tip shown in Figure 1.13(b) is 33% silver by atom mass and produces a significant near field enhancement, which is thought to be due to the thicker metal layer and the presence of discrete nanoparticle formations at the apex.

Commercially available TERS probes with sufficiently grainy structures can be viewed as a collection of individual nanoparticles. The resonance wavelength and electric field enhancement of TERS probes with multiple nanoparticles are both highly dependent on the number, position and size of the nanoparticles [76]. Since the formation of these nanoparticles is random, there may be significant performance differences between identically fabricated probes.

In summary, the random formation of nanoparticles on metal coated probes can result in:

- An offset between AFM and TERS maps.
- Artefacts in the TERS map.
- Unreliable Raman enhancement from probe to probe with some tips producing no measurable enhancement.
- Decreased AFM and TERS resolutions.

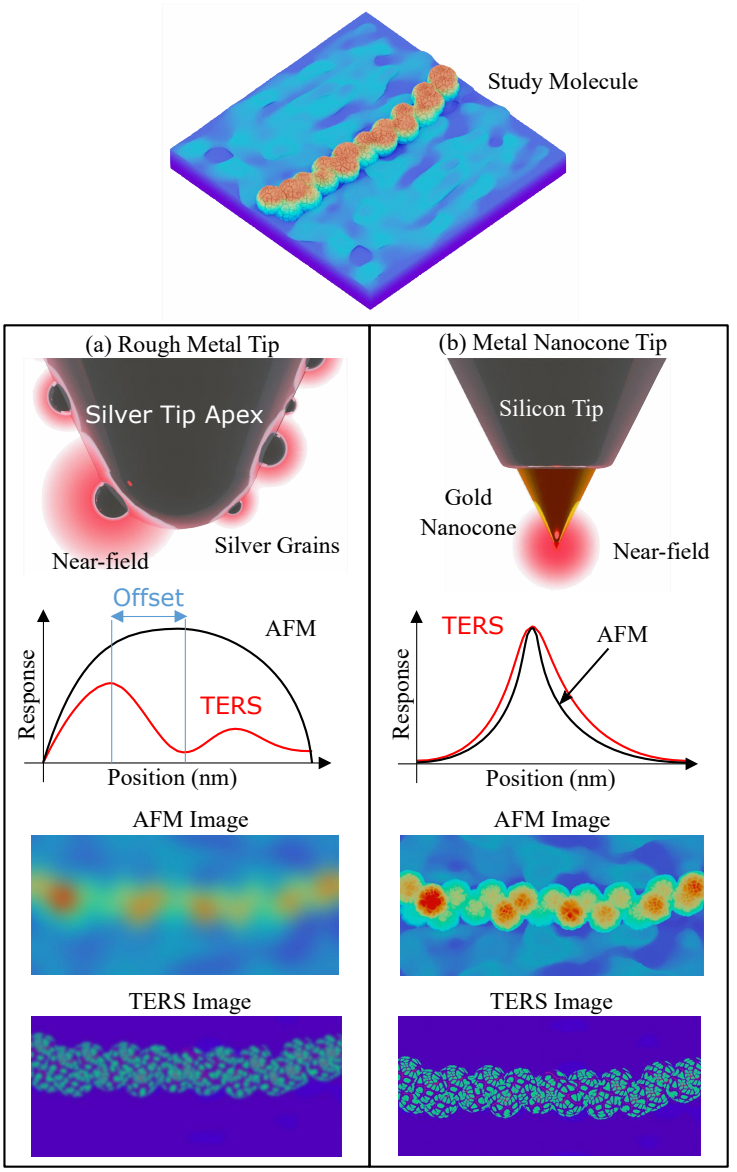

Figure 1.14: Illustrations that describe how the random nature of grain formation can result in an offset between AFM and TERS maps. Both tips are scanned across the molecule of study. (a) Shows a tip apex with a grain structure where a nanoparticle has not formed at the AFM tip apex. This creates an offset between the location of maximum electric field enhancement and the physical AFM tip apex. This manifests as an offset between the AFM and TERS maps. In addition, the separation between the maximum electric field enhancement and the sample is increased, which results in a decreased TERS signal. Finally, the metal coating thickness has increased the physical size of the AFM tip apex resulting in decreased AFM resolution. (b) Shows a nanocone tip with a single and aligned optical and mechanical apex, which eliminates the offset between the AFM and Raman images. The nanocone geometry results in zero offset between the AFM and Raman responses. The nanocone geometry also results in higher resolution in the AFM and TERS images.

Lifetime

Silver nanoparticles tarnish rapidly in laboratory conditions, exhibiting a decreased absorption coefficient by one order of magnitude over 36 hours and a near-field resonance wavelength redshift of 1.8 nm/hr [20]. This is due to the introduction of contaminants forming oxides and sulphides, which have the potential to change the surface morphology [77, 78]. As a result, silver-based TERS probes have lifetimes limited to approximately one day. This is prohibitive given the significant set-up time associated with aligning the optical system, which must be performed for each new probes. In the experience of the author, probe lifetime has a random element with some probes of a given design having lifetimes extending beyond one week while others last only one day.

The lifetime of silver probes can be extended by adding a passivation layer on the silver layer. However, this increases the separation between the surface plasmon and the sample resulting in a decreased near-field enhancement and a decreased AFM resolution. Alternatively, the probes can be stored at vacuum or in an inert gas such as nitrogen.

Optimised Performance

At the time of writing, commercial TERS probes are sold without a specified illumination wavelength. However, the literature has identified that probes should be excited at the resonance wavelength to achieve maximum Raman enhancement [61, 76, 79, 80]. Hence, when using a commercially available TERS probe it is unlikely that the excitation wavelength and enhancement are optimal. A more robust method for probe design would involve tuning the resonance wavelength to the illumination wavelength.

The Search for an Improved TERS Probe

Due to the issues associated with commercially available TERS probes, there is great interest in finding an improved solution. An ideal TERS probe would offer:

- Zero offset between the AFM and TERS maps. This could be achieved by ensuring the near-field enhancing nanoparticle also serves as the physical apex of the tip.
- Improved chemical stability allowing a TERS probe to high enhancement for several weeks. This can be achieved using gold rather than silver, or by applying a passivation layer.
- Improved probe-to-probe consistency, which could be achieved by using fabrication methods that do not rely on the random formation of nanoparticles.
- Higher Raman signal-to-noise ratios, which could be achieved by matching the resonance wavelength of the probe and the illumination wavelength.

The focus of this thesis is to design and fabricate improved TERS probes that are based on a solid metal nanocone geometry that has optimised dimensions as illustrated in Figure 1.14(b). The nanocone approach reduces the offset between AFM and TERS images by ensuring the mechanical tip apex and the near-field are collocated. As there is no requirement for random

formation, nanocone probes are expected to be significantly more consistent than metal coated probes. The nanocone fabrication process will also enable geometry optimisation to maximise enhancement in a given application. Finally, a nanocone can be sharpened to a smaller apex diameter than an AFM tip with a thick metal layer, which will enable higher resolution AFM and TERS images. If constructed from gold, these tips would also offer superior lifetimes to those currently available.

1.6 Measuring Probe Performance

To accurately compare the performance of new probes with currently available TERS probes, a new experimental method is required. Two important performance metrics for TERS are electric field enhancement at a given wavelength and the achievable resolution which is proportional to the spot size of the near-field. Both of these metrics are shown in 1.10(b).

Methods are outlined in the literature for measuring the Raman enhancement of TERS probes. However, these rely on estimates for the spot size of the enhanced electric field and assume a homogeneous enhancement within this volume [15, 23, 36, 81]. These measurements are sensitive to the proportion of the enhanced spot interacting with Raman active molecules. For example, if only half of the near-field volume is filled with Raman scattering molecules, the enhancement will be underestimated. Furthermore, the spot size is assumed to be the diameter of the tip apex. While the spot size of the near-field is proportional to the apex diameter, the field will exist beyond this scale, albeit decaying rapidly. Hence, neighbouring molecules will contribute to the Raman enhancement which is not accounted for.

Improved measurement methods would remove the estimation of the enhanced electric field spot size and measure this directly. Furthermore, a reconstruction of the electric field distribution below the tip apex would allow the peak electric field enhancement value and the theoretical resolution to be determined. These measurements will allow accurate comparisons between TERS probes and aid in the optimisation of TERS tips. Measurement methods that satisfy these requirements will be developed in this thesis.

1.7 Thesis Outline

This thesis focuses on the design, fabrication and performance analysis of an improved TERS probe. Furthermore, a method is developed for accurately measuring the performance of TERS probes.

In Chapter 2, boundary element simulations are used to explore the formation of surface plasmons on metallic nanoparticles. The results are used to compare different nanoparticles and determine an appropriate starting geometry for a nanoparticle to use as a TERS probe. Additional variables such as focused laser beam position and beam width are discussed. The gold nanocone is chosen as a suitable nanoparticle as the resonance wavelength can be tuned independently of the spot size.

In Chapter 3, the geometries of gold and silver nanocones are optimised using boundary

element method simulations. Regression analysis is performed to produce models that allow the resonance wavelength and electric field enhancement of gold and silver nanocones to be estimated. These models are used to design TERS probes for improved Raman enhancement.

Chapter 4 details experimental techniques used in this thesis. This includes descriptions of AFM, electron beam microscopy, x-ray dispersive spectroscopy and focused ion beam techniques.

In Chapter 5, a method is developed for reliably and accurately measuring TERS probe performance. This method is based on exciting the radial breathing mode of single-walled carbon nanotubes, allowing isolated tubes to be distinguished from bundles. Isolated nanotubes act as one-dimensional scattering surfaces and are used to measure the PSF of TERS probes. The developed method is used to measure and compare the performance of commercially available grainy metal TERS probes.

Chapter 6 details the fabrication of gold nanocone TERS probes based on the optimisations from Chapter 3. The performance of the gold nanocone TERS probes is measured and compared to the commercially available, grainy metal probes. The gold nanocone probes are shown to provide a narrower PSF, comparable optical contrast and collocated TERS and AFM maps. Thus, the gold nanocone probes are superior probe high-resolution TERS imaging.

Chapter 7 presents an alternative mode of TERS operation known as modulated-illumination intermittent-contact TERS (MIIC-TERS). The performance of this imaging technique is compared using a grainy metal probe and the gold nanocone probe developed in this thesis. The gold nanocone probe is found to provide superior imaging performance with MIIC-TERS.

The thesis concludes in Chapter 8, where a brief summary of contributions is presented and potential future work is outlined.

Chapter 2

Modelling the Near-Field

In this chapter, the boundary element method is investigated for simulating the near-field response of nanoparticles. This method is found to be suitable for simulating the TERS performance of nanoparticle geometries. Multiple elementary shapes are modelled and their performance as potential TERS probes is assessed. These results are used to recommend nanocones as a suitable geometry. Furthermore, the effects of illumination beam polarisation, beam width and focus position are investigated.

2.1 Modelling Approaches

2.1.1 Finite Element Method

Finite element methods have been used successfully in the literature to study the optical properties of nanoparticles [81–86]. A dense set of discretisation points is required to capture the exponential decay of surface plasmons on a metal surface because noble metals have short skin depths, i.e. where the current density falls to $\frac{1}{e}$. For example, gold has a skin depth of approximately 25 nm at a wavelength 785 nm [87]. To capture the rapid decay of the electromagnetic fields near the surface, multiple grid points in this thin layer are required [88]. Furthermore, two-dimensional simulations cannot be used to predict the response of nanoparticles as confinement in three dimensions is needed [18]. Hence, grids with a large number of points are required. This makes finite element methods time and memory intensive.

The time and memory requirements of finite element method techniques may be acceptable when investigating the plasmon response of a single nanoparticle. However, in this thesis, many structures are simulated across different operating conditions. This is not feasible with finite element methods and a more efficient alternative is required.

2.1.2 Boundary Element Method

The Boundary element method (BEM) only requires discretisation of the boundaries between materials of different dielectric functions [89]. This is a significant advantage over finite element methods that require the problem space volume to be filled with discretisation points. The BEM carries the disadvantage of being unable to account for non-homogeneous and anisotropic dielectric functions. For simulating the plasmon response of homogeneous and isotropic nanoparticles, the reduction in memory requirements and computation time make BEM an attractive option for the optical simulation of arbitrary shapes [90]. BEM is consistent with analytical results using Mie theory for spheres and ellipsoids [91].

BEM simulations can be simplified using the quasi-static approximation. This assumes that the particle excitation is in phase across the surface, which is acceptable for small particles [92] and greatly reduces computation complexity. In the work presented in this thesis, the particle size often approaches the excitation wavelength and so retarded calculations are needed, which are based on Maxwell's equations [93]. An exception is made when simulating Gaussian beam excitation. A summarised derivation of the equations used for BEM Maxwell calculations is given in Appendix A. In this thesis, BEM simulations are used to calculate the near field enhancement for metallic nanoparticles.

2.2 Methodology

In the following sections, the boundary element method package Metallic Nanoparticles using BEM (MNPBEM) [91, 92], was used to solve Maxwell's equations in the frequency domain for gold and silver nanoparticles in a vacuum. The problem space is described in Figure 2.1(a). The particle boundaries consist of boundary elements that are defined by a set of vertex positions and normal vectors. Convergence testing was performed by increasing the number of boundary elements and examining the near field distributions. Measured dielectric functions for gold and silver are taken from the literature [94]. These dielectric functions are shown in Figure 2.3. Unless stated otherwise, a plane wave excitation E_{exc} was considered to be propagating in the x-axis direction with polarisation in the y-axis, that is

$$\mathbf{E}_{\text{exc}} = E_0 e^{-ik\omega} \hat{\boldsymbol{y}}, \tag{2.2.1}$$

with incident electric field magnitude E_0, wavenumber k and angular frequency ω. E_0 is normalised to 1.

The electric field is calculated over an M x N grid 1 nm below the particles lowest z point. The electric field is always calculated on this grid for two reasons. Firstly, the grid simulates the configuration between a TERS probe and a sample in the side-illumination configuration. Secondly, the near-field response of a particle is dependent upon the point of measurement [39]. By moving the measurement point, the measured localised surface plasmon resonance wavelength will change. For TERS it is important that the highest electric field enhancement occurs at the sample. Hence, the location of the sample is used as the measurement area.

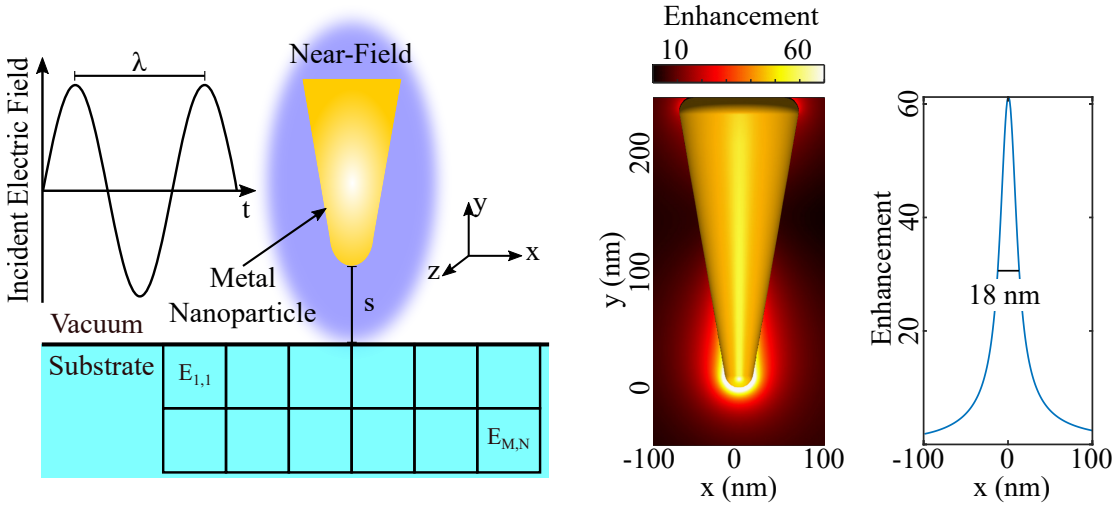

(a) Simulation space (b) Enhancement Map (c) Cross-Section

Figure 2.1: Example problem space and calculations. (a) x-y Cross-section of the simulation space, consisting of a vacuum with an embedded nanoparticle defined by an outer boundary. The tip is positioned with the bottom vertex at the origin, a distance s above an M x N grid where the electric field magnitude $E_{M,N}$ is calculated. (b) Near-field enhancement distribution for a gold nanocone. (c) Enhancement in the x-direction 1 nm below the nanoparticle apex. The near-field enhancement is given by the peak enhancement value. The spot size is given by the full width at half maximum (FWHM) of the peak.

For simplicity, the effects of a substrate are not considered in this chapter. However, proximity to a substrate introduces several effects that influence the near-field resonance of nanoparticles. For example, an increased substrate refractive index has been shown to redshift the resonance wavelength [61]. These effects are discussed in Chapter 3.

Two metrics are used to compare the near-field performance of nanoparticles in the following sections:

1. The near-field enhancement at the localised surface plasmon resonance of the particle. This is given by $E_{\max}/E_0$, where $E_{\max}$ is the maximum electric field magnitude calculated at a specified distance from the nanoparticle apex and E_0 is the normalised excitation electric field magnitude. The near-field enhancement will be proportional to the total Raman signal achievable for TERS.

2. The spot size is the full width at half maximum (FWHM) of the electric field on the top row of the measurement grid as shown in Figure 2.1. This predicts the spatial resolution achievable for TERS.

As an example, Figure 2.1(c) shows the near-field enhancement distribution in the $\hat{x}$ direction 1 nm below a nanoparticle. The near-field enhancement for this nanoparticle is given by the peak value of the enhancement. The spot size is given by the width of the enhancement peak at half of its maximum value. For the example given, the enhancement is 62 and the beam width is 18 nm.

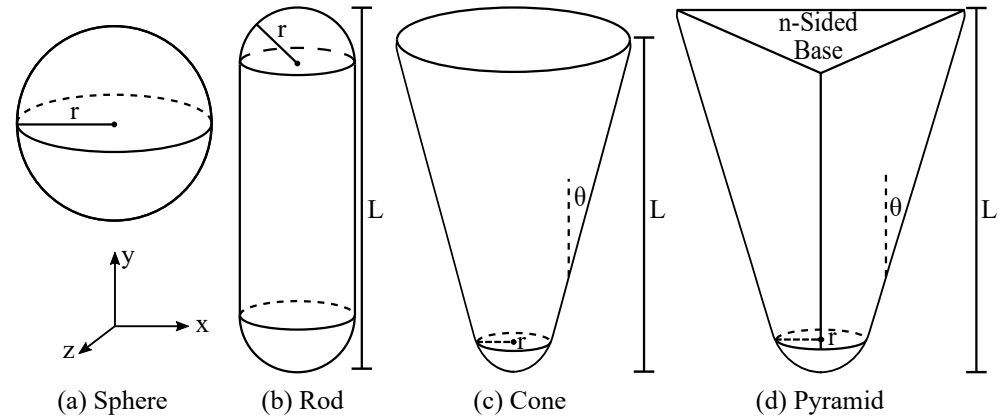

Figure 2.2: Geometries of the nanoparticles simulated in this chapter with the dimensions of apex radius r, length L and angle θ.

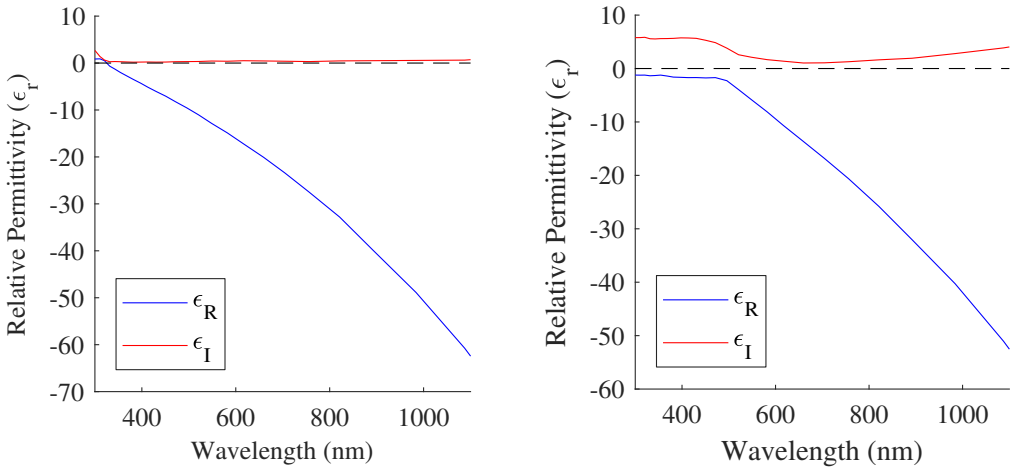

(a) Silver.

(b) Gold.

Figure 2.3: Relative permittivity of silver and gold. The lower ϵ_I for silver across optical wavelengths reduces plasmon dampening. Data adapted from [94].

An ideal TERS probe would consist of a nanoparticle that produces a high electric field enhancement with a resonance wavelength that is tunable over a wide wavelength range by varying the particle geometry. This will ensure high TERS signal. Furthermore, the spot size should be small across the tunable wavelength range to give high spatial resolution. The following sections discuss the optical properties of nanoparticles and their suitability as TERS probes.

2.3 Nanoparticles

2.3.1 Spheres

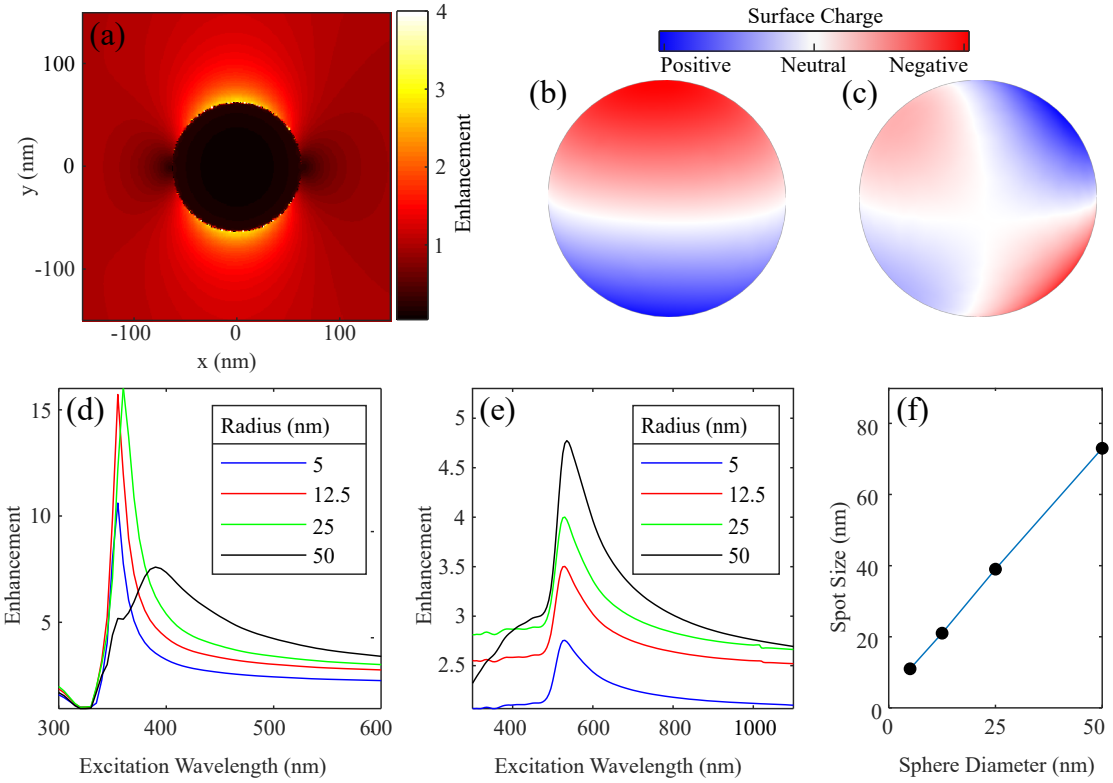

Figure 2.4: Optical simulation results for silver and gold nanospheres. (a) Enhancement map for a gold nanosphere with a 25 nm radius. (b-c) Surface charge plots representing the first and higher-order plasmon modes. (d-e) Enhancement spectra of silver and gold nanospheres respectively. (f) The spot size below the apex of silver nanospheres as a function of sphere radius.

The sphere geometry is illustrated in Figure 2.2(a) and is defined by the radius r. The optical simulation results in Figure 2.4(a) shows an enhancement map for a gold nanosphere with a radius of 25 nm. The plane wave is incident with a polarisation aligned with the y-axis, which excites the fundamental dipole resonance of the nanosphere. The hotspot below the lowest z position of the nanosphere shows an electric field enhancement of 4. This means that the electric field strength is 4 times greater than the incident plane wave excitation. These hot spots can be used as near-field probes for techniques such as TERS [8, 25], microscopy [95, 96] and maskless lithography [97].

The near-field spectra for silver nanospheres are shown in Figure 2.4(d). A surface charge plot of the fundamental localised surface plasmon mode is shown in (b) corresponding to the spectral peak of the 25 nm radius silver sphere excited at 360 nm. The fundamental localised surface plasmon mode is identifiable by the single node in the vertical axis. The enhancement

spectral peak is redshifted slightly from 355 nm to 360 nm when moving from a 5 nm to a 25 nm radius nanosphere. With a 50 nm radius, the resonance wavelength becomes 390 nm. The rate of redshifting has increased with radius. This indicates that retardation effects are beginning to occur, meaning that the particle excitation phase varies significantly across the particle as its size approaches the excitation wavelength [98]. To redshift the resonance wavelength by 45 nm, the sphere radius must be increased by 45 nm. This implies that only minor tuning of the plasmon resonance of nanospheres is possible, which is consistent with the literature [72]. Thus, single nanospheres do not satisfy the resonance wavelength tunability criteria for use as TERS probes.

The surface charge for a higher-order mode is shown in Figure 2.4(c), which corresponds to the 50 nm radius silver nanosphere excited at 355 nm. As a higher-order mode, the current is more strongly confined below the surface, resulting in higher plasmon dampening [99]. This explains why the spectral peak associated with this higher-order mode has a lower enhancement than the spectral peak of the fundamental mode at 390 nm. For gold nanospheres, only the fundamental mode is observed. The higher-order modes that were observed for silver nanospheres are absent for gold nanospheres as they are suppressed by the high imaginary permittivity below 500 nm (Figure 2.3). Comparing the gold and silver nanospheres shows that silver nanospheres produce over double the electric field enhancement. The resonance wavelength of the silver nanosphere is approximately 200 nm shorter.

The spot size (FWHM) on the surface of a substrate 1 nm below a silver nanospheres is plotted against the radius in Figure 2.4. The spot size increases linearly as nanosphere radius increases, which is consistent with the literature [100]. The spot size is a useful metric as it predicts the achievable resolution for imaging techniques such as TERS and near-field microscopy.

In summary, only minor control over near-field resonance wavelength is achievable by tuning the nanosphere radius. In addition, the spot size increases as the radius increases, reducing the achievable resolution. Hence, nanospheres are not well suited for TERS applications since the spatial resolution and resonance wavelength are both dependent on radius.

2.3.2 Nanorods

The geometry of the nanorods simulated in this section is illustrated in Figure 2.2(b) and is defined by the radius of the end segments r and the rod length L. The long axis of the nanorods is aligned with the y-axis polarisation as this has been shown in the literature to maximise the optical absorption [101].

The nanorod optical simulation results are shown in Figure 2.5. An enhancement map is shown in (a) for a 200 nm long gold nanorod with a 25 nm radius excited at the resonance wavelength of the fundamental longitudinal plasmon mode. The enhancement spectra of silver nanorods are shown in (f) and the surface charge plots corresponding to the spectral peaks are shown in (b-d). Multiple spectral peaks are visible for each geometry. For example, the 100 nm long nanorod with a 5 nm radius (black trace) achieves maximum enhancement with the first-order longitudinal mode at 710 nm excitation, shown in (b). The presence of one node in the vertical axis identifies this as the first-order, or fundamental, longitudinal mode. For

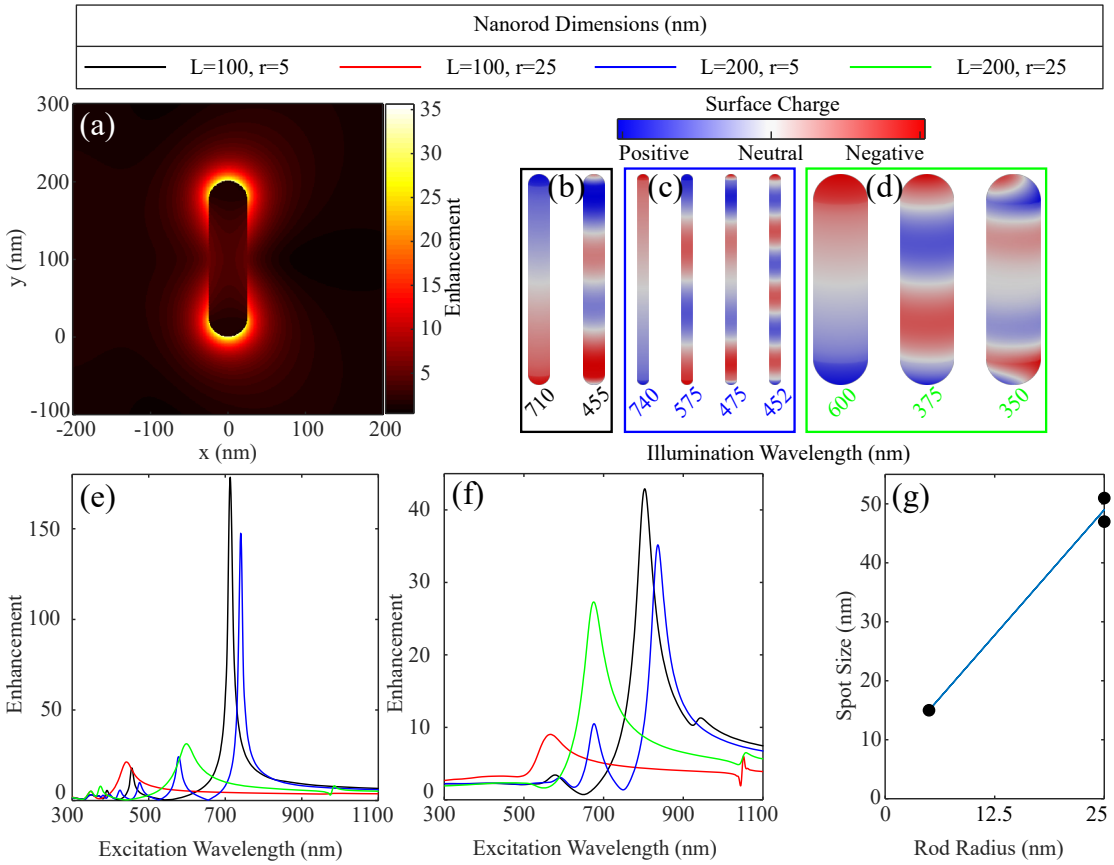

Figure 2.5: Optical simulation results for silver and gold nanorods. (a) Enhancement map for a gold nanorod that is 200 nm long with a radius of 25 nm. (b-d) Surface charge plots of nanorods with the geometry given in the legend and the illumination wavelength given below each plot. (e-f) Enhancement spectra of silver and gold nanocones respectively. (g) Spot size as a function of rod radius.

the same nanorod, a second spectral peak is visible at 455 nm. The presence of multiple nodes indicates this is a higher-order longitudinal mode. A similar analysis of the other nanorods leads to the conclusion that the fundamental longitudinal mode produces the highest near-field enhancement. This is a consequence of higher-order modes being more strongly confined inside the structure, leading to greater energy loss [39]. The number of longitudinal modes increases with length and decreases with radius. For example, the 100 nm long silver nanorod with a 5 nm radius (black trace) only supports two identifiable longitudinal plasmon modes, shown in (b). The 200 nm long silver nanorod of the same radius (blue trace) supports four identifiable longitudinal plasmon modes that are shown in (c). Longer particles will allow for higher degrees of quantization of charge density oscillations, explaining the number of plasmon modes seen for each geometry presented.

The fundamental longitudinal mode is red-shifted as nanorod length increases. This can be seen in Figure 2.5(f) where the 100 nm long nanorod (red trace) has a fundamental resonance at 440 nm and the 200 nm long nanorod (green trace) at 600 nm. This is due to decreased charge

separation restoration forces as the separation between the charges increases [39]. If antenna theory is applied to the nanorods, the dipole mode that is analogous to the fundamental longitudinal plasmon mode should occur when the particle length is half the excitation wavelength. This is not the case for silver or gold nanorods. For example, the 100 nm long silver nanorod with a 5 nm radius has its fundamental near-field resonant peak at 710 nm or $\lambda/7$. Furthermore, the redshift observed for the fundamental longitudinal mode of the 5 nm radius nanorods is significantly smaller than for the 25 nm radius nanorods for both silver (f) and gold (e) nanorods. This is because the finite skin depth at optical frequencies is of the same order as the nanoparticle dimensions, which results in currents below the particle surface that experience loss. This is in contrast to microwave and radio antennas where the skin depth is negligible compared to the physical dimensions, resulting in an almost perfect conductor [98]. The deviation of nanoparticles from $\lambda/2$ resonance means that simple linear models that estimate resonance wavelength from particle length are not sufficient. Instead, the three-dimensional geometry of the particle must be considered, which requires techniques such as finite element methods or boundary element techniques.

Gold has a higher imaginary permittivity than silver, especially below 550 nm as shown in Figure 2.3. This dampens any localised surface plasmons below this wavelength, which is evident in Figure 2.5(e) where no spectral peaks are observed below 550 nm. Silver on the other hand has a low imaginary permittivity across the visible spectrum and hence supports plasmon modes for these wavelengths. From 550 nm up to near-infrared wavelengths, gold has a low imaginary permittivity and plasmon modes exist. The higher permittivity of gold also explains the lower electric field enhancement of gold nanorods compared to equivalent silver ones.

Figure 2.5(g) shows the spot size below silver nanorods at near-field resonance as a function of radius. Increasing nanorod radius increases the spot size, as was the case with nanospheres. The rod length had no effect on spot size for the 5 nm radius nanocones but had a small effect at a radius of 25 nm where increasing the rod length from 100 nm to 200 nm resulted in a 4 nm (9%) larger spot size. The spot sizes were identical for gold and silver nanocones and appear to be material independent. The minimal effect of nanorod length on spot size allows the near-field resonance to be tuned using nanorod length with a minimal resolution penalty.

From the above results, nanorods are superior to nanospheres for use as TERS probes as they produce higher near-field enhancement and allow tuning of the resonance wavelength with minimal spot size increase. In TERS applications, nanorods are expected to result in a high return signal power at a specific wavelength with a resolution on the order of 10 nm.

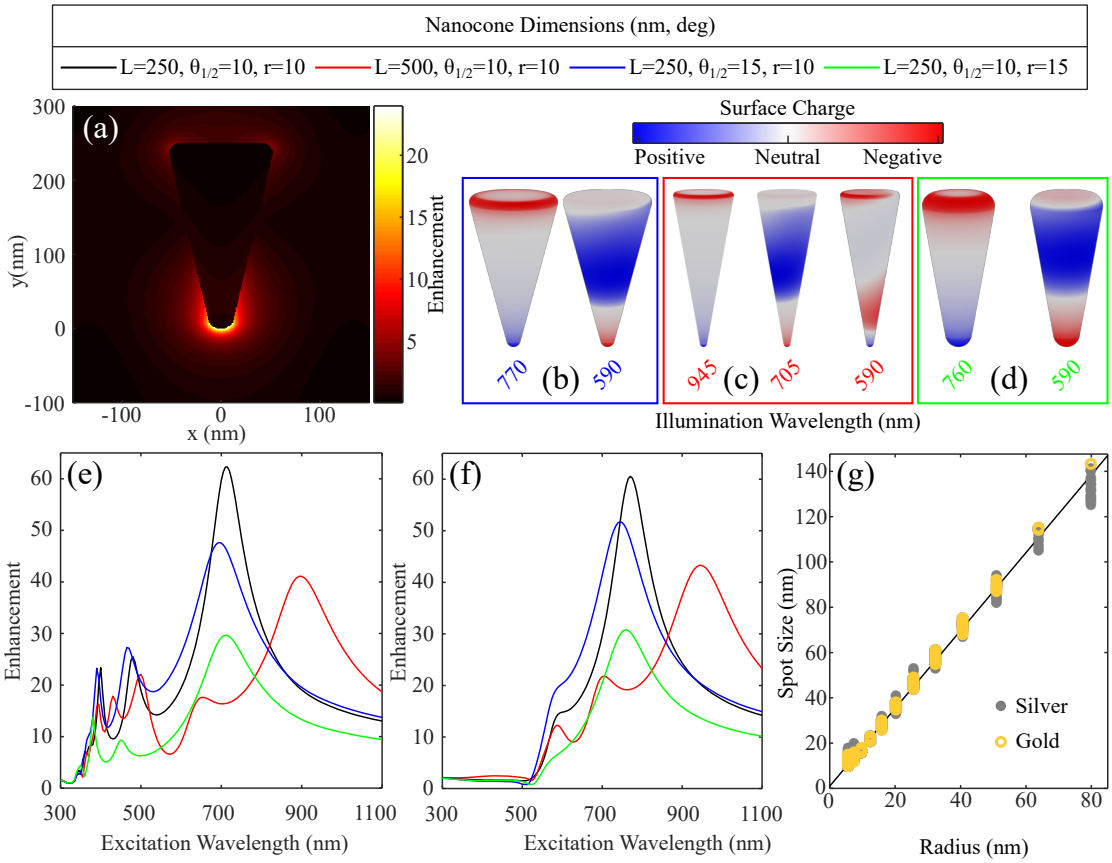

Figure 2.6: Optical simulation results for silver and gold nanocones (a) Enhancement map of a gold nanocone that is 250 nm long with a 10^o angle and a 15 nm apex radius. (b-d) surface charge plots for gold nanocones with geometry given in the legend. (e-f) Enhancement spectra of silver and gold nanocones respectively. (g) Spot size versus apex radius of curvature. Each data point represents a unique combination of length, angle and radius. Only the radius is a strong predictor of spot size and is material independent.

2.3.3 Nanocones

The nanocone geometry is illustrated in Figure 2.2(c) and is defined by the apex radius r, cone angle θ and length L. The nanocone optical simulation results are given in Figure 2.6. An enhancement map is shown in (a) where the highest enhancement is located at the apex.

The spectra for a range of rounded gold nanocones are shown in Figure 2.6(f). The spectral peaks were identified and the charge distributions are shown in (b-d). The excitation wavelength of the fundamental mode is dependent on the longitudinal particle length. For example, the fundamental plasmon resonance wavelength of gold nanocones is red-shifted from 770 nm to 945 nm when the length is increased from 250 nm (black trace) to 500 nm (red trace). Furthermore, as the nanocone particle length changes, the near-field amplitude is affected. The near-field plasmon enhancement for gold nanocones is significantly reduced below 550 nm, which is due to the high imaginary permittivity at these wavelengths. There is also a decrease in near-field plasmon enhancement for silver and gold nanocones as the length is increased from 250 nm (black trace)

to 500 nm (red trace). Figure 2.3(a) shows that the imaginary permittivity of silver is relatively constant for the resonance wavelengths of these two nanocones. Hence, the decreased near-field resonant amplitude must be due to decreased restoring forces as the electron separation is increased. In addition, decreasing the sharpness of the probe by increasing the apex radius ($L = 250\,\text{nm}$, $\theta_{1/2} = 10$ and $r = 15\,\text{nm}$) or the angle ($L = 250\,\text{nm}$, $\theta_{1/2} = 15^o$ and $r = 10\,\text{nm}$), leads to a lower enhancement. This is despite the fact that the fundamental mode for these two geometries is blue-shifted to regions of lower imaginary permittivity. The maximum near field enhancement for the nanocones is approximately 20 greater than spheres, further supporting the importance of tip sharpness. Finally, the number of spectral peaks increases with particle length, as was observed for nanorods.

Figure 2.6(e-f) shows that silver and gold nanocones exhibit similar near-field enhancement for wavelengths above 550 nm. However, for shorter wavelengths only silver provides significant enhancement. This is due to the high imaginary permittivity of gold below 550 nm. It is expected that shorter length gold nanocones will allow high electric field enhancements tuned down to at least 600 nm. Below this, significant enhancement will not be possible.

Figure 2.6(g) shows the spot size at the near-field resonance of gold and silver nanocones as a function of radius. The spot size is proportional to the nanocone radius and independent of length and angle. This allows the resonance wavelength to be tuned using nanocone length while maintaining a small spot size.

The mechanical strength of a nanocone is superior to a nanorod. With nanorods, the radius must be large enough to ensure adhesion to the AFM probe, which imposes a resolution limit. For nanocones, the radius can be kept small and the adhesion area is proportional to length and angle.

From the work presented in this section, it remains unknown how nanocone length, radius and angle numerically effect the near-field resonance wavelength and enhancement. It is also unclear what the dimensions of an optimal TERS probe are. These concepts will be discussed in Chapter 3.

2.3.4 Pyramid Nanoparticles

The geometry used to investigate pyramid nanoparticles is illustrated in Figure 2.2(d) and is defined by the apex radius r, angle θ, length L and number of sides on the base n. All edges were rounded to a radius of 3 nm to avoid sharp edges that are problematic for boundary element simulations. The pyramid nanoparticle optical simulation results are shown in Figure 2.7. An enhancement map for a triangular pyramid is shown in (a). The enhancement spectra of silver and gold pyramid nanoparticles are shown in (f-g) respectively. For gold pyramids, the number of base sides has a negligible effect on electric field enhancement and resonance wavelength. However, for silver, there is a dramatic increase in the electric field enhancement, from 40 for a triangular pyramid to 210 for a hexagonal pyramid. Furthermore, there is a slight redshift as the number of base sides increases.

The gold pyramids all exhibit near-field enhancements of over 100. This is significantly higher than the equivalent size gold nanocone, which exhibited an enhancement of 60. This indicates

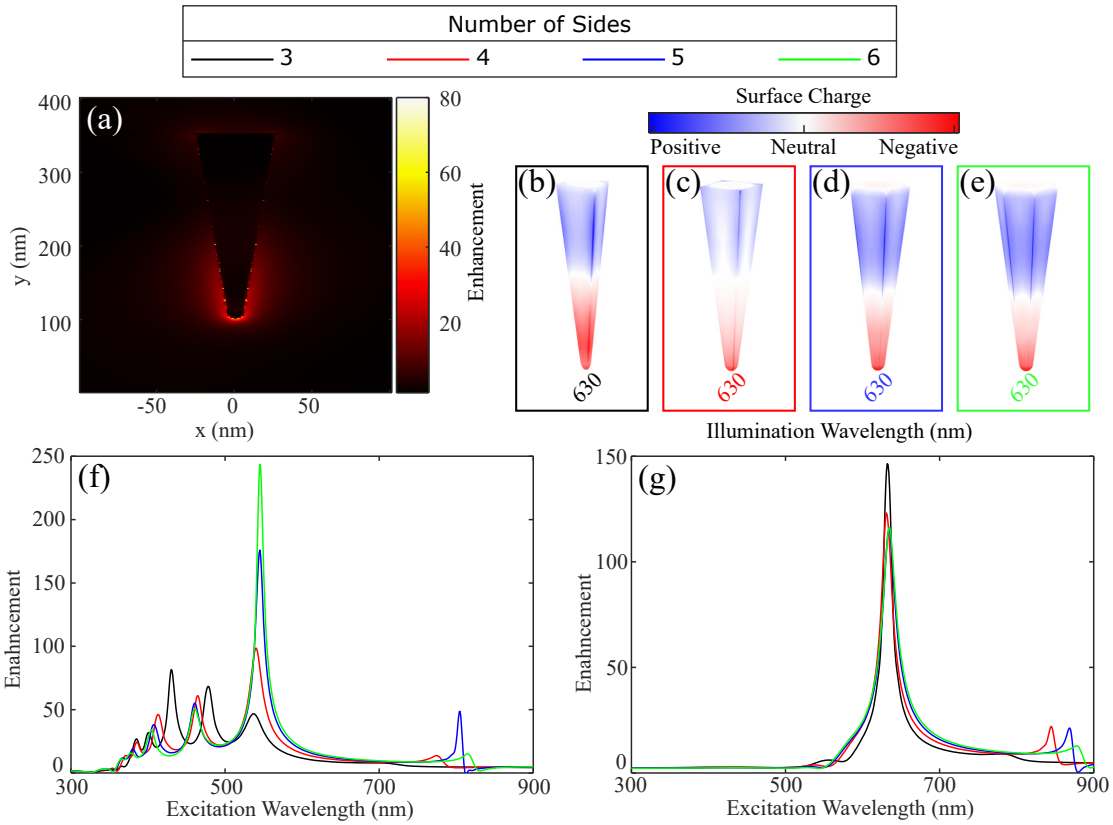

Figure 2.7: Optical simulation results for silver and gold nanopyramids with different numbers of sides. (a) Enhancement map of a silver nanopyramid with 3 sides. (b-e) Surface charge plots of pyramids with 3-6 sides excited at their resonant frequency. (f-g) Enhancement spectra of silver and gold nanopyramids respectively.

that the sharp edges of the pyramid structure increase the near-field enhancement. Hence, the performance of pyramid nanoparticles is superior to nanocones. However, it is worth noting that the sharp edges of the pyramid nanoparticles would require a higher resolution manufacturing process than the nanocones presented previously.

2.3.5 Summary

Single metallic nanospheres are not suitable for constructing tunable TERS probes as only small variations in the resonance wavelength can be achieved. Furthermore, larger spheres result in larger spot sizes and reduced TERS resolution. Nanorods offer a significant improvement over nanospheres. The near-field enhancement is larger and the near-field resonant peak can be tuned with rod length while the spot size is unaffected. However, the low mechanical strength due to the small binding area to an AFM tip is expected to result in a fragile TERS probe. Nanocones allow the near-field resonance wavelength to be tuned with length, angle and radius. If the length is varied and the radius is kept constant then the spot size will be unaffected. Due to the larger dimensions at the base, nanocones have superior mechanical strength compared to nanorods. Pyramid nanoparticles offer the highest performance of any theoretical nanoparticle presented in this section. However, the manufacturing requirements are significantly more complex than nanocones.

From the near-field spectra for sphere, rod and cone nanoparticles, some conclusions can be made:

- Increasing geometrical complexity, i.e. breaking symmetry, increases the number of plasmon modes. Hence, complex shapes are more likely to give field enhancement over a broad range of excitation wavelengths.
- The wavelength of the fundamental mode increases with particle length, but not at a fixed ratio like an antenna.
- Nanoparticle sharpness increases near-field enhancement due to tighter charge confinement at the particle apex.
- Plasmons are highly suppressed when the imaginary component of the permittivity (ϵ_I) is high. This makes silver a superior plasmon material to gold over the visible spectrum. However, the low ϵ_I of gold around 700 nm allows strong plasmon resonances to occur.

2.4 Metal Layer Thickness

Commercially available TERS probes are silicon AFM tips coated with a thin layer of metal. Adding layered structures to boundary element method simulations increases the computational complexity and adds another parameter during the design stage for TERS probes. However, due to the short skin depth of gold and silver at optical wavelengths, any penetrating fields will be highly attenuated. Thus, it was expected that after a certain metal coating thickness, the optical response would converge to that of a solid nanoparticle. In this section, the effects

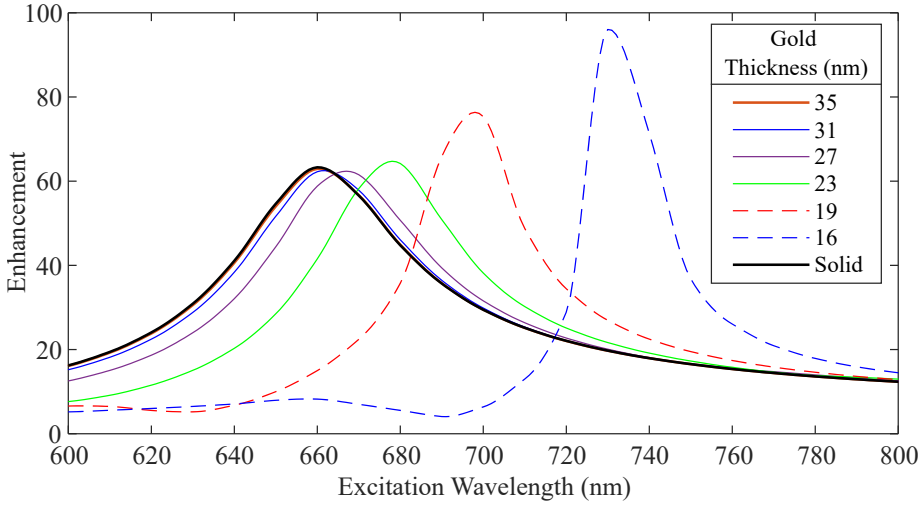

Figure 2.8: Near-field enhancement spectra for silicon nanocones coated in varying thicknesses of gold.

of metal layers are investigated, as opposed to the solid metal nanoparticles discussed in the previous sections.

Gold nanocones were simulated with an internal silicon nanocone. The average coating thickness was calculated as the mean distance of corresponding points on the gold and silicon nanocones.

Figure 2.8 shows the near-field enhancement spectra for various thicknesses of gold coatings on silicon nanocones. The near-field spectrum for thin layers is significantly different from a solid nanocone, but as the gold coating thickness increases, the near-field spectrum converges to that of a solid gold nanocone. For a gold coating thickness of 35 nm, the near-field enhancement spectrum is almost identical to that of a solid gold nanocone. Note that the solid cone spectrum does not match the spectrum for an equivalent nanocone shown in Figure 2.6(f) because a rougher particle discretisation was used here to offset the increased computation time introduced by the layered structure.

Figure 2.9(a) shows the peak near-field enhancement as a function of gold coating thickness. A thin gold layer results in a higher enhancement. As gold thickness is increased, the enhancement converges to that of a solid nanocone. A gold thickness of 23 nm produces an enhancement that is approximately the same as a solid gold nanocone.

Figure 2.9(b) shows the resonance wavelength as a function of gold coating thickness. The resonance wavelength is inversely proportional to the gold thickness until converging to the resonance wavelength of a solid gold nanocone after approximately 30 nm.

A thin gold coating increases near-field enhancement, resulting in an increased TERS signal. However, coating an atomic force microscope tip with a thin, smooth and uniform coating of gold is problematic as discussed in Chapter 1.5. On the other hand, off-the-shelf gold-coated AFM tips are available. Using focused ion beam milling, a gold cap at the end of the tip could be produced and would resemble the gold-coated nanocones presented in this chapter. This manufacturing process could be simpler than producing a solid tip, which is discussed further

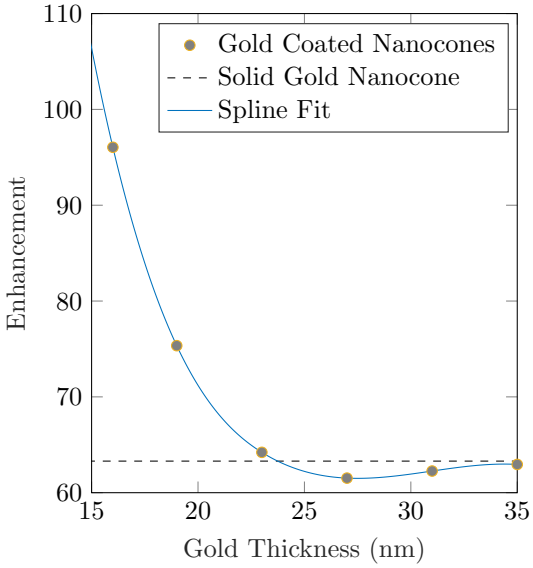

(a) Enhancement.

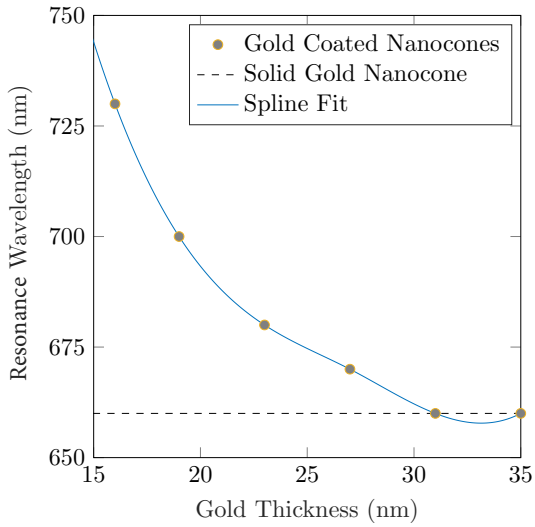

(b) Resonance wavelength.

Figure 2.9: The spot size (a) and resonance wavelength are plotted for various gold coating thicknesses on a silicon nanocone corresponding to the near-field enhancement spectra shown in Figure 2.8.

in Chapter 6.

2.5 Illumination Parameters

In this section, the effects of excitation laser beam waist and focus position are shown. Figure 2.10 shows the problem space for these simulations where a Gaussian excitation is defined by

$$I(z,x) = I_0 \left(\frac{\omega_0}{\omega(x)}\right)^2 exp\left(\frac{-2z^2}{\omega(x)^2}\right), \tag{2.5.1}$$

with beam waist radius ω_0, distance from the centre axis z and axial distance from the focus x.

Figure 2.11(a) shows the enhancement spectra for a silver nanocone excited with varying beam waists. Although the beam waist values are well below the diffraction limit, these small focal spots allow smaller problem spaces to be used and trends can still be identified. As the beam waist increases, the number of modes excited increases. This can be seen by moving from 10 nm to a 40 nm beam waist, where two additional spectral peaks at 375 nm and 425 nm are produced. Furthermore, as the amount of energy coupled into the particle increases with a wider beam, the resulting near-field amplitude also increases.

In Figure 2.11(b) the enhancement spectra for a silver nanocone excited by a Gaussian excitation with a 20 nm beam waist and a varying focus position are shown. For $Z = 0$, the beam is focused at the tip apex and a dominant mode is seen at 500 nm with a much weaker secondary mode at 425 nm. For $Z = 20$, the beam is focused above the tip apex, and the two modes have reversed in their relative amplitudes, with the 425 nm one dominating. Increasing

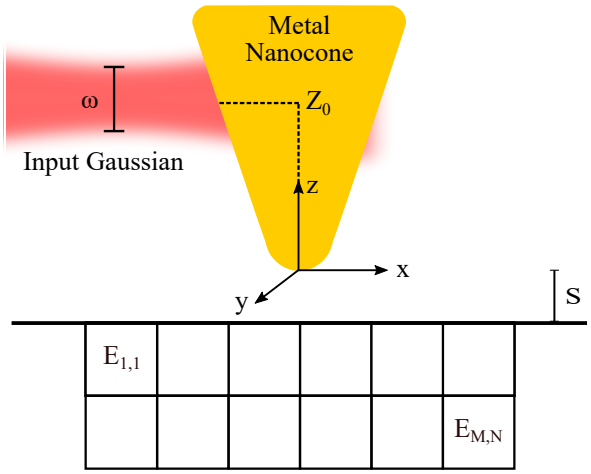

Figure 2.10: x-z Cross-section of the simulation space, consisting of a vacuum with an embedded nanoparticle defined by an outer boundary. The tip is positioned with the bottom vertex at the origin, a distance s above an M x N measurement grid where the electric field is measured. The near-field enhancement is determined from the maximum electric field value on the upper row of the grid. The input beam is a Gaussian defined by the beam width ω where the electric field drops to $1/e$ of its maximum value, and the focal point on the nanocone Z_0.

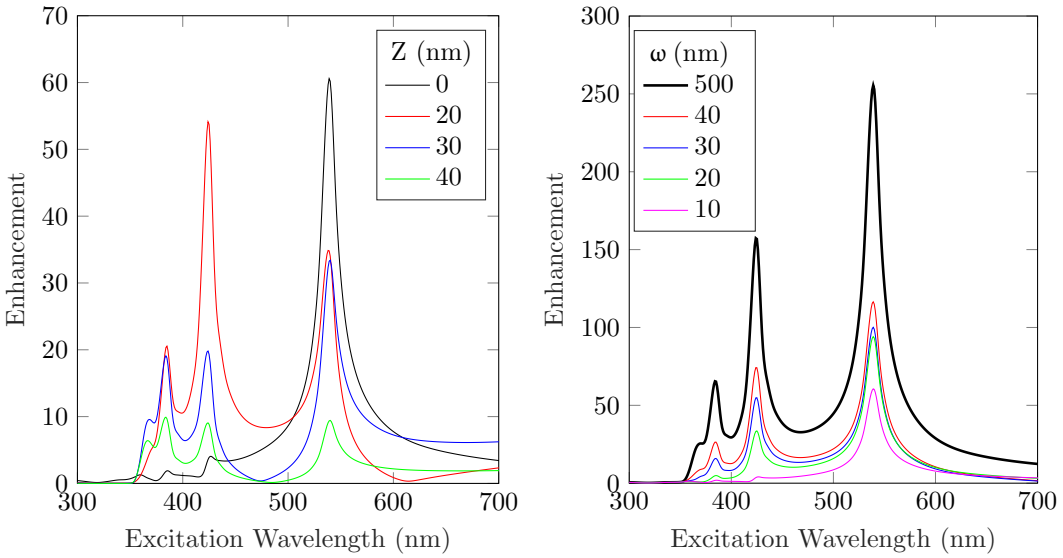

(a) Beam waist.

(b) Beam position

Figure 2.11: Near-field spectra for silver nanocones excited with a Gaussian beam (a) focused at tip apex with a varying beam waist ω, (b) fixed beam waist of 10 nm with varying position Z.

Z continues to shift the relative amplitudes. However, the maximum amplitudes decrease as the beam is focused further from the tip apex. These results are consistent with experimental electron energy loss spectroscopy results [102].

The resonance wavelength of the nanocone is constant regardless of position or beam width as shown in Figure 2.11. Hence, excitation beam parameters cannot be used to tune the resonance wavelength of a nanoparticle. Instead, the nanoparticle geometry must be optimised.

In Figure 2.12 the effects of polarisation and incidence angle can be seen. (a) Shows z-polarisation that is parallel to the cone axis. (b) Shows x-polarisation, perpendicular to the cone axis. (c) Shows y-polarisation that is perpendicular to the cone axis. Out of these three cases, z-polarisation that is parallel to the cone axis yields the highest enhancement. This is consistent with the literature [84].

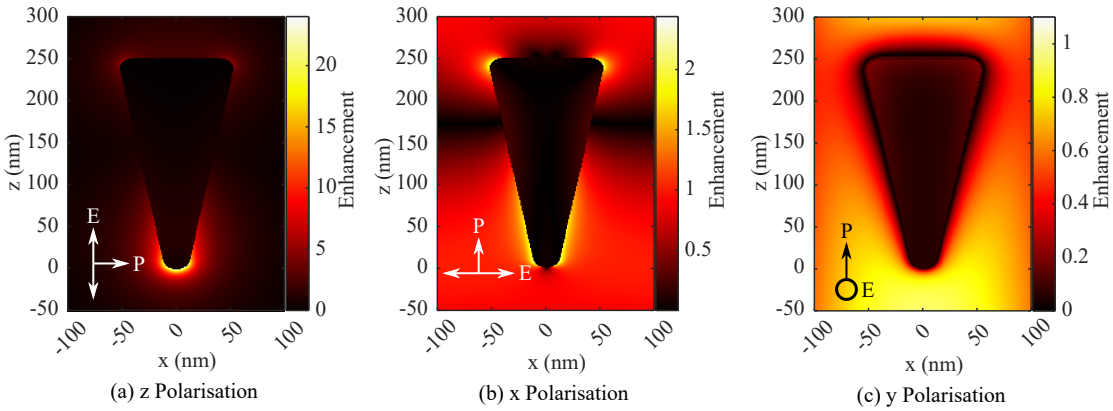

Figure 2.12: Electric field enhancement for a silver nanocone excited at the fundamental longitudinal resonance mode, using various propagation directions and polarisations. The electric field polarisation E is shown for each case and the second arrow gives the propagation direction P. The circle represents a direction out of the page. The $\hat{z}$ polarisation is parallel to the nanocone axis and results in the highest electric field enhancement. Thus, the remaining work in this thesis will only consider incident electric field polarisation that is parallel to the long axis of a nanoparticle.

Practically, these results indicate that a focused beam with a beam waist similar to the particle size should be used if the broadest near-field response is desired. Furthermore, the polarisation should be aligned with the nanocone axis for maximum enhancement.

2.6 Applicability to TERS

From the results presented in this chapter, it can be concluded that nanocone particles attached to a silicon AFM tip are well suited to TERS. Nanocone probes provide high electric field enhancement when made of silver or gold and the resonance wavelength can be tuned independently of spot size by varying the particle length. They also offer high TERS resolution and can be attached securely to a silicon AFM tip. The nanoparticles should be fully illuminated with a focused laser to give the broadest near-field response. Furthermore, the polarisation should be aligned with the nanocone axis for maximum enhancement.

Nanocones have a near-field resonance wavelength and enhancement that are dependent on material and shape. Hence, models are required to estimate the design of an optimal nanocone TERS probe for a given illumination wavelength. The following chapter develops these models for silver and gold nanocones using boundary element method simulations.

Chapter 3

Optimising Geometry of Gold and Silver Nanocone Probes

This chapter describes the optimisation of nanocone geometry for TERS applications. The optimisation was performed using the boundary element method and a sweep of nanocone parameters. From the resulting data, numerical models for near-field enhancement and resonance wavelength were obtained. These numerical models estimate of the optimal nanocone dimensions for a given target illumination wavelength. The results are used to fabricate TERS probes in Chapter 6.

Publications Arising from this Chapter:

- L. R. McCourt, M. G. Ruppert, B. S. Routley, S. C. Indirathankam, and A. J. Fleming, "A comparison of gold and silver nanocones and geometry optimisation for tip-enhanced microscopy," *Journal of Raman Spectroscopy*, vol. 51, no. 11, pp. 2208–2216, 2020

Conference Presentation Arising from this Chapter:

- L. R. McCourt, "Resolution and enhancement of probes for nearfield two photon apertureless lithography," in *Nanophotonics and Micro/Nano Optics International Conference 2019*, (Munich), p. 197, Sept. 2019

3.1 Introduction

In this Chapter, boundary element method simulations are used to calculate the near-field resonance wavelength and electric field enhancement of nanocone tips and map the dependencies of tip dimensions and material. This work aims to produce numerical models that describe the optimal geometry of gold and silver nanocones for excitation wavelengths from the visible to near-infrared. Gold nanocones have longer lifetimes than silver nanocones due to improved

chemical stability and therefore, it is of interest to identify the wavelength range where the performance is comparable to silver.

For an LSPR to form, the particle has to be spatially confined in all three dimensions. Furthermore, the particle material needs to have a negative real permittivity and a low imaginary permittivity [39]. Examples of such materials are silver and gold. In addition, LSPR wavelength is dependent upon material permittivity and particle geometry [18]. Hence, probe geometry needs to be adjusted so an LSPR exists at the illumination wavelength.

The current industry-standard tip for near-field applications consists of a silicon AFM tip with a silver coating which forms a grainy surface. A scanning electron microscope image of one such tip is shown in Figure 3.1. The discrete metal grains provide particle confinement and silver meets the permittivity requirements, most notably having low loss across the visible spectrum [105]. However, there are several disadvantages associated with these probes. Firstly, the random nature of grain formation [21,106] results in an inconsistent electric field enhancement and near-field resonance wavelength. Secondly, to ensure a nanoparticle at the tip apex, a thick metal coating is required, which decreases the optical and topographic resolution. For the tip shown in Figure 3.1, the apex radius of 45 nm will result in an optical resolution of approximately 90 nm. Thirdly, there is often an issue with collocation, where the enhanced near-field is not located at the AFM tip apex. In the case of TERS, this results in an offset between Raman and topography maps [107]. Finally, silver nanoparticles tarnish rapidly in laboratory conditions, exhibiting a decreased absorption coefficient by one order of magnitude over 36 hours and a redshifting near-field resonance wavelength of 1.8 nm/hr [20]. Thus, silver-based tips have lifetimes limited to approximately one day, which is prohibitive given the significant set-up time associated with optical alignment that must be performed for each new tip. To extend the lifetime, a passivation layer may be added. However, this increases the separation between the plasmonically active silver and the sample resulting in decreased near-field enhancement, optical and topographic resolutions.

An alternative tip consists of a metallic nanocone attached to the end of a silicon AFM probe. This design was illustrated in Figure 1.10, with the electric field enhancement surrounding the gold nanocone shown in Figure Figure 1.10(a) and the enhancement perpendicular to the cone axis, below the apex, shown in 1.10(b). These nanocones can be manufactured using focused ion beam milling with consistent surface topography, producing more consistent electric field enhancement and near-field resonance wavelengths [108]. In addition, the nanocone apex is both the source of near-field enhancement and the mechanical apex, which removes the collocation issue. Furthermore, these nanocones can be produced with apex radii of approximately 10 nm, providing superior optical and mechanical resolution to commercially available silver coated tips. Finally, nanocone geometry can be altered to shift the LSPR to the excitation wavelength [18], allowing the use of alternative materials with higher chemical stability than silver.

As nanoparticle material and geometry affect the LSPR wavelength and near-field enhancement, the material and shape of the nanocone tips need to be optimised for a required optical wavelength. In contrast to spheres and ellipsoids, no analytic solutions for the optical response of nanocones exist [39]. Hence, computational methods are needed to optimise nanocone geometry.

Previous studies have investigated the optical performance of geometries similar to the

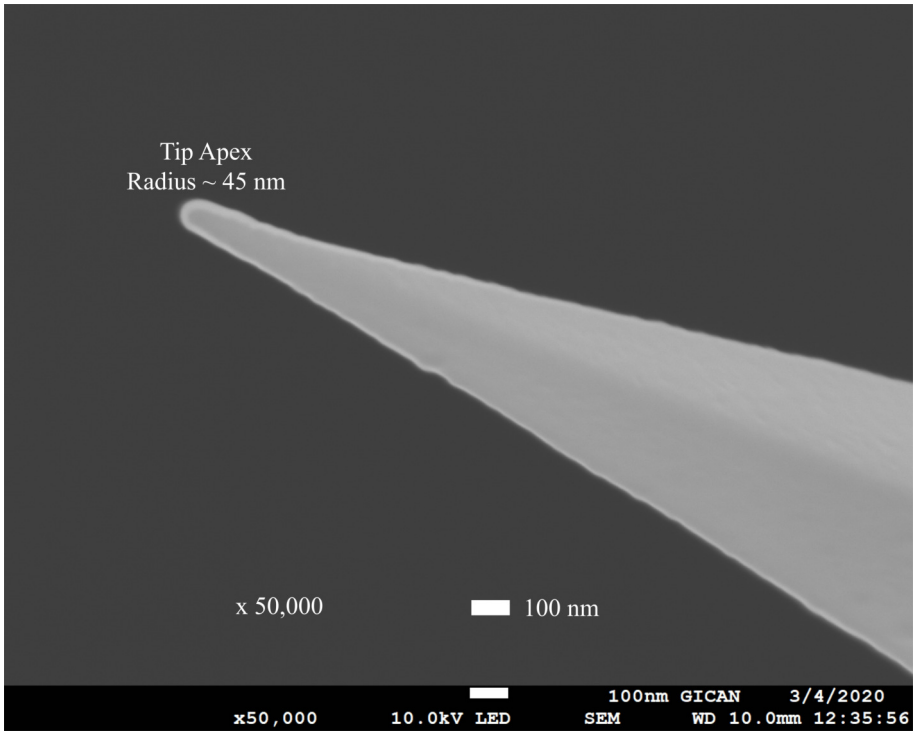

Figure 3.1: Scanning electron microscope image of a commercially available silver coated AFM TERS tip. The apex radius is approximately 45 nm

nanocone considered here. However, some have only considered a single excitation wavelength, which does not allow the near-field resonance wavelength and peak enhancement to be identified [80,84,86,109,110]. Others use quantities other than near-field enhancement such as optical extinction [72, 110] or antenna efficiency [111]. However, simulation allows direct calculation of electric field enhancement and the effects of material and geometry to be investigated. Furthermore, by considering limited nanocone geometry parameters, studies have failed to produce generalised models of near-field resonance wavelength and enhancement in the visible spectrum [82, 112].

In this chapter, BEM simulations are used to model the plasmon responses of gold and silver nanocones over visible and near-infrared wavelengths. Results from a large number of length, radius and cone angle combinations are used to produce empirical models. These models allow estimation of the resonance wavelength and enhancement for a given nanocone design.

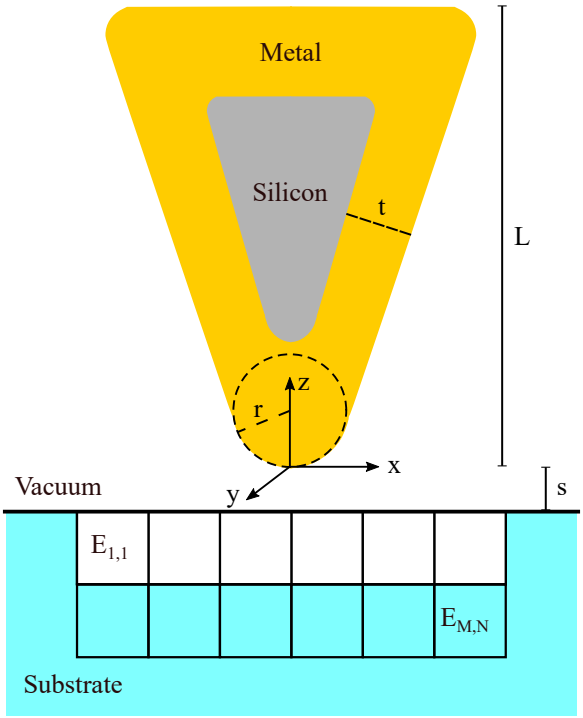

Figure 3.2: x-y cross-section of the simulation space, consisting of a vacuum with an embedded nanocone tip defined by an outer boundary with length L, radius of curvature r, and apex angle θ. The tip is positioned with the bottom vertex at the origin, separated a distance s above a substrate of 1.5 refractive index. Electric field values are calculated over an 1 x N grid located 10 nm below the substrate surface.

3.2 Method

3.2.1 Tip Performance Metrics

Two metrics for tip performance are used throughout this work. Firstly, the electric field enhancement, referred to as 'enhancement', is $E_{\text{enh}} = E_{\text{res}}/E_{\text{exc}}$ where E_{res} is the maximum electric field strength in the plane 1 nm below the sample surface, perpendicular to the cone axis and E_{exc} is the electric field strength of the excitation beam, which is set to 1 V/m. A high enhancement is desirable as the ratio of near-field to far-field increases. An example electric field map for a nanocone is plotted in Figure 1.10(a). The second metric, spot size, is the full width half maximum of the electric field in the plane 1 nm below the sample surface, perpendicular to the cone axis. A smaller spot size improves resolution in near-field applications. An example spot size calculation is illustrated in Figure 1.10(b).

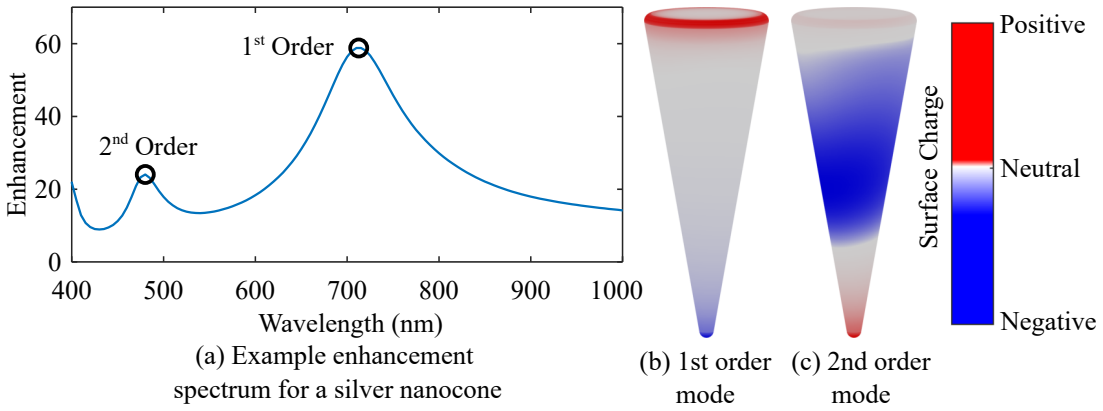

Figure 3.3: Enhancement spectrum of a silver nanocone 1 nm above a glass substrate. The (a) 1st and (b) 2nd order longitudinal modes are identified from the surface change plots.

3.2.2 Boundary Element Method Simulations

The boundary element method (BEM) package, metallic nanoparticles using BEM (MNPBEM) [91, 92], was used to solve Maxwell's equations in the frequency domain for gold and silver metallic nanocone structures above a lossless glass substrate. The problem space is described in Figure 3.2. The particle boundaries consist of boundary elements which are defined by a set of vertex positions and normal vectors. Measured dielectric functions [94] for gold or silver were used inside the boundary. The substrate was assumed to be a lossless material with a refractive index of 1.5, approximating glass. A plane wave excitation E_{exc} was used, propagating in x with y polarisation, a configuration that has been shown to maximise enhancement [84]. Particle geometry was varied using combinations of particle length L, radius of curvature r and apex angle θ.

For each tip geometry, the near-field resonance wavelength was identified by the maximum electric field enhancement. The order of each mode was identified from the surface charge distribution, with the order corresponding to the number of zero surface charge nodes in the y-axis. Examples of 1$^{\text{st}}$ and 2$^{\text{nd}}$ order longitudinal modes are shown in Figure 3.3. For consistency, only results for the 1$^{\text{st}}$ order mode are given for each nanocone.

3.3 Results

For nanocones of silver and gold located 1 nm (s=1 nm) above a glass substrate, the near-field resonance wavelength was identified and the enhancement at this wavelength was calculated 1 nm below the glass surface (a total of 2 nm below the tip apex). The results of this are shown in Figure 3.4 with each data point representing a unique nanocone geometry defined by the radius, angle and length on the xyz axis. Figure 3.4(a) shows the near-field resonance wavelength for silver nanocones. Enhancement spectra for the boxed data points, A1-A4, are shown. The enhancement achieved at the near-field resonance wavelength of each silver nanocone is shown in Figure 3.4(b) and the enhancement spectra for the boxed data points, B1-B4, are

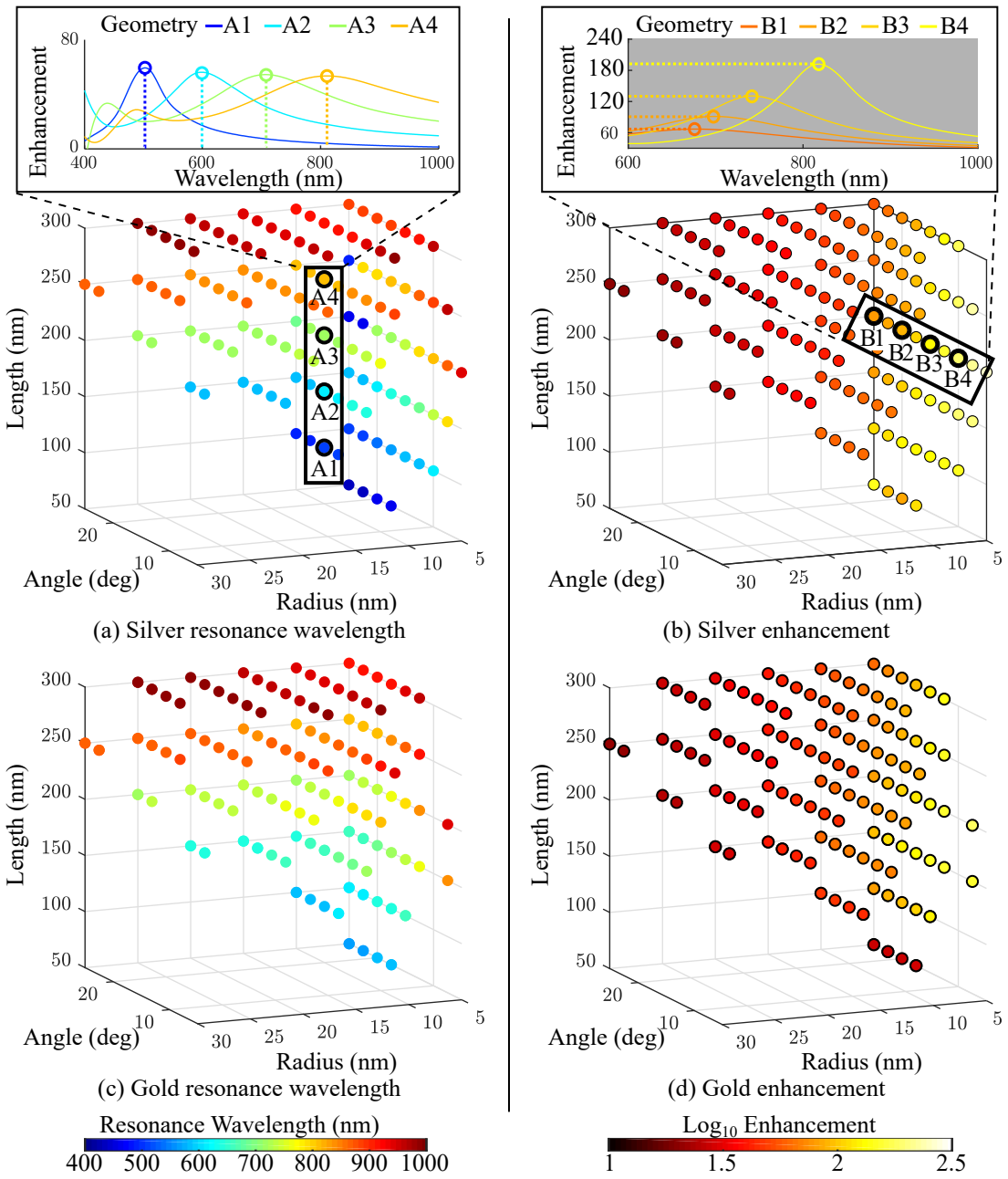

Figure 3.4: The simulated optical responses of silver and gold nanocones 1 nm above a glass substrate, measured 1 nm below the glass surface are given with example spectra in the top plots. (a) silver and (c) gold show the near-field resonance wavelengths of nanocones. The wavelength scale is in the bottom left. The near-field resonance wavelength is redshifted when moving to longer lengths and smaller angles. (b) silver and (d) gold show the electric field enhancement of nanocones. The enhancement scale is in the bottom right. A high enhancement can be observed for nanocones with small radii and cone angles.

shown. Similarly, the near-field resonance wavelengths and corresponding enhancements for gold nanocones are shown in Figures 3.4(c) and (d) respectively. An empirical model can then be used to describe the near-field resonance wavelength and enhancement as a function of length, half angle, and radius, in the range of interest.

Fitting a linear regression model using a least squares algorithm to the near-field resonance wavelength data yields:

$$\lambda_{\text{res}}\,(\text{nm}) = \begin{cases} 610 + 1.5L - 7.1\,\theta + 0.3r, & \text{Gold} \\ 460 + 1.9L - 7.0\,\theta + 1.1r, & \text{Silver,} \end{cases} \tag{3.3.1}$$

where λ_{res} is the near-field resonance wavelength in nm, the radius is in nm and the angle in in degrees. This fit allows for accurate predictions of the near-field resonance wavelength with less than 5% error for both materials when compared to the simulated results. The coefficients reveal that increased length or apex radius induce a redshift of the near-field resonance wavelength, while increased angle produces a blueshift. There is a trend where larger radii cause a blueshift for short nanocones, but a redshift for long nanocones. This averages to a slight redshift as radius increases. However, the shifts due to radius are small compared to the shifts associated with length and angle, especially given the small range of radii considered here (5-30 nm).

In addition, the near-field resonance wavelength of gold is 150 nm longer than silver with the same geometry. As a result, even when short nanocones are used, the near-field resonance wavelength of gold nanocones cannot be realistically tuned below 630 nm.

A non-linear optimisation was used to determine the following enhancement models:

$$E_{\text{enh}} = c_1 e^{-2\gamma} + c_2, \tag{3.3.2}$$

where c_1 is770 and 930, and c_2 is 27 and 32 for gold and silver respectively and $\gamma = (r\theta)^{1/2}$ where r is in nm and θ is in radians. The models capture the trend well with a root mean squared error (RMSE) in enhancement of 12.

The enhancement models are shown (Equation 3.3.2), together with the simulated enhancements in Figure 3.5. Enhancement is increased when tip apex angle and radius are small, in effect when the tip is sharp. This differs from hemisphoid ellipses where enhancement is dependent on the short to long axis ratio [86, 113]. Equation 3.3.2 is length independent, which indicates an increased tip length does not decrease the enhancement at least across the particle lengths considered here and when restricted to the first-order longitudinal mode.

Gold nanocones have been manufactured in [108], where the length and far-field scatter resonance wavelengths were measured, while a range of cone angles are given. In Figure 3.6, the near-field resonance wavelength model for gold nanocones (Equation 3.3.1) is compared with this experimental data. Probable bounds on the experimental cone angle give a range of near-field resonance wavelengths for a given nanocone length. The model fits the data well, with 4% of the data points falling outside the models predictions. This indicates the simulated data and subsequent linear regression model are valid. A particular near-field resonance is typically redshifted from the same resonance observed in the far-field due to retardation effects which

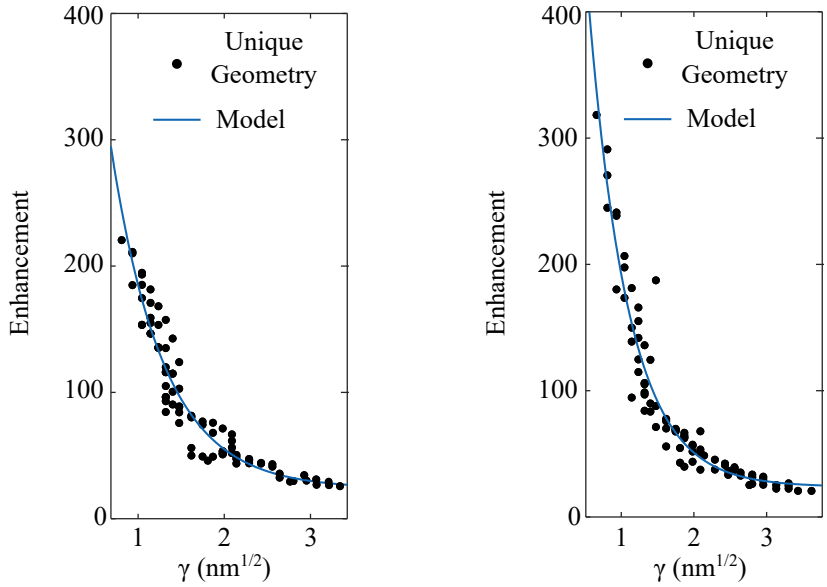

Figure 3.5: The enhancement of each nanocone geometry is plot as a function of γ (black) for (a) gold and (b) silver where $\gamma = (r\theta)^{1/2}$ where r is in nm and θ is in radians. Each data point represents a unique nanocone geometry. The enhancement model (Equation 3.3.2) is overlaid (blue) and captures the data well. The highest enhancements occur when gamma is small, or the nanocone is 'sharp'.

become significant as particle size approaches the excitation wavelength [98, 114]. In this study, the particle widths are small compared to the near-field resonance wavelengths, hence there will be a small shift between the near-field and far-field resonances.

Furthermore, the experimental data [108] measures nanocones terminated on a glass substrate which will shift the resonance wavelengths. This limits the validity of a direct comparison between the experimental data [108] and the data acquired through simulations. However, due to a lack of experimental near-field resonance data for gold nanocones this was necessary.

The termination of metal nanocones onto the larger AFM cantilever has been shown to affect the near-field enhancement, with an increased refractive index red-shifting near-field enhancement [115]. Figure 3.7 compares the near-field enhancement spectra for a gold coated tip which forms a cap, and a gold nanocone. The cap structure results in a 30% greater peak enhancement and a resonance that is blueshifted 15 nm.

Given the significant increase in computation time when including the silicon structure and the small wavelength shift, only freestanding metal nanocones were modelled in the parameter sweep. Equation 3.3.1 can be modified by including the 15 nm blueshift in the constant term. Hence, the models become:

$$\lambda_{\text{res}}\,(\text{nm}) = \begin{cases} 595 + 1.5L - 7.1\,\theta + 0.3r, & \text{Gold} \\ 445 + 1.9L - 7.0\,\theta + 1.1r, & \text{Silver,} \end{cases} \tag{3.3.3}$$

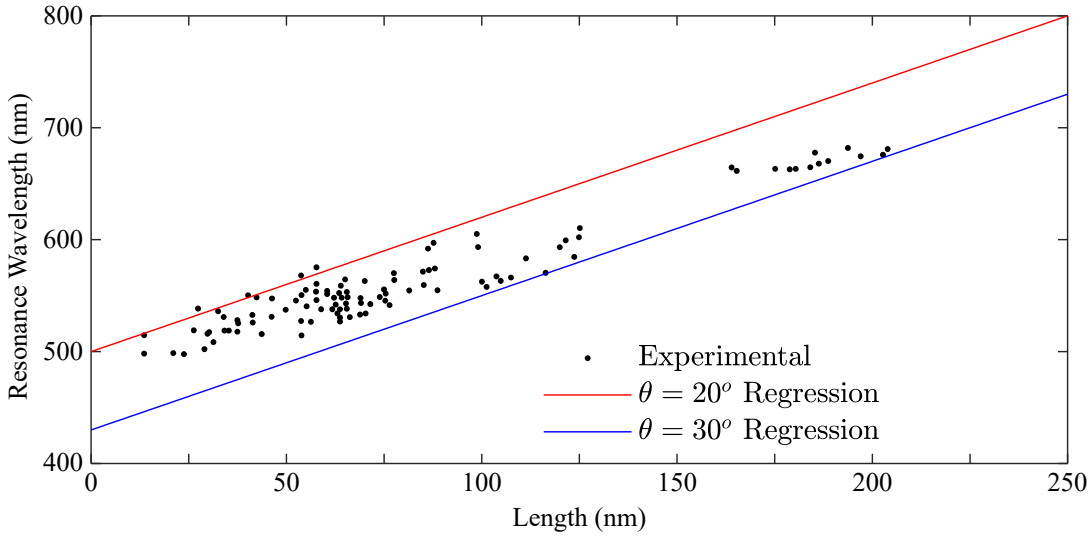

Figure 3.6: The experimental far-field resonance wavelength for gold nanocones (black) [108] is plot and compared to the near-field resonance wavelength model (Equation 3.3.1). Estimates for maximum and minimum cone angle were chosen as 30^o and 20^o and radius kept at 10 nm, resulting in upper (blue) and lower (red) estimates from the model respectively.

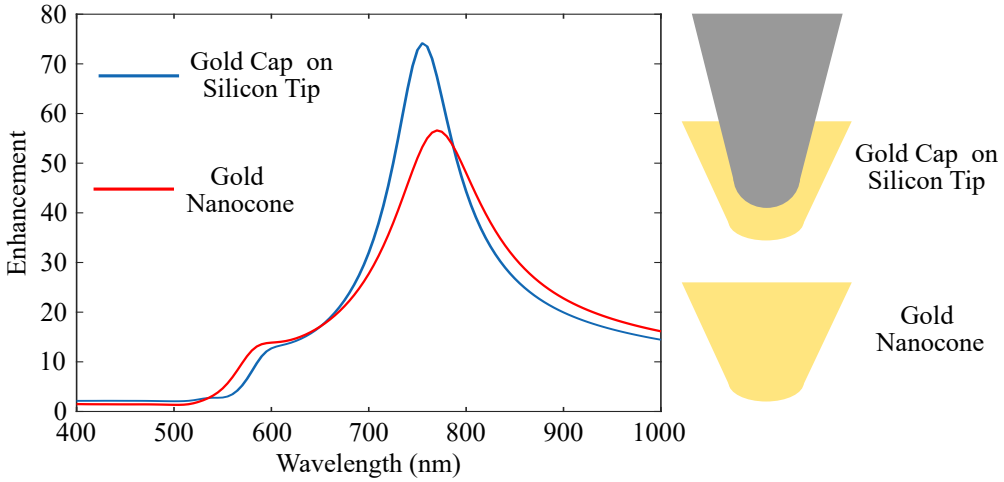

Figure 3.7: Near-field spectra for a gold coated silicon tip apex (cap) and gold nanocone. The gold cones are both 250 nm long with a radius of curvature of 10 nm and a cone angle of 10^o.

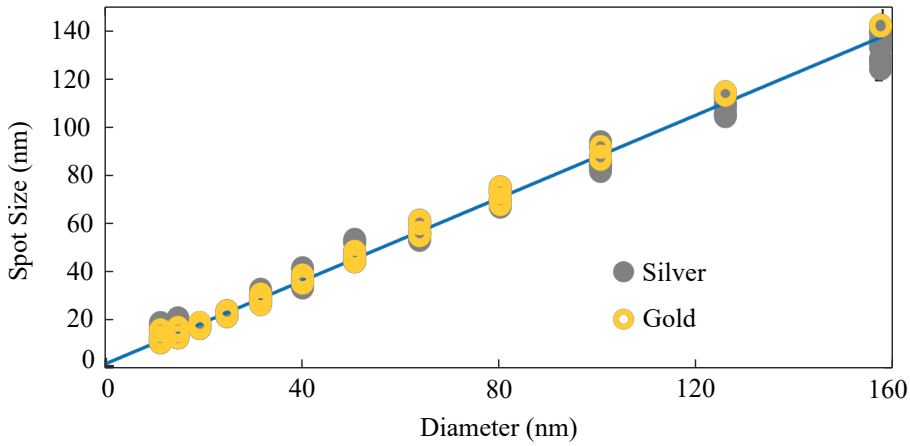

Figure 3.8: Near-field spot size (FWHM) as a function of radius for gold and silver nanocones. The spot size is measured 1 nm below the apex with each data point representing a unique nanocone geometry. The radius is observed to be the dominant determinant of spot size. The linear fit is Spotsize(nm) $= 1.72r + 1$.

The empirical functions that describe trends in the resonance wavelength and enhancement provide a starting point for the tip design process. The desirable characteristics of small spot size and high enhancements are most closely associated with a small tip radius combined with a small tip angle; therefore, these should be minimised within the limits of the available manufacturing process.

Then, the resonance wavelength can be tuned with nanocone length. Optimised length and material combinations are given in Table 3.1 for commonly used wavelengths in TERS.

Figure 3.8 shows the spot size as a function of radius, with a single linear fit capturing both the silver and gold data set. Multiple data points at a given radius are for different combinations of length and apex angle, however, the position of these data points within a group could not be predicted. The spot size was found to be independent of length, apex angle and material (gold or silver), with the apex radius being the only strong predictor. The spot size being proportional to radius is consistent with previous results [100, 116] and so the radius should be minimised.

As gold has a relatively low imaginary permittivity, it provides a similar near-field enhancement to silver, provided the geometry is appropriate and offers the same resolution capabilities. Due to superior corrosion resistance, gold nanocone tips appear to be better suited for imaging and lithography applications in the 633-900 nm wavelength range. Outside this range, the comparatively low enhancement may limit their use.

It is worth noting that an increased substrate refractive index will result in a red-shifted nanocone near-field resonance [83]. Hence, the wavelength ranges suggested here are limited to use with substrates similar to glass with refractive indices around 1.5. For high refractive index substrates, the use of gold nanocones may be restricted to longer wavelengths.

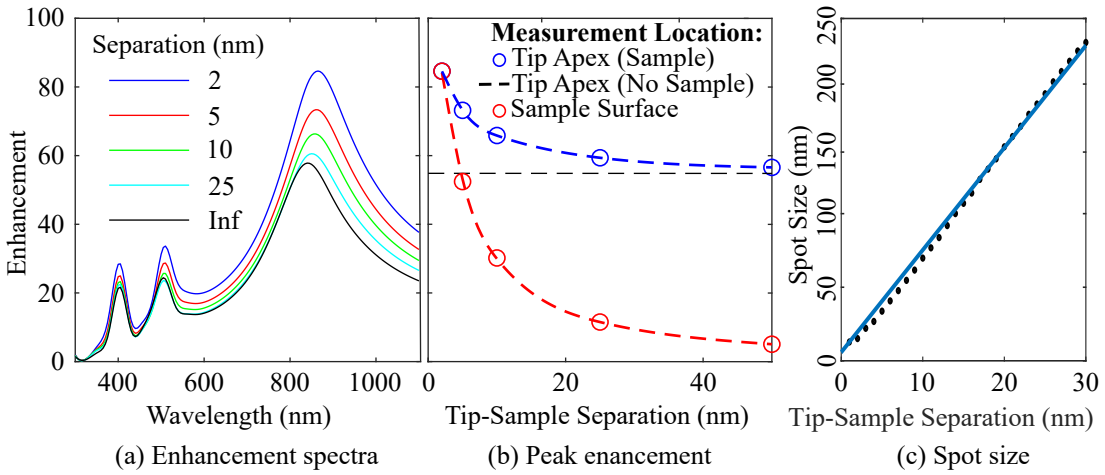

Figure 3.9: The effects of increasing tip-sample separation for a 250 nm silver nanocone with a radius of 10 nm and an angle of 10 degrees, for: (a) electric field enhancement spectra. (b) electric field enhancement as measured 1 nm below tip apex (blue), 1 nm below the sample surface (red) and with the no sample (infinite tip-sample separation) case included as a reference (black). (c) the near-field spot size measured 1 nm below the sample surface (FWHM). The linear fit approximates the dependence of spot size on tip-sample separation.

3.3.1 Tip-Sample Separation

In this section, the effects of tip-sample separation are investigated in terms of enhancement, location of spectral peaks and the spot size for nanocone tips.

Figure 3.9(a) shows the enhancement spectra for nanocones, calculated 1 nm below the tip apex, at multiple tip-sample separations. As the sample is brought closer to the tip, the strongest spectral peak is redshifted and increases in amplitude. This effect is further explored in Figure 3.9(b) which shows the enhancement as a function of tip-sample separation 1 nm below the tip apex and at the sample surface. As the tip-sample separation increases, the enhancement below the tip apex decreases asymptotically towards the enhancement seen when there is no sample present. The enhancement at the sample surface decays towards 1 as the tip-sample separation increases, a trend consistent with experimental results [16, 53, 82, 95, 117, 118]. This shows that a small tip-sample separation increases the enhancement at the sample through two mechanisms. First and most significant, the sample being closer to the tip decreases the distance over which the evanescent field can decay. Secondly, there is an amplification of the near-field enhancement, which is evident as the enhancement measured at the tip apex increases when the tip-sample separation is decreased. This is due to the formation of a tip image in the substrate, increasing the dipole strength [83]. Thus, for enhancement and resolution, the tip-sample separation should be minimised. Figure 3.9(c) shows that spot size increases linearly as a function of tip-sample separation from 0-30 nm typical in TERS. This is consistent with previous work [110]. Thus, for high enhancement and resolution, the tip-sample separation should be minimised.

Table 3.1: Recommended nanocone material, length and cone angle combinations for common wavelengths in near-field lithography (785 nm) and TERS (633 and 514 nm) given a radius of 10 nm. The nanocone lengths are given by equation 3.3.3.

Wavelength (nm)	Material	Angle (deg)	Length (nm)	Enhancement
785	Gold	20	220	45
		30	267	34
633	Silver	20	167	54
		30	204	42
	Gold	20	118	45
		30	164	35
514	Silver	20	104	54
		30	141	42

3.4 Conclusion

This Chapter describes a numerical method for optimising the enhancement and resonance wavelength of metallic nanocones for applications such as tip-enhanced Raman spectroscopy. The boundary element method is utilized to simulate the optical response of many metallic nanocones with unique combinations of length, half-angle, and radius. Tip-sample separation is also considered. The materials of interest are gold and silver; however, the presented method is applicable to any metal.

The results show well-defined trends between each geometry parameter and the resulting resonance wavelength and tip-enhancement. Empirical functions are fitted to simulation results which describe the major trends. These empirical functions are useful for predicting performance and determining the optimal geometry for a given application.

For tip-enhanced Raman spectroscopy, gold nanocones are found to have a similar near-field enhancement to silver nanocones at red and near-infrared wavelengths. This is significant as gold has far superior corrosion resistance to silver, which could potentially increase the probe lifetime from hours to days or weeks. However, gold nanocones do not provide competitive enhancement below 633 nm, so silver nanocones are expected to be a better choice for applications requiring these wavelengths. This work highlights that the choice of material is strongly dependent on the required operating wavelength. Nanocones are also predicted to have significantly improved resolution compared to metal coated tips due to the smaller tip radius.

The numerical models developed in this chapter are used to design optimised gold nanocone TERS probes that are fabricated in Chapter 6.

Chapter 4

Experimental Methods and Equipment

This chapter describes experimental techniques used throughout this thesis that are not discussed in the following chapters.

4.1 Atomic Force Microscopy

Atomic force microscopy (AFM) allows the topography of a surface to be characterised with sub-nanometre resolution [119, 120]. AFM is suitable for a broad range of samples from soft samples such as DNA [121] and living cells [122] to stiff samples such as graphene [123], silicon and metals [124]. AFM is used for TERS measurements due to the ability to precisely control the tip-sample separation.

AFM probes typically consist of a sharp tip located at the end of a cantilever, which is scanned over the sample surface. The cantilever deflection is measured using the optical deflection method where the position of the laser beam is measured after it is reflected off the cantilever onto a four-quadrant photodetector. A feedback loop is used to maintain a constant deflection signal by varying the nanopositioner z-position as the sample is scanned in the x-y plane. The z-axis controller output as a function of x-y position is used to generate a topography estimate of the sample.

There are several AFM modes of operation that allow the surface topography to be measured such as contact and tapping modes. For contact mode, there is no cantilever excitation and the tip remains in contact as it is scanned across the sample [125]. In general, contact mode results in higher shear forces that increase the likelihood of sample damage and tip contamination [46,126]. For these reasons, contact mode was not used in this thesis.

Alternatively, an atomic force microscope can be operated with tapping mode where a piezo-acoustic actuator at the cantilever is used to excite the cantilever at its resonance frequency [127].

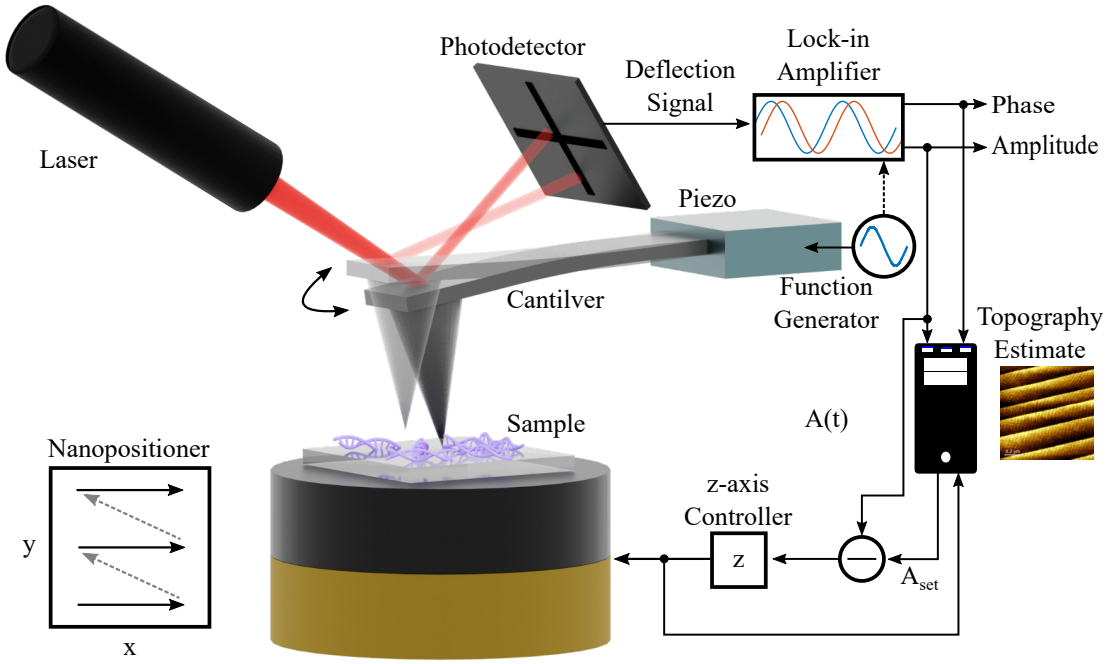

Figure 4.1: Schematic of an atomic force microscope being operated in tapping mode.

A schematic of an atomic force microscope operating in tapping mode is shown in Figure 4.1. A lock-in amplifier demodulates the cantilever deflection signal to measure the oscillation amplitude [128]. The amplitude setpoint is usually specified as a percentage of free-air amplitude. Over an oscillation cycle, the cantilever tip only briefly touches the sample leading to lower force tip-sample interactions, which makes the tapping mode especially useful for soft or fragile samples [126]. Furthermore, the tapping mode is sensitive to surface properties such as elasticity and viscosity, which allows these properties to be measured.

4.2 Raman Spectroscopy

Confocal Raman spectroscopy is used to measure the bulk Raman response of samples before attempting TERS. For example, during the preparation of single-walled carbon nanotube samples, confocal Raman microscopy was used to confirm the presence of the radial breathing mode with 638 nm and 785 nm illumination. For the work presented in this thesis, a Horiba XploRA Plus confocal Raman microscope was used with 532 nm (green), 638 nm (red) and 785 nm (infrared) lasers.

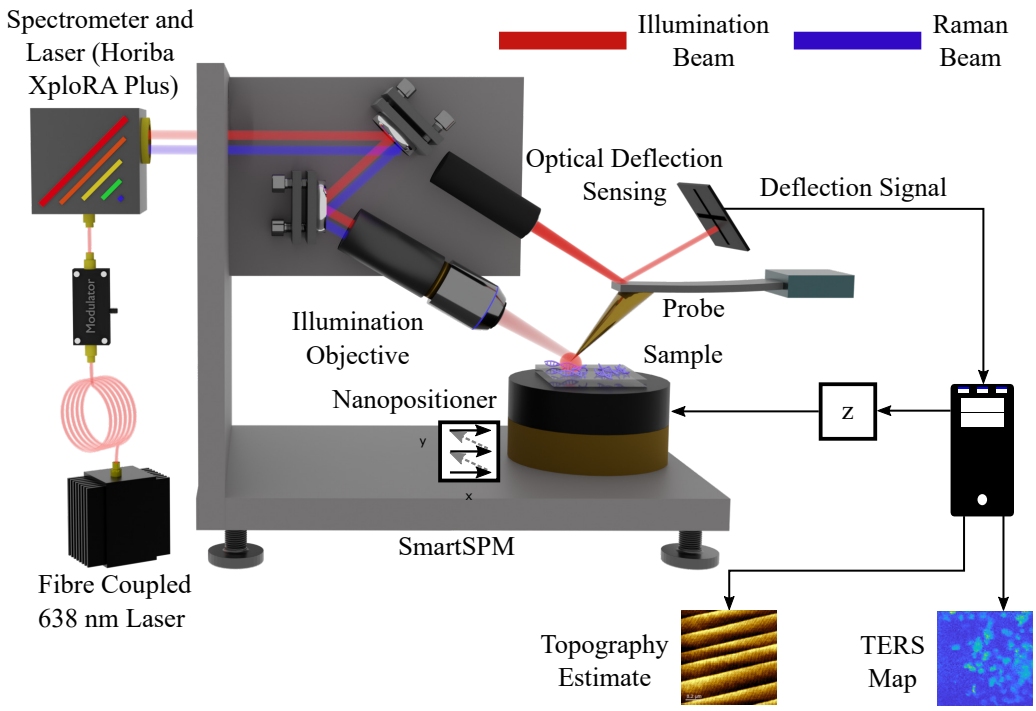

Figure 4.2: Schematic of the experimental setup used for contact and hybrid mode TERS. The AFM system is an AIST-NT atomic force microscope and the Raman microscope including the lasers and spectrometer are contained in the Horiba XploRA Plus unit. The side illumination requires TERS probes with the access tip geometry as shown. The modulated illumination is achieved with an external fibre coupled 638nm laser and acousto-optic modulator.

4.3 Tip Enhanced Raman Spectroscopy

The theoretical concepts of TERS were introduced in Chapter 1.4. A schematic of the experimental setup is shown in Figure 4.2, which consists of a Horiba XploRA Plus Raman microscope and a Horiba SmartSPM scanning probe microscope. The Raman microscope contains 538, 638 and 785 nm laser sources. However, the 638 nm laser failed and was replaced with an external, 638 nm, fibre coupled laser (IPS #I0638SB0025PA). A fibre acousto-optic modulator (Gooch & Housego FIBER-Q) was used to modulate the 638 nm laser while performing modulated-illumination intermittent-contact TERS, which is discussed in Chapter 7. The illumination beam is focused onto the tip apex using a 100x, 0.7 numerical aperture, side-illumination objective lens. The Raman scattered light is collected by the side objective lens and the spectral components of the scattered light are measured with the spectrometer built in to the Raman microscope. A photograph of the 638 nm laser focused onto a TERS probe is shown in Figure 4.3(a).

TERS can be performed using several AFM modes of operation, such as contact or tapping modes. In tapping mode, the illumination beam can be modulated or the spectrometer can be time-gated to reduce far-field contributions to the measured signal. In this thesis, a hybrid imaging mode is used where the movement between pixels and topography measurements are

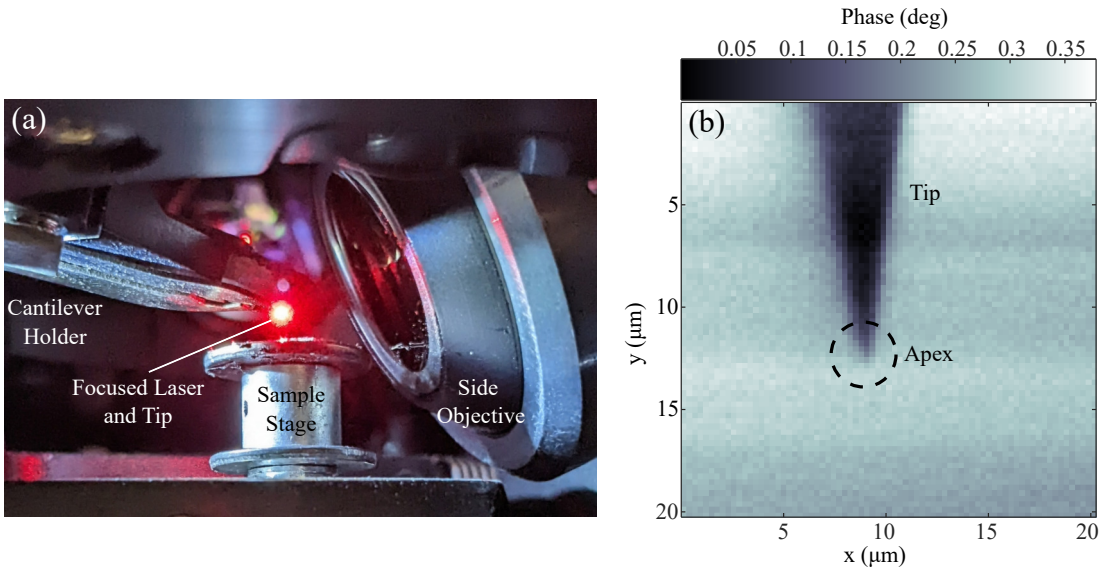

Figure 4.3: (a) Photo of a TERS probe being illuminated with the 638 nm laser. (b) Phase map of a TERS probe as a function of x-y side objective position, which is used to align the laser to the apex.

performed with tapping mode while the Raman spectrum at each pixel is acquired in contact mode. A discussion of the benefits and disadvantages of the different modes is presented in Chapter 7.

The optical alignment is performed by visually positioning the laser spot onto the tip using a camera and the side objective lens. The cantilever is then driven at its resonance frequency, and a phase map is acquired as a function of the objective x-y position as shown in Figure 4.3(b). The cantilever phase is affected when the laser is focused onto the tip and allows the laser to be directed to the apex. Finally, the probe is landed onto a sample and the alignment is fine-tuned to maximise the Raman signal. This is the standard alignment procedure for the microscope.

4.4 Raman and TERS Post-processing

4.4.1 Background Removal

Practically, a Raman spectrum will likely consist of the desired signal containing Raman peaks, noise and broad fluorescence. The fluorescence background may be reduced by tuning microscope parameters or changing the sample preparation. Alternatively, there are several post-processing approaches that do not require experimental modification and importantly do not require modification of the sample. In this work, two algorithms are used depending on the particular requirement of the experiment.

Firstly, I-ModPoly is an iterative polynomial fitting algorithm with automatic peak detection [129]. Spectral peaks above the sum of the noise level and the fitted polynomial are removed from subsequent background fits. This method is superior for fluorescence background removal

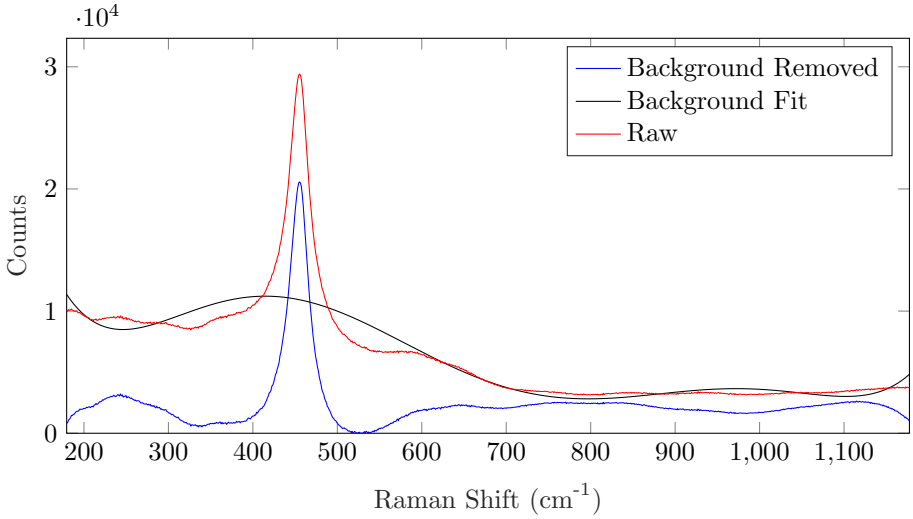

Figure 4.4: I-ModPoly background fit and removal of an example Raman spectrum. The background fit is biased by the spectral peak at 450 nm.

compared to single polynomial fits and supersedes the ModPoly routine. Furthermore, the routine is insensitive to initial polynomial order and is completely automated.

Figure 4.4 shows an example of I-ModPoly being applied to an example Raman spectrum. The fluorescence is effectively removed. However, the algorithm does not remove the entire spectral peak at 450 nm before fitting the background fit to the raw spectrum, which results in a bias in this region..

A second background removal method, adaptive penalised least squares (ALPS) separates a spectrum into two Poisson processes, one being the Raman count and the other the fluorescence background [130]. A cost function is minimised by adjusting the relative weights of both processes point-wise across the spectrum. This algorithm is superior to I-ModPoly and a range of others in most situations. The disadvantage is that a smoothing parameter needs to be manually adjusted.

Figure 4.5 shows an example of ALPS being applied to the same Raman spectrum as the I-ModPoly example above. ALPS more effectively removes the spectral peak before fitting the background, which results in less bias around spectral peaks. In this example, ALPS is more effective in removing the background compared to I-ModPoly.

Figure 4.6(a) shows a Raman map for plastic nanoparticles on a paper substrate with high fluorescence. The fluorescence dominates the map and results in poor contrast of the nanoparticles. Figure 4.6(b) shows the same Raman map after background removal using ALPS. The background removal has greatly improved the contrast and revealed more information about the surface, allowing the identification of more nanoparticles and more accurate measurements of particle size. This demonstrates that background removal is necessary for Raman and TERS imaging, especially for samples with high fluorescence. Furthermore, for samples with multiple spectral peaks, it is necessary to remove the fluorescence background before comparing peak ratios.

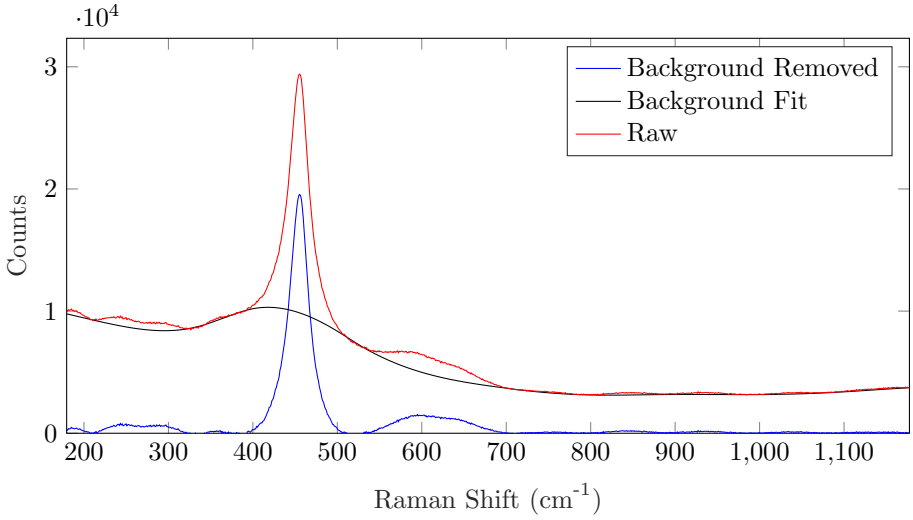

Figure 4.5: ALPS background fit and removal of an example Raman spectrum.

4.4.2 Drift Correction

TERS and Raman signals are sensitive to optical alignment. As the duration of a scan increases, the optical alignment decays. This becomes significant for long acquisition times that are common when mapping surfaces using TERS or Raman spectroscopy. The drift as a function of the slow axis (y-axis) position can be approximated by:

$$d(y) = \sum_{x=1}^{N} \sum_{\lambda_0}^{\lambda_N} B(x, y, \lambda), \tag{4.4.1}$$

where n_x is the x-axis index of the pixel, $B(x, y)$ is the background fit of the pixel located at (x, y, λ) and λ is the wavenumber. Thus, $d(y)$ represents the total number of counts from the Raman spectrometer as a function of slow axis position. The inverse of the drift will give the drift correction function:

$$d^{-1}(y) = \frac{1}{d(y)}, \tag{4.4.2}$$

where $d(y)$ is the normalised drift fit.

A correction matrix C can then be created for an $N \times M$ Raman map:

$$C_N = \begin{bmatrix} \vec{c} & \vec{c} & \dots & \vec{c} \end{bmatrix}, \tag{4.4.3}$$

where $\vec{c}$ is the correction vector:

$$\vec{c} = \begin{pmatrix} d^{-1}(y_1) \\ \vdots \\ d^{-1}(y_M) \end{pmatrix} \tag{4.4.4}$$

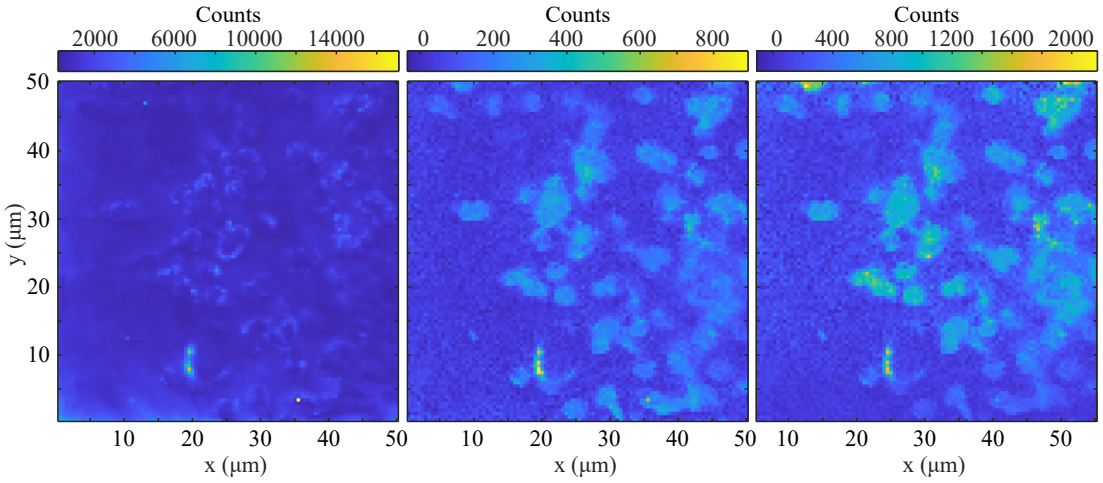

Figure 4.6: Raman maps of plastic nanoparticles at $1578\,\mathrm{cm}^{-1}$ with different levels of post-processing. This sample has a significant fluorescence background. The improvement in the nanoparticle contrast demonstrates the usefulness of background removal and drift correction for samples with significant fluorescence.

With the background removed Raman data in the form:

$$R = \begin{bmatrix} s(x_1, y_1, \lambda_1) & \dots & s(x_1, y_1, \lambda_N) \\ \vdots & \ddots & \vdots \\ s(x_N, y_1, \lambda_1) & \dots & s(x_2, y_1, \lambda_N) \\ \vdots & \ddots & \vdots \\ s(x_1, y_2, \lambda_1) & \dots & s(x_1, y_2, \lambda_N) \\ \vdots & \ddots & \vdots \\ d^{-1}(x_N, y_M, \lambda_1) & \dots & d^{-1}(y_N, x_M, \lambda_N), \end{bmatrix} \tag{4.4.5}$$

the drift corrected Raman data is obtained by:

$$A = C_N \times R \tag{4.4.6}$$

Figure 4.7 shows the drift of a Raman map of plastic nanoparticles as a function of y-axis position. A 2^{nd} degree polynomial is fit to the Raman background, which was found using ALPS. The data is scaled so that the fit to drift line is normalised, shown in red. The inverse of the drift line gives the drift correction, shown in blue. The drift correction was applied to the Raman map in Figure 4.6(b) to produce the drift-corrected Raman map in Figure 4.6(c). The features at high y positions have increased contrast compared to the non-drift-corrected Raman map and allows for more accurate mapping of surfaces.

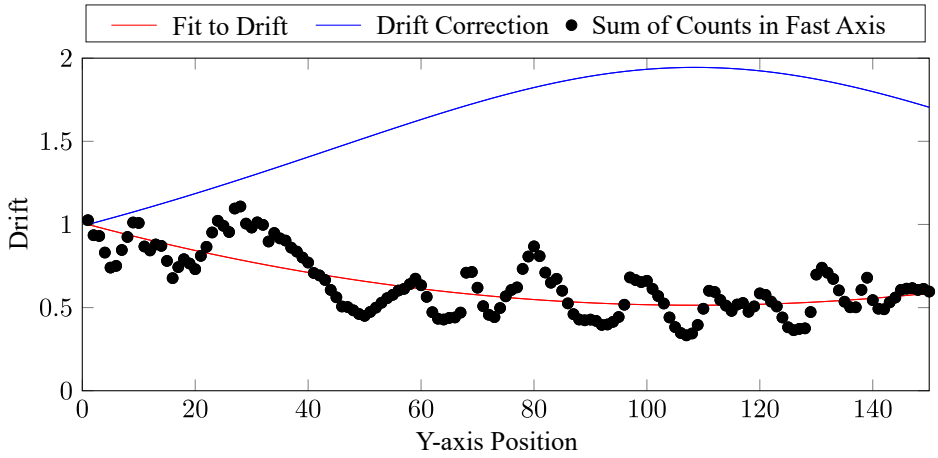

Figure 4.7: An example of drift correction applied to a Raman map of plastic nanoparticles. The sum of Raman signal counts of the background fit in the fast axis is shown as the black data points. With the spectral peaks removed, it is assumed that fluctuations in the background signal are due to degradation of the optical alignment. A second-order polynomial is fit to the sum of counts and is shown as the red curve. The inverse of the drift fit is shown in blue and is applied to the TERS map to compensate for the optical drift.

4.5 Scanning Electron Microscopy

The scanning electron microscope (SEM) provides high-resolution images of a sample. A high-energy beam of electrons is scanned across the sample and the intensity of the scattered electrons forms a high-resolution image. The most commonly recorded signal is that of the secondary electrons, which are liberated as ions are formed in the sample resulting from interactions with the primary electron beam [131].

Although the SEM is a powerful tool, it has several limitations. Firstly, SEM is a destructive imaging technique [132]. Thus, imaging a TERS probe with SEM may cause changes to the surface and alter the performance. For this reason, SEM imaging was usually performed on probes that were not used for TERS. Secondly, charge accumulation will occur for poorly conducting materials as a result of electron injection. The charged sample then deflects the incoming electron beam through a Lorentz force [133]. Hence, imaging poorly conductive TERS probes, such as those with a sparse metal coating, results in a low image quality. Despite the shortcomings of scanning electron microscopy, the high-resolution images obtained when using a conductive sample made this technique the most suitable for imaging TERS tips. In this thesis, a JEOL FE-SEM was used to image TERS probes.

4.6 Energy Dispersive X-ray Spectroscopy

Energy-dispersive X-ray spectroscopy (EDX) measures the elemental composition of a sample at the target of an electron beam. EDX is performed by exciting inner shell electrons to a higher energy state with a beam of focused electrons. When the hole created in the inner shell is filled by an electron from a higher energy state, a characteristic x-ray is created. Each element has unique characteristic x-rays, allowing the elemental composition of a sample to be identified [134].

The characteristic electrons are produced to a depth of about $2\,\mu$m and so EDX is not strictly a surface analysis technique [135]. Nevertheless, EDX was used in this thesis to analyse the composition of TERS probes. Of special interest was the amount of metal content at the tip apex, which is an indication of the metal layer thickness. In addition, contamination such as metals from previous evaporation steps, carbon contamination from SEM imaging and hydrocarbons can be detected. In this thesis, a JEOL FE-SEM was used to perform EDX of TERS probes.

Chapter 5

Quantifying the Performance of Commercial TERS Probes

This chapter assesses the imaging performance of commercially available tip-enhanced Raman spectroscopy probes. A method is described for measuring the one-dimensional point spread function. The point spread function is used to calculate the optical contrast and spot diameter of three commercially available probes, which results in some conclusions on recommended use cases. Current methods of characterising tip-enhanced probe performance rely on numerical assumptions about the near-field and far-field beam areas. Other methods do not adequately discriminate between bundles and isolated nanotubes when using them as one-dimensional scattering objects. By using the AFM topography and Raman spectrum (with 785nm illumination to excite the radial breathing mode), single-walled carbon nanotubes suitable as 1D scattering objects are identified. Elemental analysis and boundary element simulations are employed to explain the formation of multiple peaks in the point spread functions as a consequence of random grain formation on the probe surface.

Publications Arising from this Chapter

- Reprinted with permission from L. R. McCourt, B. S. Routley, M. G. Ruppert, V. J. Keast, CI Sathish, R. Borah, R. V. Goreham, A. J. Fleming, "Single-walled carbon nanotubes as: One-dimensional scattering surfaces for measuring point spread functions and performance of tip-enhanced Raman spectroscopy probes," *ACS Applied Nanomaterials*, vol. 5, no. 7, pp. 9024–9033, 2022.

5.1 Introduction

TERS imaging resolution and optical contrast are dependent on the TERS probe. This thesis focuses on the fabrication of an improved TERS probe. Hence, an experimental method is required to accurately characterise TERS probe performance and allow comparisons between probes.

Finite element simulations can be used to estimate the enhancement factor of a TERS probe, and these values are often quoted by probe manufacturers [51,57,136]. However, approximations for probe and sample geometry are often required, reducing the validity of simulations as surface plasmons are sensitive to surface morphology including fine grain structure [55, 75]. Furthermore, Raman enhancement values from these simulations are often not indicative of laboratory performance.

The enhancement factor, F, is often used to characterise the Raman enhancement and is given by [137]:

$$F = \left(\frac{I_{\mathrm{nf}} - I_{\mathrm{ff}}}{I_{\mathrm{ff}}} - 1 \right) \frac{V_{\mathrm{ff}}}{V_{\mathrm{nf}}}, \tag{5.1.1}$$

where I_{nf} and I_{ff} are the near-field and far-field intensities, and V_{nf} and V_{ff} are the near-field and far-field volumes. The far-field intensity is collected with the tip retracted and the near-field with the tip on the sample. The far-field volume is often estimated as the diffraction-limited spot size of the illumination laser [36, 138–140] and the near-field volume by the tip apex diameter [138, 139]. There are several modifications of Equation 5.1.1 that account for factors such as the number of molecules in each scattering volume [141] or the tip acting as a mirror [140]. For a given enhancement factor, a larger near-field volume of the same intensity will result in a higher near-field signal. Alternatively, the contrast can be defined as $(I_{\mathrm{nf}}/I_{\mathrm{ff}})$, which more accurately quantifies the measured near-field to far-field signal ratio. The literature contains many values of the contrast, which has also been summarised [24].

For TERS imaging, rather than point spectroscopy, different methods can be used to characterise the TERS system. In an optical system, the point spread function (PSF) describes the response to a point light source. Images formed using a given system are the convolution of the PSF and the true image [142]. For TERS, the spot diameter of the PSF defines the spatial resolution, which depends on the volume of the near-field in the tip-sample junction [67]. The image contrast is determined by $I_{\mathrm{nf}}/I_{\mathrm{ff}}$ where the near-field signal is collected on a sample molecule and the far-field signal is collected on the substrate. The image contrast quantifies the systems ability to distinguish features on the sample. Hence, the PSF characterises the TERS imaging performance of a system.

To measure the PSF, a scattering object that approximates a delta function is required [142]. Single-walled carbon nanotubes (SWCNTs) act as one-dimensional scattering structures with diameters on the order of 1 nm and lengths that may exceed 1 μm [30,143]. This makes SWCNT superior for TERS characterisation compared to most nanoparticles that are typically on the order of tens of nanometres in diameter. Thus, SWCNTs are suitable structures for measuring the PSFs of TERS probes. Furthermore, the length of SWCNTs allows repeat measurements of the same structure from a single TERS image.

SWCNTs have three major spectral bands of interest, the radial breathing mode (RBM), D-band and G-band. The D-band and G-band occur at around 1350 and 1582 cm^{-1} respectively, and the D-band magnitude is associated with defects. The RBM wavenumber is dependent on tube diameter, a simple model is given by:

$$\omega_{\mathrm{RBM}} = \frac{A}{d_{\mathrm{t}}} + B \tag{5.1.2}$$

where A is typically around 248 cm^{-1} and B accounts for environmental factors such as the surrounding medium, nanotube bundling, molecular adsorption and surfactant, which all affect the wavenumber and intensity of the RBM [144]. Hence, an analysis of the RBM wavenumber distribution allows the distribution of diameters to be determined. This model is accurate for SWCNTs on the order of 1 nm, while for larger diameters, the RBM is hardly observable [145, 146].

SWCNTs are not ideal for measuring the PSF of a TERS system as the scattering cross-sections are dependent on the environment surrounding the nanotube and the polarisation. It has been shown that SWCNTs on a glass substrate only respond to light polarised parallel to the tube axis [69]. The absorption of light polarised parallel to the tube axis has been found to be 20 times greater than perpendicular polarised light due to the extreme anisotropic nature of SWCNTs [147]. In addition, the RBM signal increases as the chiral angle decreases [148]. However, the one-dimensional nature and availability of SWCNTs make them accessible scattering objects for measuring the PSF of TERS systems. Furthermore, the impact of environment and chirality on the measured results can be controlled by using a single sample for all probes that will be compared.

SWCNTs have been used previously to measure the resolution of TERS systems [149]. SWCNTs have also been used to fit Gaussian functions to the near and far-fields for bottom illumination TERS [140]. In doing so, the enhancement factor and optical spot size were determined. However, the height map range of 1 μm indicates that bundles of nanotubes were imaged. Similarly, nanotube bundles have been imaged and the bundle width was used to estimate the enhancement factor [150].

This chapter describes a method for measuring the PSF of TERS probes using SWCNTs. The RBM of SWCNTs is analysed to identify single nanotubes. High-resolution TERS cross-sections of the SWCNTs are collected and the PSF is calculated. From the PSF, the contrast and spot diameter are calculated, allowing a comparison of the imaging performance. This is repeated with 638 nm and 785 nm laser excitation to quantify probe performance at these two wavelengths, which are commonly used for TERS imaging of different materials. The method is used to characterise the TERS imaging performance of four commercially available TERS probes.

5.2 Method

5.2.1 Sample preparation

Polished silicon substrates were coated with a 50 nm thick gold layer using thermal evaporation. (6,5) chirality SWCNTs were purchased (Signis SG65i) with a reported average diameter of 0.78 nm as measured using near-infrared fluorescence spectroscopy. The nanotubes were dispersed in N-Methyl-2-pyrrolidone with an initial mass loading of 1 mg/mL. The mixture was bath sonicated for 15 minutes. The initial mass loading was found to be too high as a sediment was formed. The mixture was diluted ten-fold and bath sonicated for 15 minutes. The translucent decantate of this mixture was further diluted five-fold and sonicated for 15 minutes. The solution was drop cast onto the gold substrate, which was held horizontal using reverse action forceps and was left to dry for several days.

5.2.2 TERS

Figure 5.1(a) shows a schematic of the TERS microscope used for this work. The Horiba XploRA Plus confocal Raman microscope provides the spectrometer and filters to process the Raman scattered light collected from the sample. The XploRA unit also provided the 785 nm laser excitation. The system was modified to include a 638 nm fibre coupled laser. The microscope operates with side illumination, where the laser is focused onto the tip apex using a 100x, 0.7 numerical aperture side objective lens. A laser power of 0.7 mW measured at the probe results in a power density of approximately 4.3 x 10^5 W/cm^2 for the 638 nm laser and 2.8 x 10^5 W/cm^2 for the 785 nm laser. Both laser sources were aligned with a vertical polarisation. The laser alignment procedure is detailed in Figure 5.3. A 600 g/mm grating resulted in a spectral resolution of 3.1 cm^{-1}.

An AIST-NT atomic force microscope was used to control the tip scanning. The scanning protocol used was a hybrid mode where the Raman signal is collected in contact mode for the specified acquisition time. The height map and movement between pixels are performed in tapping mode. The Raman acquisition time was minimised while achieving an acceptable Raman signal-to-noise and was generally 0.1-0.5 s. This reduced the duration of mapping and avoided unnecessary optical drift. An example G-band TERS map of a SWCNT is shown in Figure 5.1(c).

AFM maps were acquired using tapping mode to minimise sample and probe damage. These AFM maps are used to identify suitable carbon nanotubes that appear as isolated tubes, free from any bundles and are roughly aligned with the x-axis. An example of a suitable SWCNT is shown in Figure 5.2(a). Once a suitable SWCNT is found, the tip is put into contact with the nanotube and the laser alignment is adjusted to optimise the Raman signal. The Raman signal is checked for the presence of a single radial breathing mode peak at approximately 280 cm^{-1}. A narrow line width supports the conclusion that this is an isolated SWCNT. If this peak is not present, appears to be broadened or there are multiple peaks then the CNT is deemed unsuitable and another is found. If a Raman spectrum typical of a SWCNT can't be produced, the TERS

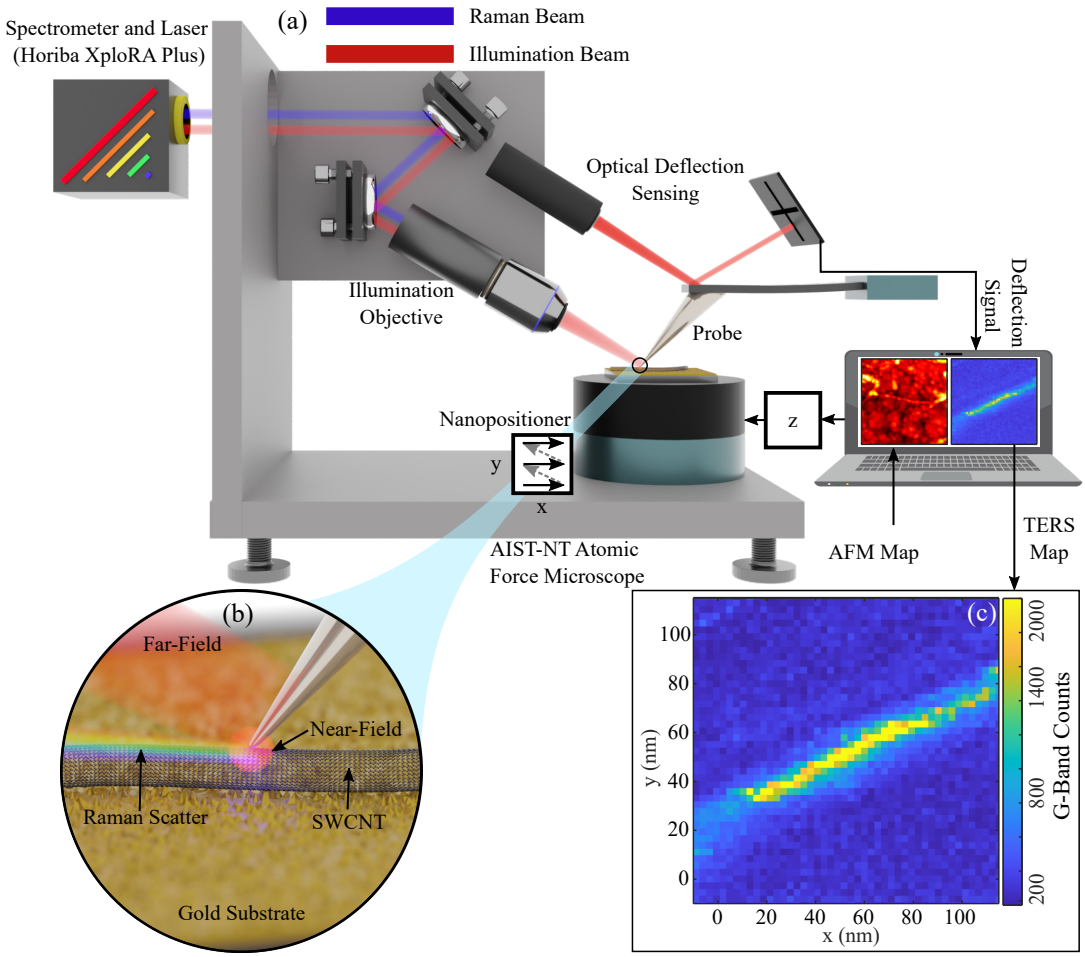

Figure 5.1: (a) Schematic of the experimental setup used for tip-enhanced Raman spectroscopy (TERS). The side illumination setup requires TERS probes with the access tip geometry as shown. The inset (b) shows an illustration of a TERS probe scanning over a SWCNT on a gold substrate. The far-field light excites surface plasmons on the tip surface that produce an enhanced near-field. The near-field amplifies the Raman scattering in the localised area. The TERS map (c) shows the G-band counts of a single-walled carbon nanotube (SWCNT).

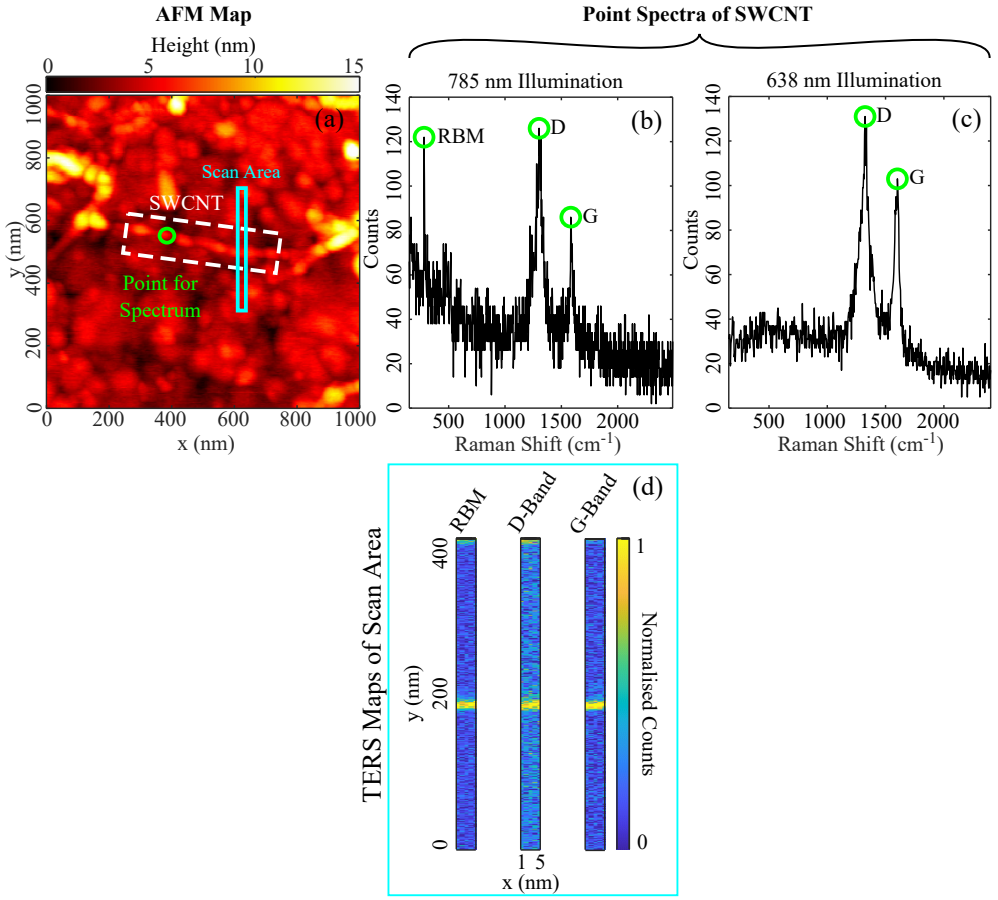

Figure 5.2: (a) An AFM map of a SWCNT that is suitable for collecting TERS cross-sections. The nanotube (surrounded by the white box) is approximately aligned horizontally. The spectrum of the SWCNT is collected to ensure the radial breathing mode (RBM) is present when illuminated with the 785 nm laser. The scan area (shown by the cyan box) is 400 x 5 nm with a pixel size of 1 nm^2. (b-c) Example TERS spectra of a SWCNT for 785 nm and 638 nm illumination. The RBM peak at 282.2 cm^{-1} gives a SWCNT diameter of 0.86 nm. (d) Example TERS cross-sections plotted for the RBM, D-band and G-band. These cross-sections are used to calculate the PSF, contrast and spot diameter of TERS probes.

probe is deemed to have failed. Example SWCNT spectra for 785 nm and 638 nm excitation are shown in Figure 5.2(b-c) where the RBM mode occurs at 288 cm^{-1}, the D-band at 1289 cm^{-1}, and the G-band at 1587 cm^{-1} and 1580 cm^{-1} for 638 nm and 785 nm excitation respectively. The RBM is only excited with the 785 nm excitation.

For a suitable SWCNT, a TERS map is acquired with an area of 5 nm x 400 nm with the long axis aligned perpendicular to the SWCNT and a pixel count of 5 x 400. The map contains 5 cross-sections of the SWCNT. Examples of RBM, D-band and G-band TERS maps are shown in Figure 5.2(d) with the SWCNT occurring at approximately $y = 200$. The optical alignment and scanning methodology are summarised in Figure 5.3.

For a given wavenumber ω, let the Raman map be denoted as:

$$M_\omega = \begin{bmatrix} m_{1,1} & \dots & m_{1,400} \\ \vdots & \ddots & \vdots \\ m_{5,1} & \dots & m_{5,400} \end{bmatrix}, \tag{5.2.1}$$

where $m_{i,j}$ are the Raman counts at each pixel and each row has been aligned so that the SWCNT is positioned approximately at index 200. Assuming the PSF is symmetric in the x and y-axis:

$$\mathrm{PSF}_{\omega,j} = \frac{\sum_{i=1}^{5} m_{i,j}}{\max(\sum_{i=1}^{5} m_{i,j})}. \tag{5.2.2}$$

The far-field contribution is estimated by taking the mean of the PSF with the near-field peak removed:

$$\overline{\mathrm{PSF}}_{\mathrm{ff}} = \frac{\sum_{j=1}^{l} \mathrm{PSF}_{\omega,j} + \sum_{j=r}^{end} \mathrm{PSF}_{\omega,j}}{n}, \tag{5.2.3}$$

where l and r are the j indices at two full maximums to the left and right of the PSF peak respectively, and n is the number of elements in the numerator.

The near-field PSF is then:

$$\mathrm{PSF}_{\mathrm{nf}} = \mathrm{PSF} - \overline{\mathrm{PSF}}_{\mathrm{ff}}. \tag{5.2.4}$$

The contrast is calculated as:

$$C_\omega = \frac{1 - \overline{\mathrm{PSF}}_{\mathrm{ff}}}{\overline{\mathrm{PSF}}_{\mathrm{ff}}}, \tag{5.2.5}$$

which quantifies the ratio of near-field to far-field contributions. Hence, a high contrast will allow objects of interest to be distinguished from the substrate. The starting wavenumbers were 285 cm^{-1} for the RBM, 1292 cm^{-1} for the D-band and 1606 cm^{-1} for the G-band. The wavenumbers were adjusted to maximise the contrast for each band. The mean contrast is calculated across the spectral bands to reduce the effects of band ratio variation between nanotubes. For 638 nm excitation, the RBM is not included in the calculation as it is not effectively excited at this wavelength. The mean contrasts are:

$$\overline{C}_{785} = \frac{C_{\mathrm{RBM}} + C_{\mathrm{D}} + C_{\mathrm{G}}}{3} \tag{5.2.6}$$

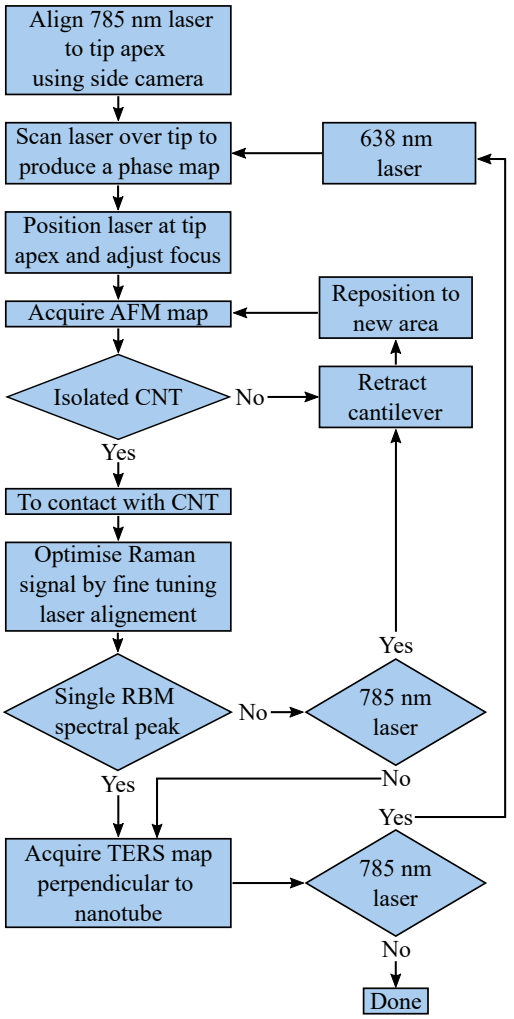

Figure 5.3: Flowchart describing the procedure used to align optics, identify suitable SWCNTs and perform TERS scans.

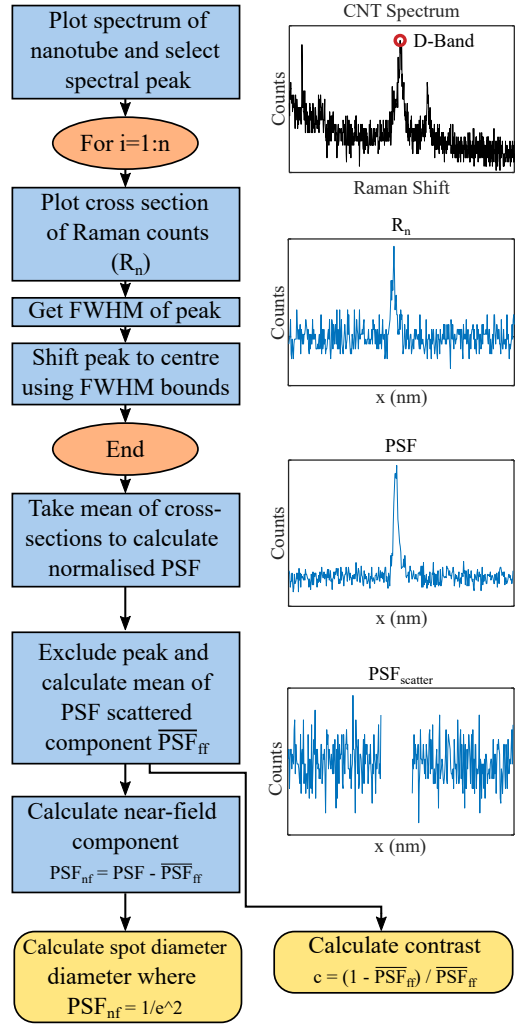

Figure 5.4: Flowchart describing the data processing used to calculate the PSF, spot diameter and optical contrast.

and

$$\overline{C}_{638} = \frac{C_{\mathrm{D}} + C_{\mathrm{G}}}{2}. \tag{5.2.7}$$

From Equation 5.2.4, the spot diameter d is the diameter where $\mathrm{PSF}_{\mathrm{nf}}$ falls to $1/e^2$ of the maximum value. This procedure was repeated using 785 nm and 638 nm lasers. The data processing method is summarised in the flowchart provided Figure 5.4. In this work, contrast and spot diameter are the metrics that characterise the imaging of a TERS system.

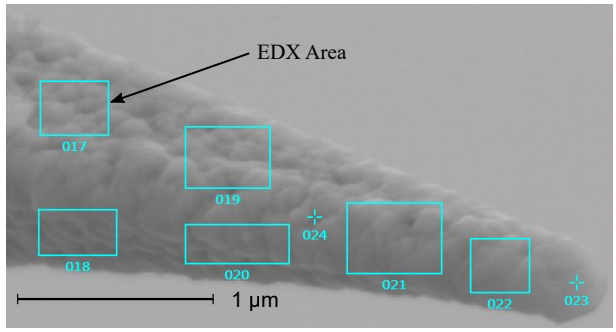

Figure 5.5: SEM image of a probe showing the EDX area of analysis.

5.2.3 TERS Probes

Four commercially available probes were selected to demonstrate the method presented in this chapter:

- A - silver and gold coated silicon (Omni-TERS-SNC Ag)
- B - gold coated silicon (Omni-TERS-SNC Ag)
- C - gold coated silicon (AppNano ACCESS-FM Au)
- D - silver coated silicon (NaugaNeedles TERS Ag)

Silver tarnishes rapidly in ambient conditions, which results in a redshift in plasmon energy and a decreased scattering cross-section [20, 77, 78, 151]. Hence, the silver probes were kept in the sealed packages they were delivered in and were opened immediately before use. This minimised the possibility of silver degradation. The Au probes were stored in gel packs in ambient conditions.

5.2.4 SEM and EDX

A JEOL FE-SEM was used for SEM imaging and EDX element analysis. EDX was performed where the probe was thick enough to limit effects associated with a finite electron penetration depth and allow a comparison between the probes. The SEM and EDX were performed immediately after opening the sealed packages. These probes were not used for TERS as enhancement was found to degrade after SEM/EDX, likely due to carbon contamination. An example SEM image is shown in Figure 5.5 with the EDX area indicated.

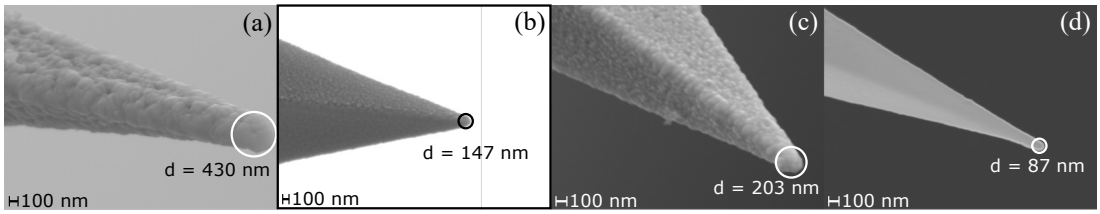

Figure 5.6: SEM images of the TERS probes reviewed in this chapter: (a) probe A, (b) probe B, (c) probe C and (d) probe D. The approximate apex diameters are displayed on each image.

5.2.5 Simulations

Boundary element method simulations were performed to investigate the role of random grain formation on the PSF of TERS probes. These simulations were performed using the MNPBEM MATLAB package [91]. 638 nm plane wave excitation was incident on silver nanocones with an apex diameter of 40 nm. To simulate different grain formations at the tip apex of TERS probes, several configurations of silver nanospheres with 30 nm diameters were embedded into the nanocones. Electric field maps were calculated and analysed.

5.3 Results

This section details the experimental results acquired using the TERS probes shown in Figure 5.6. The TERS cross-sections, calculated PSFs and performance metrics are given. The probes are also analysed using scanning electron microscope (SEM) images and energy-dispersive X-ray spectroscopy (EDX) elemental analysis. Finally, simulations are presented to explain the effects of random grain formation at the probe apex. Probes A, B and C exhibited Raman enhancement. Probe D exhibited no Raman enhancement with the method presented in this chapter and as a result, probe D is not included in several figures.

5.3.1 SEM Images and EDX Element Analysis

SEM images of the TERS probes tested are shown in Figure 5.6. The apex radius was estimated using the SEM images with the assumption that the tip apex is a nanosphere. The element compositions of the probes as measured using (EDX) are given in Table 5.1. Probe A has the largest apex diameter at 430 nm. This corresponds to the highest metal composition by mass percentage at 90%, consisting of 73% silver and 7% gold. Probes B, C and D have smaller apex diameters at 147 nm, 203 nm and 87 nm respectively. Probes A, B and C have visible metal grain structures on their surfaces and have metal contents exceeding 70%. Probe D has a much lower metal content at 22% and no metal grain structure is visible in the SEM image. It is thought that the low metal content results in a low likelihood that a metal grain will form at the tip apex. This explains why no examples of probe D exhibited measurable Raman enhancement using 638 nm or 785 nm excitation with our experimental setup.

Table 5.1: Mass composition of TERS probes measured using EDX.

Probe	Silicon (Mass %)	Silver (Mass %)	Gold (Mass %)
A	12	73	7
B	3	0	86
C	19	0	72
D	52	22	0

Table 5.2: Wavenumbers that maximised the contrast for each spectral band and probe.

Probe	Wavelength (nm)	RBM (cm^{-1})	D-Band (cm^{-1})	G-Band (cm^{-1})
A	638	N/A	1325	1602
	785	282	1302	1585
B-1	638	N/A	1289	1587
B-2	785	288	1289	1580
C-1	638	N/A	1313	1594
C-2	785	285	1284	1587

5.3.2 Imaging Performance.

The wavenumbers that maximised the contrast for each probe are given in Table 5.2. Using probe A, the data for 638 nm and 785 nm excitation was successfully collected with a single probe. For probes B and C, two probes each were required as probe degradation occurred while searching for suitable SWCNTs after switching from 785 nm to 638 nm excitation. Four examples of probe D were tested with none producing an observable Raman enhancement using the presented method.

Figure 5.7 shows the PSFs for the RBM, D-band and G-band for probes A, B and C with 638 nm and 785 nm illumination. The contrast for each band, the calculated spot diameters and the apex diameter estimated from the SEM data are summarised in Table 5.3. Of the probes tested, probe A provides the highest contrast with 638 nm and 785 nm excitation, which require shorter acquisition times than the other probes tested. However, the spot diameter is also the largest at 57 nm and 52 nm for 638 nm and 785 nm excitation respectively. This makes probe A suitable for high-speed, lower resolution TERS imaging. However, the PSFs reveal multiple

Table 5.3: Performance characteristics of TERS probes for imaging SWCNTs at 638 nm and 785 nm laser excitations. The apex diameter was estimated using the SEM data with separate probes.

Probe	Wavelength (nm)	Contrast RBM	Contrast D	Contrast G	Contrast Mean	Spot Diameter (nm)	Apex Diameter (nm)
A	638	N/A	13.59	9.82	11.21	57	430
	785	24.61	44.11	21.13	30.62	52	
B-1	638	N/A	1.13	1.39	1.26	45	147
B-2	785	13.73	3.62	7.23	8.19	16	
C-1	638	1.14	9.48	7.68	8.58	28	203
C-2	785	2.04	3.80	3.65	3.17	20	

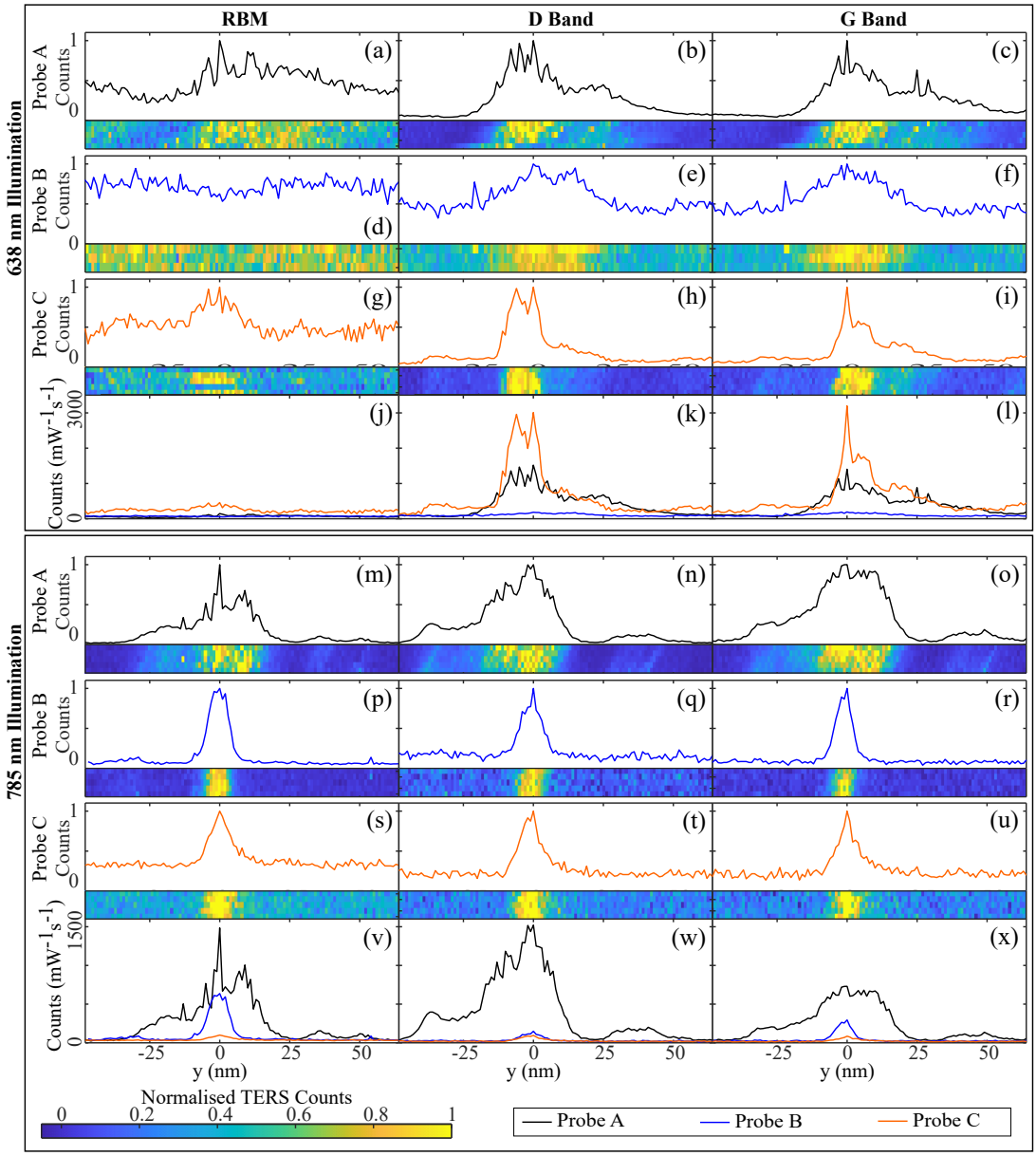

Figure 5.7: Data acquired from high-resolution cross-section TERS maps of SWCNTs. PSFs with the corresponding normalised TERS map shown below for (a-i) 638 nm and (m-u) 785 nm illumination. Results are included for three TERS probes at the RBM, D-band and G-band. SWCNT cross-sections with TERS counts per mW of laser power per second of pixel acquisition time for (j-l) 638 nm and (v-x) 785 nm illumination. The PSFs are used to calculate the contrast and spot diameter of each TERS probe, which are summarised in Table 5.3.

hot spots, which introduce artefacts into TERS maps. This appears as a ghosting effect in the TERS maps to the right of the SWCNT in Figure 5.7(a-c) and the left in Figure 5.7 (m-o).

Probe B-1 provides poor contrast with 638 nm excitation. Hence, long acquisition times are required for an acceptable signal-to-noise ratio. Furthermore, the spot diameter of 45 nm and

multiple hot spots make the probe unsuitable for high-resolution imaging. Conversely, probe B-2 provides adequate contrast at 785 nm excitation, the narrowest spot diameter at 16 nm and a single hot spot, which make the probe suitable for high-speed, high-resolution imaging.

Probe C-1 provides adequate contrast at 638 nm excitation and a spot diameter of 28 nm making it the most suitable for high-speed, high-resolution imaging. However, the PSF of probe C-1 shows multiple hot spots, which will result in ghosting artefacts that are visible in the TERS maps shown in Figure 5.7(h-i). Probe C-2 provides a lower contrast at 785 nm excitation compared to probe B-2 and thus, is less suitable for high-speed imaging. To compensate for the lower contrast, longer acquisition times will be necessary. However, long acquisition times introduce significant optical drift and expose the probe to an extended period of illumination that may degrade the metal layer. On the other hand, the spot diameter is relatively small and the PSFs show one hotspot making probe C-2 suitable for low-speed high-resolution imaging.

The measured spot diameters are significantly smaller than the apex diameters. For example, probe A has a measured spot diameter of 57 nm when excited with the 638 nm laser, while the apex diameter is approximately 430 nm. Thus, for this example, the spot diameter is only 13% of the apex diameter, which is much smaller than previously reported [152]. This shows that approximating the tip apex as a sphere for a grainy probe is inadequate for estimating the spatial resolution. The complex geometry at the tip apex must be considered along with tip-sample interactions that increase confinement [64–66]. As an example, Figure 5.6(c) shows sharp features at the tip apex that are smaller than the apex diameter if the tip is considered as a sphere. It is possible that higher resolution SEM images would reveal further features at the tip apex.

Random grain formation can partially explain the differences in PSFs between probes B-1 and B-2, likewise C-1 and C-2. The grain formation at the tip apex will determine the spot diameter and this will vary from probe to probe [76]. However, probe A also displays different PSFs when illuminated with 638 nm and 785 nm excitation despite being the same probe. One explanation is that different plasmon modes are being excited that have unique enhancement distributions. This effect has been demonstrated on gold nanoparticles in the literature [102, 153]. Another potential explanation is that the tip morphology was altered due to excessive heat generation, although anecdotally this is usually associated with a significant decrease in enhancement and therefore unlikely.

There are notable differences between the PSFs of the spectral bands for probe C when illuminated with the 638 nm laser. The D-band PSF displays two distinct peaks while the G-band PSF displays a less pronounced second peak as shown in Figure 5.7(h) and (i) respectively. This is undesirable as it indicates that the choice of spectral band effects the measured PSF. This effect is not present for the other measurements presented. It is possible that a bundle of nanotubes were imaged with individual nanotubes of varying D-band and G-band scattering cross-sections.

The presented method allows the PSF to be measured when: $d_{\mathrm{SWCNT}} << d_{\mathrm{spot}}$, where d_{SWCNT} is the SWCNT diameter and d_{spot} is the PSF spot diameter [142]. This inequality is true for the conditions described in this article. However, the method is likely to be unsuitable for measuring the PSF of TERS systems that exhibit sub-nanometre resolution where $d_{\mathrm{SWCNT}} \approx$

d_{spot}, such as those under vacuum [64, 154]. Furthermore, as SWCNTs are only excited by in-plane polarisation, the measured contrast will depend on the tip-sample geometry [69]. Thus, the method presented here is suitable for comparing the performance of TERS probes in a specific microscope, but likely not between different microscopes.

The plasmon response of grainy metal probes is highly dependent on random grain formation at the tip apex [76, 155, 156]. Hence, a statistical analysis of several probes is required for a comprehensive analysis of design parameters.

The relative intensities of the D-band and G-band have been shown to vary along the length of a SWCNT [149]. The method presented in this chapter accounts for this by averaging five cross-sections over a length of 5 nm. The method could be improved by averaging over more lines and a larger length. Furthermore, the method presented assumes a PSF that is symmetrical in the x-y planes. The 2D PSF could be calculated by devolving the PSF acquired with SWCNTs aligned with the x-axis and y-axis.

The proposed method of comparing probe imaging performance has been demonstrated on probes A, B and C, which reveals the PSF, contrast and spot diameter. The PSFs provide information about potential imaging artefacts due to multiple hot spots. The TERS imaging performance is characterised by acquiring a single TERS map, which does not require assumptions about particle density, apex diameter, or spot diameter. Therefore, this chapter describes an improved method for characterising the imaging performance of a TERS probe compared to other methods in the literature that estimate the far-field [36, 138–140] or near-field [138, 139] spot sizes, and calculate the enhancement using tip-in-contact and tip-retracted spectra, or require the number of molecules in the scattering volume to be estimated [140]. The disadvantages of the method presented are that the measured contrast may be polarisation dependent and that the spot diameter should be larger than the nanotube diameter.

A potential alternative method has been presented theoretically in the literature that uses the TERS approach curve on an ideal two-dimensional scattering surface. The tip radius is also measured using a topographic alignment grid [157]. This approach may provide characterisation of TERS systems with reduced sample dependence but has not been confirmed experimentally.

5.3.3 Effects of Random Grain Formation.

Figure 5.8(a-d) shows the normalised electric field enhancement at the apex of simulated TERS probes with a 40 nm diameter tip apex and random grain formation. The probes are illuminated with a 638 nm planewave polarised in the $\hat{y}$ axis. Figure 5.8(e) shows the normalised electric field cross-section perpendicular to the apex corresponding to the geometries (a-d).

Figure 5.8(a) shows a probe where no random grains have formed in the local vicinity of the tip apex. The corresponding cross-section reveals that this configuration results in a wide spot diameter, which would lead to poor optical resolution when used for TERS imaging.

Figure 5.8(b) shows a probe where a single grain has formed at the tip apex, acting as a new geometric apex. The corresponding cross-section shows that this configuration results in the narrowest spot diameter and would be suitable for high-resolution TERS imaging.

Figure 5.8(c) shows a probe where a single grain has formed but is offset from the apex. The

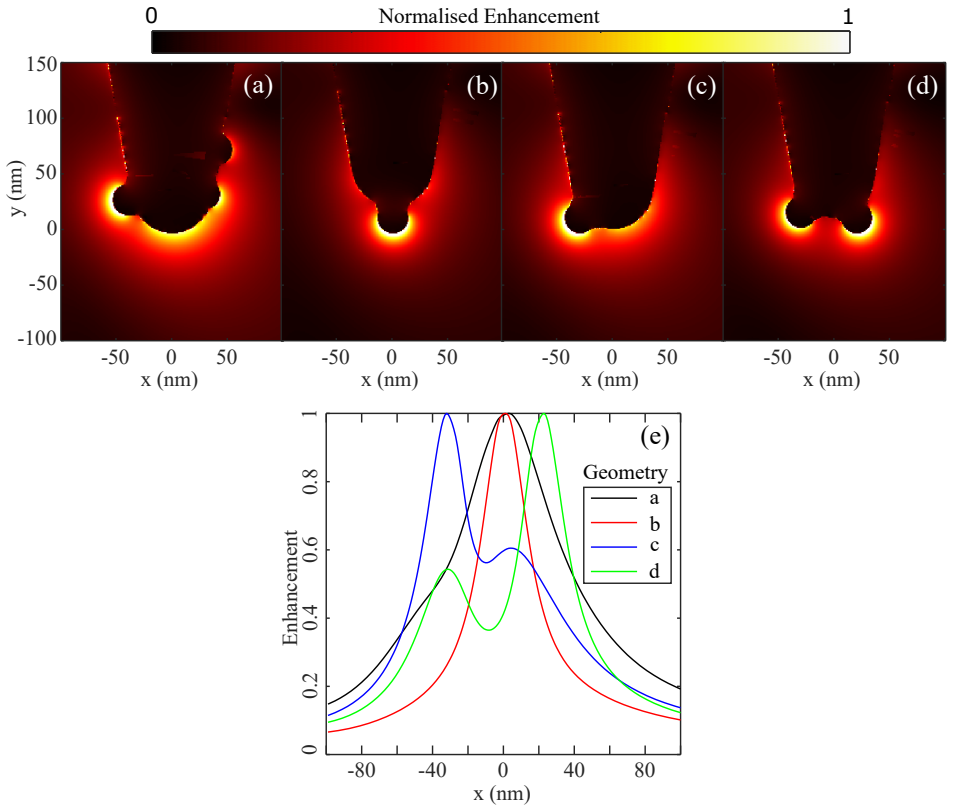

Figure 5.8: (a-d) Normalised enhancement maps of grainy silver probes acquired using boundary element method simulations. These geometries are used to investigate the effects of random grain formation on the spot diameter and the introduction of multiple peaks in the PSF. (e) Normalised enhancement cross-sections below the grainy silvers TERS probes shown in (a-d). Probes with multiple grains offset from the tip apex result in an increased spot diameter and multiple enhancement peaks that introduce artefacts into TERS maps.

corresponding cross-section reveals that this configuration results in an increased spot diameter. In addition, multiple enhancement peaks would introduce artefacts into TERS maps. These effects are amplified when multiple grains are offset from the apex as shown in Figure 5.8(d) and the corresponding cross-section.

These results indicate that random grain formation has a profound effect on the performance of TERS probes in terms of spot diameter and the introduction of artefacts in TERS maps due to multiple enhancement sites. Random grain formation provides an explanation for the different PSFs and spot diameters measured for the Omni-TERS Au probes (see Table 5.3). The probe used with 638 nm illumination likely had multiple grains in proximity to the apex resulting in a spot diameter of 45 nm and multiple PSF peaks. Meanwhile, the probe used with 785 nm illumination likely had fewer or even a single grain at the apex resulting in a spot diameter of 16 nm and a single PSF peak.

One method of overcoming the random grain formation at the apex of TERS probes involves using a single nanoparticle as the plasmonic nano-antenna. Such probes can have a nanoparticle with dimensions optimised using optical simulations [103]. Using focused ion beam milling or deposition allows these nanoparticles to be created on AFM cantilevers for TERS imaging [108, 158]. The methods of measuring probe performance outlined in this work will allow a comparison between single nanoparticle TERS probes and the existing grainy metal layer TERS probes investigated here.

5.4 Conclusion

This chapter describes a new method for measuring the PSF, contrast, and spot diameter of TERS probes in the side-illumination configuration. Knowledge of the contrast and spot diameter allow probe characteristics to be matched to a given imaging application. For example, probes that provide low contrast and a small spot diameter are suitable for high-resolution imaging of small structures where the acquisition time can be increased without introducing significant optical drift. On the other hand, a probe that provides high contrast is suitable for large TERS maps where the acquisition time must be kept low to reduce optical drift. The method presented is unique, as using 785 nm excitation of the RBM allows for selection of isolated SWCNTs that act as one-dimensional Raman scattering probes. This ensures accurate measurements of the near-field optical beam-width for TERS probes. Different lasers can then be used to determine performance over a range of illumination wavelengths. This method is used in Chapter 6 to compare the performance of a gold nanocone probe with the commercial ones tested in this chapter.

Chapter 6

Nanocone Probe Fabrication and Performance

This chapter describes the fabrication and characterisation of gold nanocone TERS probes designed in Chapter 3. The performance of a fabricated probe is found to exceed that of the commercially available TERS probes considered in this thesis. The nanocone probe exhibited superior optical resolution, chemical stability and collocation of TERS and height maps while providing comparable contrast.

Publications Arising from this Chapter:

- L. R. McCourt, B. S. Routley, M. G. Ruppert, A. J. Fleming, "Gold Nanocones for Collocated Tip-Enhanced Raman Spectroscopy and Atomic Force Microscope Imaging," *Journal of Raman Spectroscopy*, Submitted.

Acknowledgements:

- The author would like to acknowledge the Research and Prototype Foundry, The University of Sydney, which performed the FIB milling and electron beam evaporation in this chapter.

6.1 Introduction

As discussed in Chapter 1.5 and shown experimentally in Chapter 5, commercially available TERS probes have several disadvantages that are consequences of using a grainy metal layer. These disadvantages include:

1. An offset between AFM and TERS maps.
2. Artefacts in TERS maps due to multiple hot spots.
3. Unreliable Raman enhancement with some tip producing no measurable enhancement.

(a) Nanocone probe (b) Nanocap probe

Figure 6.1: Two possible geometries for gold TERS probes based on the cone shape are shown. (a) The nanocone geometry consists of a solid gold nanocone attached to a plateaued silicon AFM tip with a thin adhesive layer (chromium or titanium). (b) The nanocap geometry consists of a gold layer on a silicon AFM tip with a ring of gold removed to electrically isolate the gold cap at the apex.

4. Decreased AFM and TERS resolutions if a thick metal layer is used to ensure reliable enhancement.

5. Short lifetimes for silver probes due to rapid degradation in ambient conditions.

Chapter 2 identified gold nanocones as suitable single-particle TERS probes. Smooth nanocones remove the issues associated with random grain formation observed with commercially available TERS probes. Furthermore, the resonance wavelength can be tuned with nanocone length without affecting the optical or topographical resolutions.

In Chapter 3, numerical models were found that allow optimised gold nanocone TERS probes to be designed for a chosen excitation wavelength. These models assume a smooth and solid metal nanocone particle with a finite length. Optical simulations revealed that a gold-coated nanocone with a thickness of 35 nm performs equivalent to a solid gold nanocone. Figure 6.1 illustrates two possible geometries for gold nanocone TERS probes. The solid nanocone geometry is shown in (a) and consists of a solid gold nanocone attached to a plateau on an AFM tip. The nanocap geometry consists of a gold-coated AFM tip with a ring of exposed silicon that optically isolates the apex at optical frequencies.

This Chapter discusses the fabrication of optimised nanocone TERS probes and compares their performance to commercially available probes using the method presented in Chapter 5.

6.1.1 Nanocones Probes in the Literature

The use of nanocone arrays in SERS is well documented in the literature. The transverse mode of a gold nanocone array has been used to enhance in-plane excitation [159]. Likewise, silicon or silver double nanocone substrates have been shown to improve Raman sensitivity [160, 161]. Arrays of gold nanocones have also been fabricated and the plasmon resonance wavelength has been demonstrated to be tuneable from 600-700 nm [162].

The fabrication of gold nanocone near-field probes is described in [108]. The authors successfully produced gold nanocone probes with lengths ranging from 15-175 nm. The probes were fabricated by FIB milling a plateau on an AFM tip before coating with a stack consisting of a chromium adhesion layer and a ticker gold layer using thermal evaporation. An SiO_x etch mask was deposited on the stack with a 50 nm base diameter and a height of 100-300 nm using focused electron beam induced deposition. Milling with an argon ion beam resulted in nanocones with a base angle of 60-70^o being formed. The plasmon resonance wavelength was measured using dark-field scattering. Increasing the nanocone length tuned the resonance wavelength from 500-675 nm. However, it is likely that longer resonance wavelengths could be achieved with loner nanocones. A proof of concept was achieved by showing Raman enhancement of a dilute CNT sample. The probes were also demonstrated to provide high-resolution topographical measurements as AFM probes. However, the probes were not used for TERS imaging and their performance was not measured or compared to commercially available probes.

The same group has also demonstrated the fabrication of gold nanocones without the deposition of an SiO_x etch mask [163]. Instead, a titanium, gold and Al_2OA_3 stack was deposited. A ring-shaped ion beam milling profile was then used to create a pillar. Subsequent milling utilised the Al_2OAu_3 layer at the top of the stack as an etch mask. The resulting probes were not tested for TERS or AFM performance.

To the author's knowledge, there have been no reports of high-resolution TERS mapping with gold nanocone probes in the literature. Furthermore, these probes have not been compared to commercially available probes or fabricated probes consisting of a grainy metal surface.

6.1.2 Manufacturing Methods

The following sections discuss possible techniques for fabricating optimised gold nanocone TERS probes. The advantages and disadvantages are discussed and the availability of suitable equipment is discussed.

Electrochemical Etching

For electrochemical etching, a metal wire is dipped into an etch solution with a counter electrode. A DC voltage causes the wire to be dissolved, leaving a sharp tip apex. This allows silver and gold tips to be fabricated with diameters of 50-100 nm [22]. However, this method results in large morphology and enhancement variations from tip to tip [164]. Researchers have estimated only a few out of 20 tips manufactured will give adequate near-field enhancement resulting in poor TERS signal-to-noise ratios [106]. Furthermore, if grain structures are formed then tip convolution with the sample is difficult to estimate [106].

Based on the literature, electrochemical etching is not a fabrication method that solves the current issues with commercially available TERS tips. Thus, this method was not considered.

Vacuum Deposition

Vacuum deposition is performed by thermally evaporating a metal source in a vacuum, allowing metal molecules to reach the sample. Using this method, several tips can be coated with silver, gold or another metal simultaneously. This results in a grainy structure and there is a chance that a single nanoparticle is deposited at the apex of the AFM tip. However, this method is unreliable with large variations in morphology and enhancement [164]. In addition, the random nature of the particle at the tip apex leads to variation in spatial resolution and the direction of dipole polarisation. This induces inconsistent imaging from tip to tip [165]. Furthermore, the tips exhibit poor mechanical stability with wear and peeling during scanning. The morphology can somewhat be controlled through deposition rate with high deposition rates resulting in smoother surfaces [166].

Although vacuum deposition commonly results in a grainy surface, a thick metal layer can be deposited and subsequently shaped using a sputtering method. This yields a relatively pure nanoparticle and is used in this work to deposit a gold layer.

Electroless Deposition

Electroless deposition is performed by exposing an AFM tip to a cleaning agent such as hydrofluoric acid vapour to remove oxide layers. The tip is then immersed in a silver or gold solution allowing particles to grow. This process results in unpredictable and non-uniform coverage [167] [21]. Furthermore, the use of HF is problematic due to its acute toxicity if inhaled, ingested or comes into contact with skin.

Due to the poor control over particle geometry, electroless deposition was not considered.

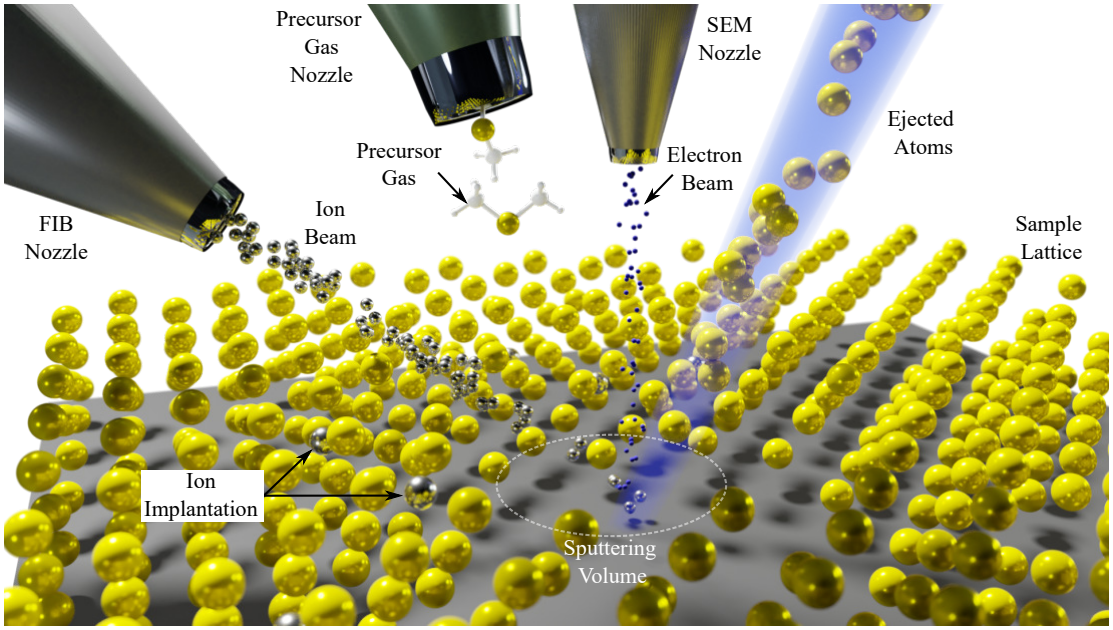

Figure 6.2: Illustration of a crossbeam FIB-SEM experimental setup with a precursor gas capable of FIB or SEM induced deposition. For FIB milling, high energy ions enter the sample, sputtering surface molecules. Ions are also implanted into the sample to a depth of approximately 20 nm. The system illustrated can also be used for FIB induced deposition where the ion beam is used to decompose precursor gas molecules that have adsorbed to the surface. The electron beam in a crossbeam system can be used to image the sample simultaneously to FIB operation. Alternatively, the electron beam may be used to perform electron beam induced deposition.

Focused Ion Beam Milling

Focused ion beam (FIB) milling is most commonly performed by accelerating metal ions, such as gallium, at a target. A liquid metal ion source is positioned in contact with a sharp tungsten needle with a high voltage extraction field. The liquid metal is pulled onto the tip, ionised and accelerated towards the target with a voltage between 5-50 keV. The metal ions enter the sample and sputter surface material while also implanting the metal ions [168]. Other effects include displacement of sample atoms, sample heating, secondary electrons forming in the sample and the breaking of chemical bonds [169]. FIB milling is performed using an FIB-SEM cross-beam setup as illustrated in Figure 6.2. Sputtering sample atoms allows FIB milling of small features on the sample. Milling resolutions of 5 nm have been demonstrated. FIB milling can be operated in a cross-beam configuration with a scanning electron microscope as illustrated in Figure 6.2. This allows real-time monitoring of the FIB milling process during device fabrication.

FIB milling is well suited to machining bulk metal layers into nanoparticles [170]. These nanoparticles can be produced at the apex of an AFM tip and serve as the TERS probe. Consistent surface morphology can be achieved and the dimensions can be tuned by varying sputter rate and the dimensions of the etch mask if one is used.

FIB milling has been used to successfully produce nanocone probes for near-field scanning

optical microscopy [108]. This example used an SiO_x etch mask that was deposited using electron beam induced deposition. The etch mask reduces the etch rate over the given area, allowing a nanocone to form with an angle dictated by angle dependant sputtering. The length of the final nanocone was controlled by varying the etch mask thickness. Furthermore, these nanocones were produced with apex radii of approximately 10 nm, providing superior optical and mechanical resolution to commercially available silver coated tips. Thus FIB milling is well suited to fabricating the nanocone geometry illustrated in Figure 6.1(a). FIB milling has also been used to mill a ring on a pyramid AFM probe to create a nanopyramid notch [171]. This method achieved results similar to the nanocap illustrated in Figure 6.1(b).

Focused Beam Induced Deposition

Focused electron beam induced deposition (FEBID) of material is possible by using a precursor gas. The precursor gas contains the desired material to be deposited and a volatile component. Secondary electrons from the sample surface decompose the precursor gas allowing the target material to adsorb to the surface. FEBID is illustrated in Figure 6.2 with SEM nozzle and precursor gas system. Similarly, focused ion beam induced deposition FIBID allows metals to be deposited. Direct deposition of materials using FIBID and FEBID have both been demonstrated with resolutions as low as 3 nm. However, FIBID has been reported to deposit higher metal contents [172, 173].

FEBID would allow for direct deposition of metallic nanoparticles at the apex of an AFM tip for use in TERS. However, the resulting nanoparticles are typically heavily contaminated. Carbon from the ion source can comprise up to 28% of the sample [174]. Furthermore, organometallic precursors result in low metal content nanoparticles with carbon embedding causing the metal to separate into small clusters [175]. The overall purity of metals deposited using FEBID is low, which is not ideal for producing TERS probes as it is unlikely that a strong plasmon response will be produced. This contamination can be removed by exposing the structure to a scanning electron beam operated in a 10 Pa H_2O environmental chamber [176]. Direct focused ion beam deposition in combination with contamination removal presents a valid method for producing nanocone TERS probes. However, a suitable fabrication facility could not be found in Australia.

Summary

A suitable fabrication facility could not be found to perform FIBID and decontamination. Thus, FIBID was not used to produce TERS probes. Instead, FIB milling was used to etch nanoparticles from solid metal layers. This avoids the contamination from the precursor gas and metal layers were deposited using e-beam or vacuum deposition.

6.2 Probe Design

The empirical model for gold nanocone resonance wavelength developed in Chapter 3.3.1 was used to design an optimal TERS probe for 638 nm illumination. The model is as follows:

$$L = \frac{\lambda_{\text{res}} - 610 + 7.1\theta - 0.3r + \lambda_{\text{termination}}}{1.5}, \tag{6.2.1}$$

where λ_{res} is the resonance wavelength, θ is the half angle and r is the tip radius. The termination constant $\lambda_{\text{termination}}$ accounts for the shift in resonance wavelength due to the termination on a non-vacuum material. Optical modelling showed a termination offset of +15 nm with gold nanocones on silicon and this value is used here. For a 638 nm target resonance wavelength, a 28^o angle and 15 nm tip radius, the length of an optimal gold nanocone is expected to be 158 nm. For a 785 nm target wavelength, the optimal length is estimated to be 256 nm.

6.3 Fabrication

Attempts were made to fabricate gold nanocones and gold nanocaps as shown in Figure 6.1 (a) and (b) respectively. The nanocap fabrication was ultimately unsuccessful and is described in Appendix C. The remainder of this chapter focuses on the fabrication of gold nanocones.

The substrate cantilever is an uncoated Access probe (ACCESS-FM–20) from AppNano. The cantilevers were mounted directly on an aluminium block to minimise potential charging during FIB milling and were secured using adhesive tape as illustrated in Figure 6.3(a). The access probes have a 127^o angle between the cantilever and the back face of the tip and a 107^o angle to the front face. The aluminium mount was designed so that when sitting on a flat surface, a horizontal FIB cut will create a plateau that is normal to the average angle of the tip. This allows the resulting nanocone to maintain the original tip angle for optimal laser alignment. This mounting solution also minimised the handling of cantilevers required throughout the fabrication process.

Figure 6.3(b-e) illustrates the gold nanocone fabrication process. (b→c) The AFM tips were FIB milled using a Zeiss Crossbeam 540 FIB-SEM with a 30 kV, 300 pA gallium beam such that a flat triangular plateau approximately 1 um in diameter was created parallel to the mount base. (c→d) The mount was then placed in an AJA ATC-1800-E electron beam evaporator. 20 nm of titanium at 1 Å/s was deposited followed by 300 nm of gold at 2 Å/s. The titanium acts as an adhesion layer for the gold and improves the otherwise poor adhesion of gold to silicon. The gold layer was made thick enough to accommodate all of the planned nanocone lengths. (c→d)

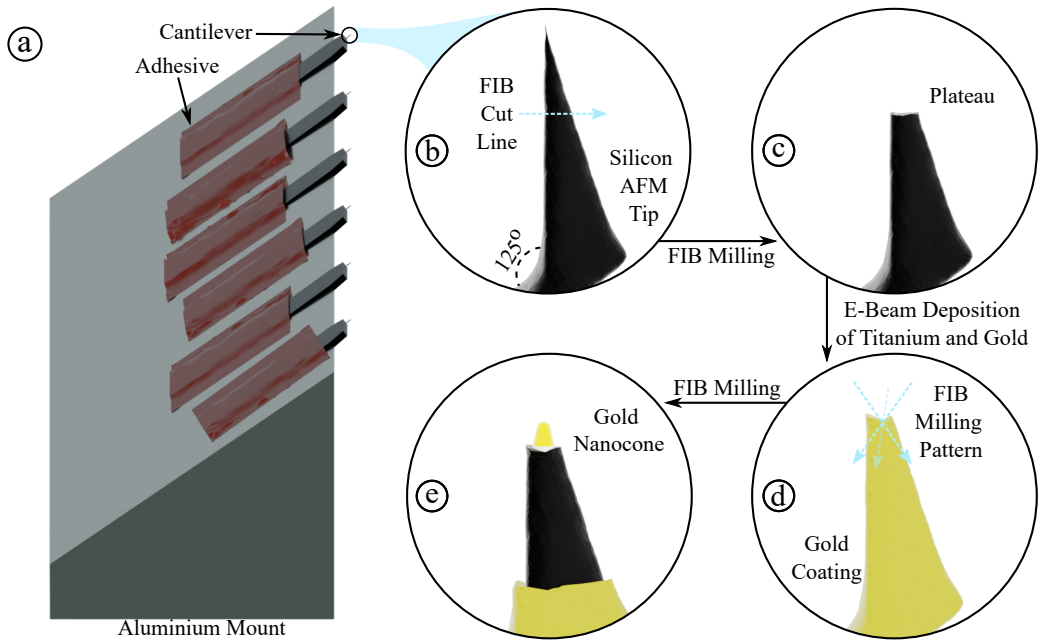

Figure 6.3: Illustration of the method used to fabricate gold nanocones. (a) The cantilevers were mounted on an aluminium wedge to give a convenient horizontal FIB milling angle. The cantilevers are secured using adhesive tape. (b) A zoomed image of the AFM tip with the planned FIB cut line to produce a plateau. (c) FIB milling is used to create a plateau. (d) A thin platinum adhesion layer is deposited followed by a thicker gold layer. (e) FIB milling is used to fabricate an isolated gold nanocone TERS probe.

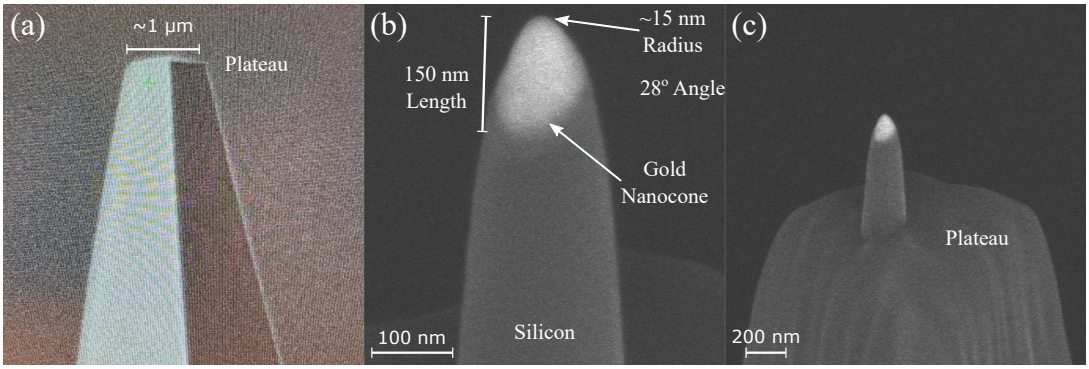

Figure 6.4: SEM images of the fabrication of gold nanocone TERS probes. (a) A 1 μm diameter plateau. (b) A 150 nm long gold nanocone on a silicon pillar. The image is axis corrected, allowing the dimensions to be measured from the SEM image. (c) A view showing the 150-nm long gold nanocone on the silicon plateau.

The cantilevers were then placed into the FIB with the ion beam oriented collinearly with the desired tip axis. A 30 kV, 50 pA Ga beam was scanned in an annular, single-pass, reducing spiral with an outer diameter of 3 μm and an inner void diameter of 200 nm, for a total dose of 0.5 nC/μm^2. This produced a sharp tip approximately 300 nm in length. The overall height of the metal tip was monitored using the secondary electron detector while performing a 0.1 μs dwell time milling scan with the same FIB beam over a 30 μm diameter disk area. The milling was terminated once the desired tip length was achieved.

This fabrication process was performed in collaboration with Steven J. Moody from the Research and Prototype Foundry at the University of Sydney. Of the 12 mounted cantilevers, only 4 gold nanocone probes were successfully fabricated due to handling errors.

Figure 6.4(a) shows an SEM image of the FIB milled plateau with a diameter of approximately 1 μm. A zoomed image of a 150 nm long gold nanocone is shown in (b). The image is axis corrected allowing the dimensions to be measured. This example is 150 nm long, has a 15 nm tip radius and a half angle of 28^o. A zoomed out image of the nanocone and plateau are shown in (c). The nanocone is distant from any other metal layers and will act as an isolated nano-antenna. The lengths of the successfully fabricated nanocones were 150, 175, 225 and 250 nm.

Following the fabrication, the aluminium mount was placed onto a heat pad at 80^{o}C to denature the adhesive tape. This allowed the cantilever and the tape to be pried from the aluminium block. The cantilever and tape were placed onto carbon tape. The increased adhesiveness of the carbon tape allowed the top-side tape to be removed. The cantilever was then removed from the carbon tape and placed into a gel pack.

6.4 Performance Characterisation Method

In Chapter 5, a method was developed that allowed the performance of TERS probes to be reliably measured. In addition, the performance of four commercially available TERS probes were measured and compared. For a more detailed description refer to Chapter 5.2. The same experimental methods are used in this Chapter to measure the performance of the fabricated nanocone TERS probes and compare them to commercially available TERS probes.

Additionally, large area TERS maps of carbon nanotube bundles were collected using a nanocone probe and an Omni-TERS Ag probe. This allows a direct comparison between the collocation of the AFM and TERS maps. The sample for these experiments is a commercially available test sample consisting of CNT bundles and graphite flakes (TS0001 from Horiba, France). The maps were collected using hybrid contact mode.

6.5 Results

The 175, 225 and 250 nm long nanocones initially gave a measurable Raman enhancement. However, soon after alignment, the Raman signal disappeared. It is believed that an increased coupling efficiency of the 785 nm laser with these long nanocones caused the nanocone to melt. The 150 nm long nanocone was able to withstand the laser power and allowed for the collection of the data presented in this chapter. This nanocone is close to the optimal length of 158 nm for 638 nm illumination identified in Chapter 6.2

Figure 6.5 shows the measured PSFs of the gold nanocone probe along with those measured for commercial probes in Chapter 5. The calculated performance metrics are given in Table 6.1.

6.5.1 Performance Metrics: 638 nm Illumination

The PSFs of the gold nanocone probe with 638 nm illumination are shown in Figures 6.5(a1), (b1) and (c1) for the RBM, D-band and G-band respectively. The D-band and G-band PSFs display a single narrow peak. This is due to a single hot spot and will allow the nanocone probe to produce artefact-free TERS maps. Furthermore, the calculated spot diameter of 19 nm is significantly narrower than the commercial probes investigated, where the narrowest spot diameter was 28 nm using the ACCESS Au probe. This demonstrates that nanocone probes can produce higher-resolution TERS maps.

The gold nanocone achieved a mean contrast of 8.05 with 638 nm illumination. This is 28% lower than the Omni-TERS Ag, 6% lower than the ACCESS Au and 650% that of the Omni-TERS Au. Hence, the contrast achievable with the gold nanocones is comparable to the commercial probes tested.

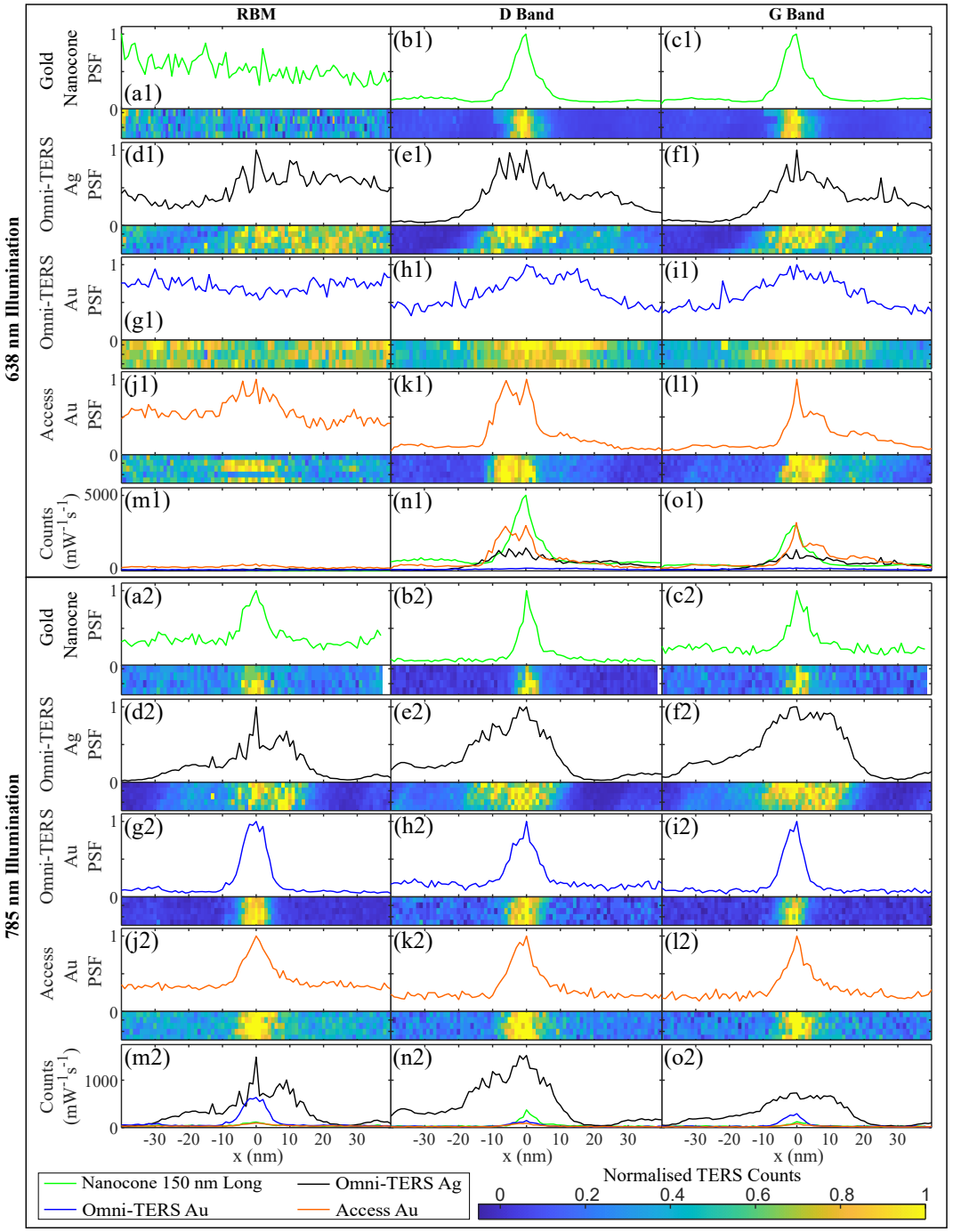

Figure 6.5: Data acquired from high-resolution cross-section TERS maps of SWCNTs. (a1-l1) PSFs with the corresponding normalised TERS maps shown below for 638 nm illumination. (m1-o1) SWCNT cross-sections with counts per mW·s for 638 nm illumination. (a2-o2) PSFs, normalised TERS maps and cross-sections for 785 nm illumination. The PSFs are used to calculate the contrast and spot diameter of each TERS probe, which are summarised in Table 6.1. The gold nanocone fabricated in this chapter provides the narrowest spot diameter while maintaining adequate contrast with 638 nm and 785 nm illumination.

6.5.2 Performance Metrics: 785 nm Illumination

The PSFs of the gold nanocone probe with 785 nm illumination are shown in Figures 6.5(a2), (b2) and (c2) for the RBM, D-band and G-band respectively. The PSFs for the RBM, D-band and G-band all display a single peak. This supports the previous conclusion that this probe has a single hot spot. The calculated spot diameter of 12.5 nm is the lowest of all measured TERS probes. This result demonstrates that the nanocone probe can provide an optical resolution superior to the commercial TERS probes tested.

The gold nanocone achieved a mean contrast of 6.59 with 785 nm illumination. This is comparable to the contrast measured with the Omni-TERS Au and ACCESS Au probes but is only 22% of the Omni-TERS Ag probe. One possible explanation is that the 150 nm long nanocone is not long enough to adequately excite the fundamental plasmon mode at this wavelength. It is expected a nanocone of optimal length would provide improved contrast.

Table 6.1: Performance characteristics of TERS probes for imaging SWCNTs at 638 nm and 785 nm laser excitation.

Probes	Wavelength (nm)	Contrast RBM	Contrast D	Contrast G	Contrast Mean	Spot Diameter (nm)
Gold Nanocone	638	N/A	8.27	7.27	8.052	19
150 nm Long	785	1.80	10.07	3.12	6.59	12.5
Omni-TERS	638	N/A	13.59	9.82	11.21	57
Ag	785	24.61	44.11	21.13	30.62	52
Omni-TERS	638	N/A	1.13	1.39	1.26	45
Au	785	13.73	3.62	7.23	8.19	16
ACCESS	638	1.14	9.48	7.68	8.58	28
Au	785	2.04	3.80	3.65	3.17	20

6.5.3 TERS Mapping

Figure 6.6 shows the mapping of CNT bundles on a gold substrate collected using the Omni-TERS Ag probe. This probe features a grainy surface as shown in Figure 5.6(a). Figure 6.6(a) shows the TERS D-band map and (b) shows the AFM height map. Features are identified and labelled on the TERS map. The TERS D-band counts and AFM height are plotted in (c-d) as a function of distance along the x-profile and y-profile respectively. There appears to be a minor offset between the TERS and height maps in the x-axis with feature 1 peaking in the height map 12 nm after peaking in the TERS map. The offset is more significant in the y-axis with feature 3 peaking 72 nm earlier in the TERS map compared to the height map. This offset makes the identification of structures difficult as the AFM height and TERS maps have a spatial offset, which becomes significant when small scan areas are used. For example, if a 100 x 100 nm scan area is used then most features appearing on the TERS map will be missing in the topography map and vice versa.

Figure 6.7 shows the mapping of CNT bundles on a gold substrate collected using the nanocone TERS probe, (a) shows the TERS D-band counts and (b) shows the AFM height map. The D-band counts and AFM height as a function of distance along the x-profile and

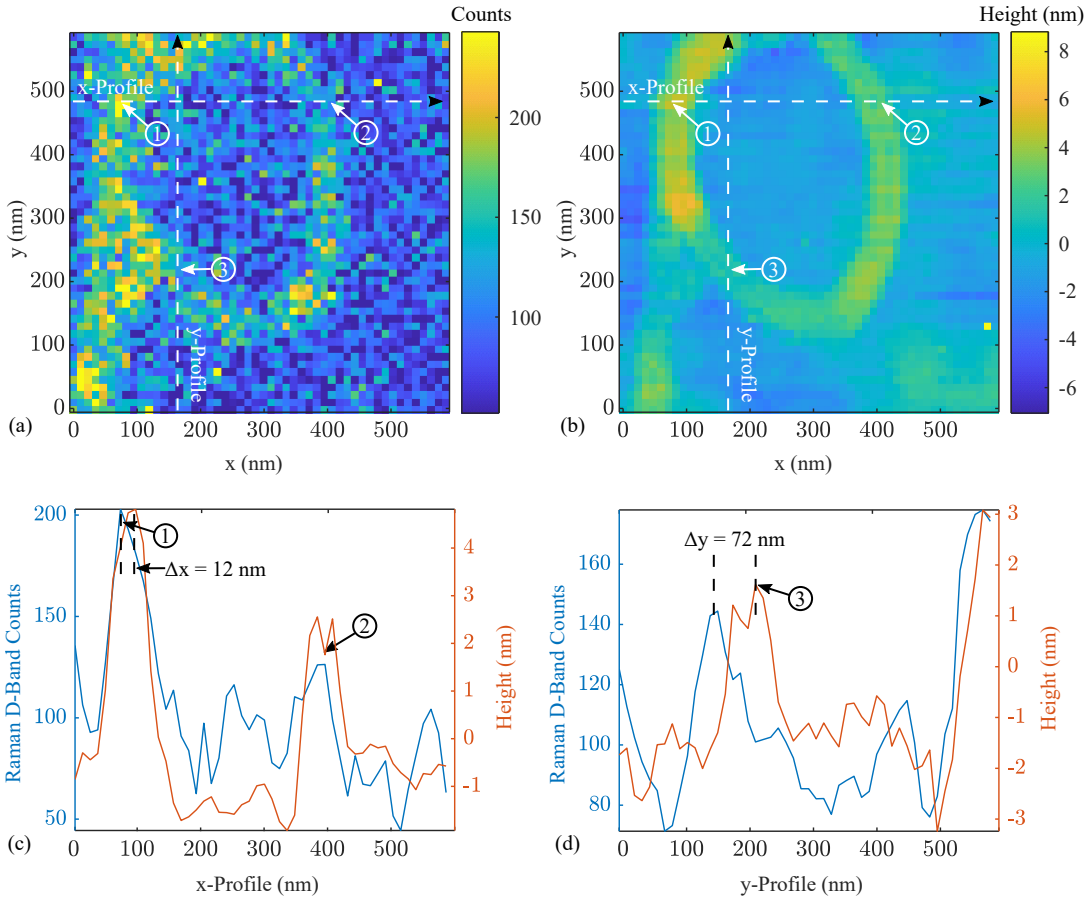

Figure 6.6: Mapping of CNT bundles on a gold substrate collected using an Omni-TERS Ag probe. (a) D-band TERS map with features labelled 1-3. (b) AFM height map. (c) Raman D-band counts and AFM height along the x-profile. There is an approximately 12 nm offset between the TERS and height maps in the x-axis. (d) Raman D-band counts and AFM height along the y-Profile. There is an approximately 72 nm offset between the TERS and height maps in the y-axis. The poor collocation seen here is typical of TERS probes with grainy surfaces.

y-profile are plotted in (c) and (d) respectively. The AFM and TERS maps are collocated with features appearing at the same position in both axes. This means that TERS and Raman maps will be collocated, allowing for more accurate surface characterisation, particularly when performing small-area, high-resolution scans.

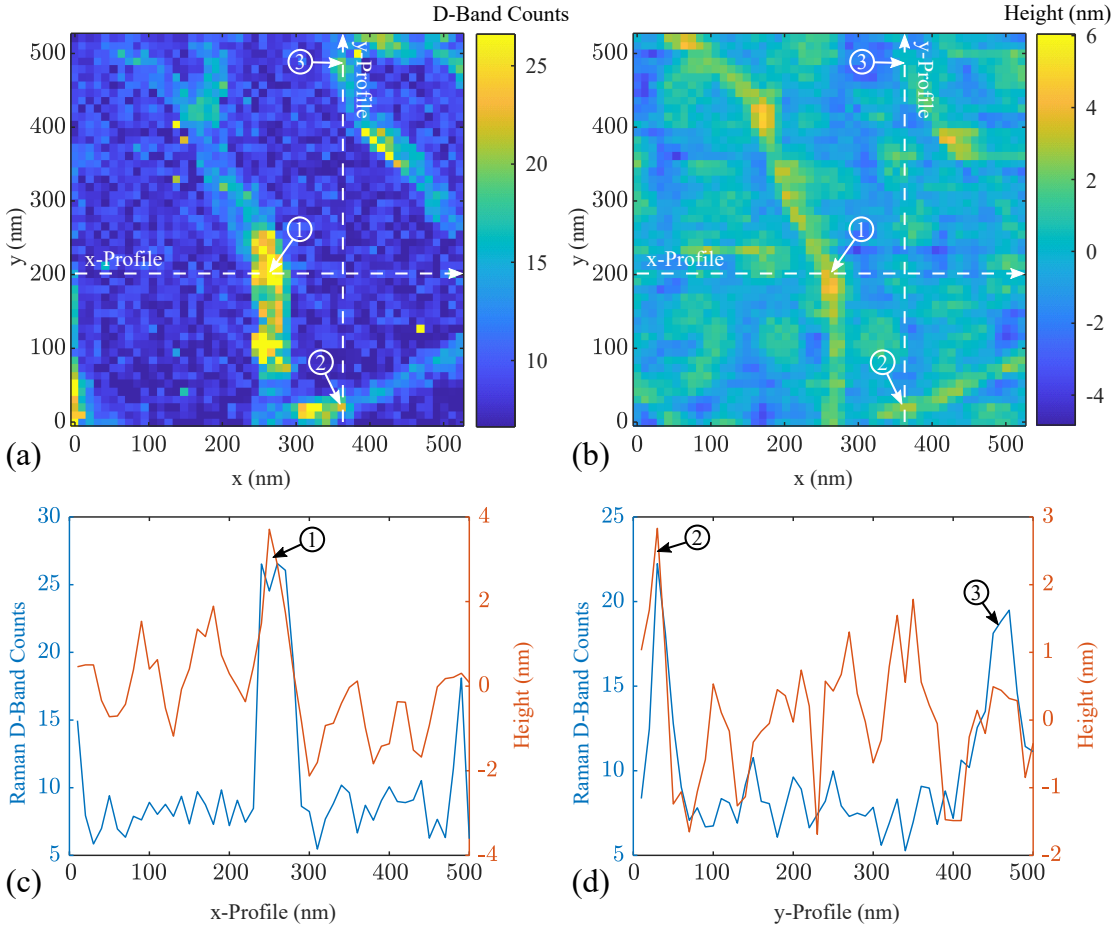

Figure 6.7: Mapping of CNT bundles on a gold substrate collected using the nanocone TERS probe described in this chapter. (a) D-band TERS map with features labelled 1-3. (b) AFM height map. (c) Raman D-band counts and AFM height along the x-profile. The gold nanocone TERS probe provides collocated TERS and AFM maps.

6.5.4 Chemical Stability

The TERS maps presented in this work were acquired 12 days after the gold nanocone TERS probes were fabricated. The probes were stored in ambient conditions. There did not appear to be a noticeable drop in performance over this time period. A microscope software failure resulted in the probe being crashed into the sample. Thus, follow-up measurements could not be performed to measure long term performance stability. However, given the chemical stability of gold, it is likely that the nanocone probes provide superior lifetimes than commercially available silver probes.

6.6 Simulations

Figure 6.8 shows BEM simulation results comparing the performance of grainy silver probes to a gold nanocone. The enhancement maps for several grain configurations are shown in (a-d) where the base probe is a silver nanocone with a 40 nm radius and 15 nm radius nanospheres acting as grains. The enhancement map for a gold nanocone with a 15 nm radius is shown in (d). The enhancement as a function of x-position is shown in (3) for the various geometries. The grainy probes result in a broader enhancement cross-section with multiple hot spots. This is a consequence of multiple plasmon enhancement sites close to the tip apex. Meanwhile, the gold nanocone results in a single and narrow hot spot. Thus, the superior experimental performance displayed by the gold nanocone TERS probe is due to having a single enhancement site near the apex, which results in a single, narrow enhancement hot spot.

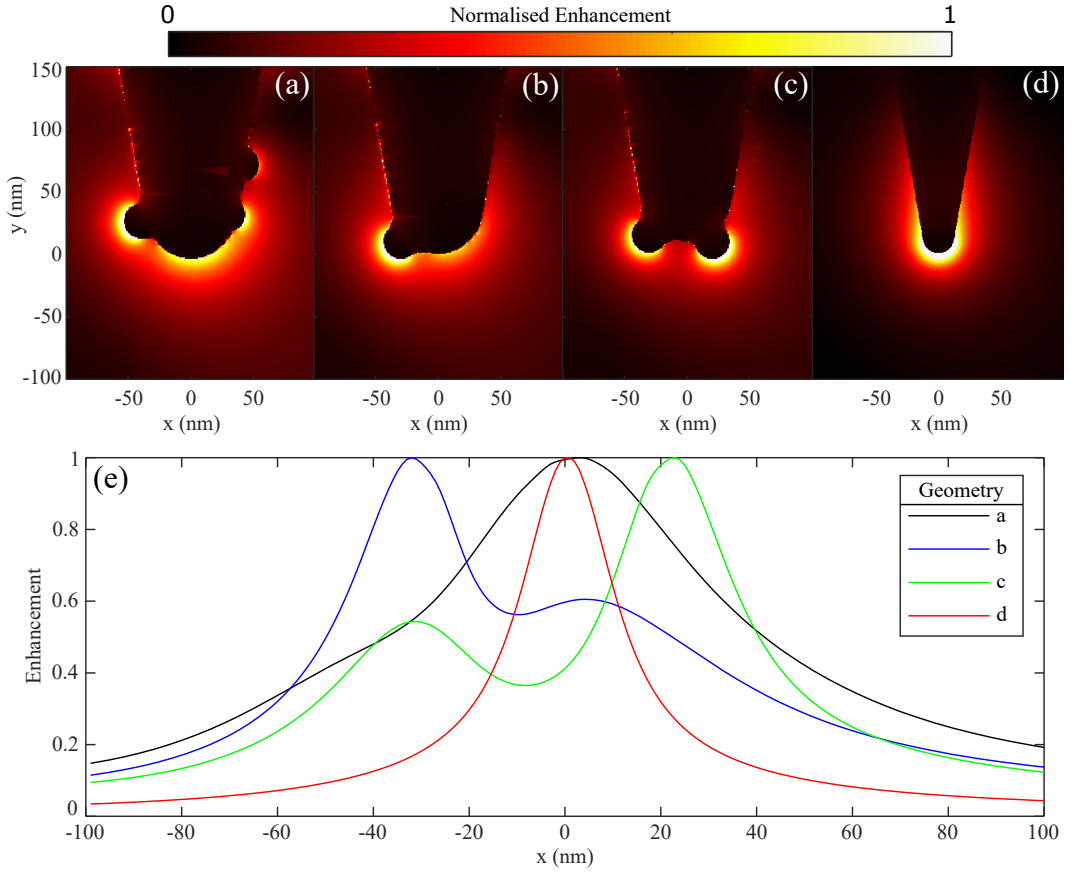

Figure 6.8: BEM simulations comparing grainy silver TERS probes and a gold nanocone. Normalised enhancement maps are shown for (a) multiple grains offset from the apex, (b) a single grain offset from the apex and (c) two grains acting as the apex. These grainy probes consist of a silver nanocone with a 40 nm radius and 15 nm radius nanosphere grains. (d) Shows the enhancement map for a gold nanocone with a radius of 15 nm. (e) Shows the enhancement verses x-position under the tip apex. The nanocone geometry results in an enhancement cross-section with a single narrow hot spot. Meanwhile, the grainy geometries result in multiple hot spots and a broader peak.

6.7 Conclusion

The gold nanocone TERS probe presented in this chapter addresses the limitations of commercial probes. These limitations are circumvented by removing the random grain formation used with commercial probes and instead using an optimised smooth gold nanocone. The nanocone probe exhibited the narrowest spot diameter of 12.5 nm and 19 nm measured with 638 nm and 785 nm illumination respectively. The nanocone contrast was comparable to the commercial probes with 638 nm and 785 nm illumination. The nanocone also provided artefact free and collocated TERS and AFM height maps due to the single TERS hot spot and mechanical apex. Finally, the nanocone probe was able to be stored in ambient conditions without noticeable performance degradation. These factors strongly support the use of gold nanocone probes for high-speed, high-resolution TERS imaging. To the authors knowledge, the work presented here contains the first high-resolution TERS maps acquired with a gold nanocone TERS probe.

6.8 Future Work

Due to the COVID-19 pandemic and associated restrictions, probe fabrication took longer than expected due to access limitations at fabrication facilities. The experimental data presented in this chapter was measured using a single 150 nm long gold nanocone. Future work should include a statistical analysis of multiple probes with various dimensions to allow the relationship between dimensions and length to be investigated, along with statistical variations in performance. The stability of the probes should also be tested over a longer time period so that storage protocols can be developed.

Chapter 7

Modulated-Illumination Intermittent-Contact TERS

This chapter describes a new TERS imaging mode where the illumination laser is modulated during intermittent-contact AFM, which will be referred to as modulated-illumination intermittent-contact TERS (MIIC-TERS). The modulation is synchronous with the cantilever oscillation so that the tip is only illuminated for a brief duration while the tip is very close to, or in contact with the sample. This allows the high Raman enhancement of contact mode TERS to be maintained while reducing the tip-sample forces that result in tip contamination and sample damage. Modulating the laser also reduces the tip and sample heating compared to constant illumination The MIIC-TERS method is experimentally demonstrated using a grainy silver probe and a gold nanocone probe. The effect of AFM setpoint and laser duty cycle are predicted theoretically and verified experimentally.

Publications Arising from This Chapter

- M. G. Ruppert, B. S. Routley, L. R. McCourt, Y. K. Yong , A. J. Fleming, "Modulated-Illumination Intermittent-Contact Tip-Enhanced Raman Spectroscopy: Simultaneous Imaging of Surface and Material Properties," *Nature Communications*, Submitted.

  Author Contributions:

  - Experimental work 50%
  - Optical modelling
  - Data analysis 50%

7.1 Introduction

TERS enhancement is dependent on the tip-sample separation [53]. Figure 7.1(a) shows the optimal condition where the tip is in contact with the sample, resulting in maximum enhancement, which produces a strong Raman signal. Figure 7.1(b) shows a tip that is retracted, resulting in reduced enhancement at the sample. The spectrometer will still collect light that originates from outside the near-field volume. Hence, the TERS signal-to-noise will be reduced. Figure 7.1(c) shows that the enhancement as a function of tip-sample separation as calculated using boundary element simulations and presented in Chapter 3.3.1. Hence, the average enhancement at the sample depends on the cantilever dynamics.

The following section describes the contact, hybrid-contact and intermittent-contact TERS modes. These modes are based on AFM modes that have distinct advantages and disadvantages. Modulated-illumination intermittent-contact TERS (MIIC-TERS) is introduced as a method that combines the advantages of the formerly mentioned modes. MIIC-TERS has been presented in the literature previously in the bottom illumination configuration with 1D line scans of a carbon nanotube [177]. In this chapter, MIIC-TERS is demonstrated in the side-illumination configuration and high-resolution TERS images are presented.

7.1.1 TERS Modes of Operation

Contact

Figure 4.2 shows a schematic for the experimental setup used to perform TERS in contact mode. The probe is kept in physical contact with the sample while a scan is performed. The tip-sample forces are predominantly repulsive due to electron-electron repulsion. The most common method for maintaining the tip-sample separation is the constant force mode. In this mode, the sample z-position is altered using a piezoelectric nanopositioner with a feedback loop, which aims to keep the optical beam deflection signal constant [125]. The z-axis controller signal is used to generate the AFM topography estimate. Laser light from the Horiba XploRA plus unit is directed through a series of mirrors and focused through a side objective lens onto the apex of the metal AFM tip. The geometry of the laser requires the tip to be angled with respect to the cantilever. The Raman scattered light is generated by molecules on the sample and collected by the illumination objective. This light is then directed back into XploRA spectrometer where the Raman signal is acquired.

Contact mode often results in damage to the sample and tip as high shear forces may displace surface particles or modify the fragile surface metal layer of some TERS probes [46, 126]. Furthermore, there is a high chance that sample molecules may attach to the TERS tip, which can introduce a constant Raman signal independent of the surface chemistry [178]. The advantage of contact mode TERS is that the tip-sample separation is minimised resulting in maximum Raman enhancement and therefore, the highest signal-to-noise ratio.

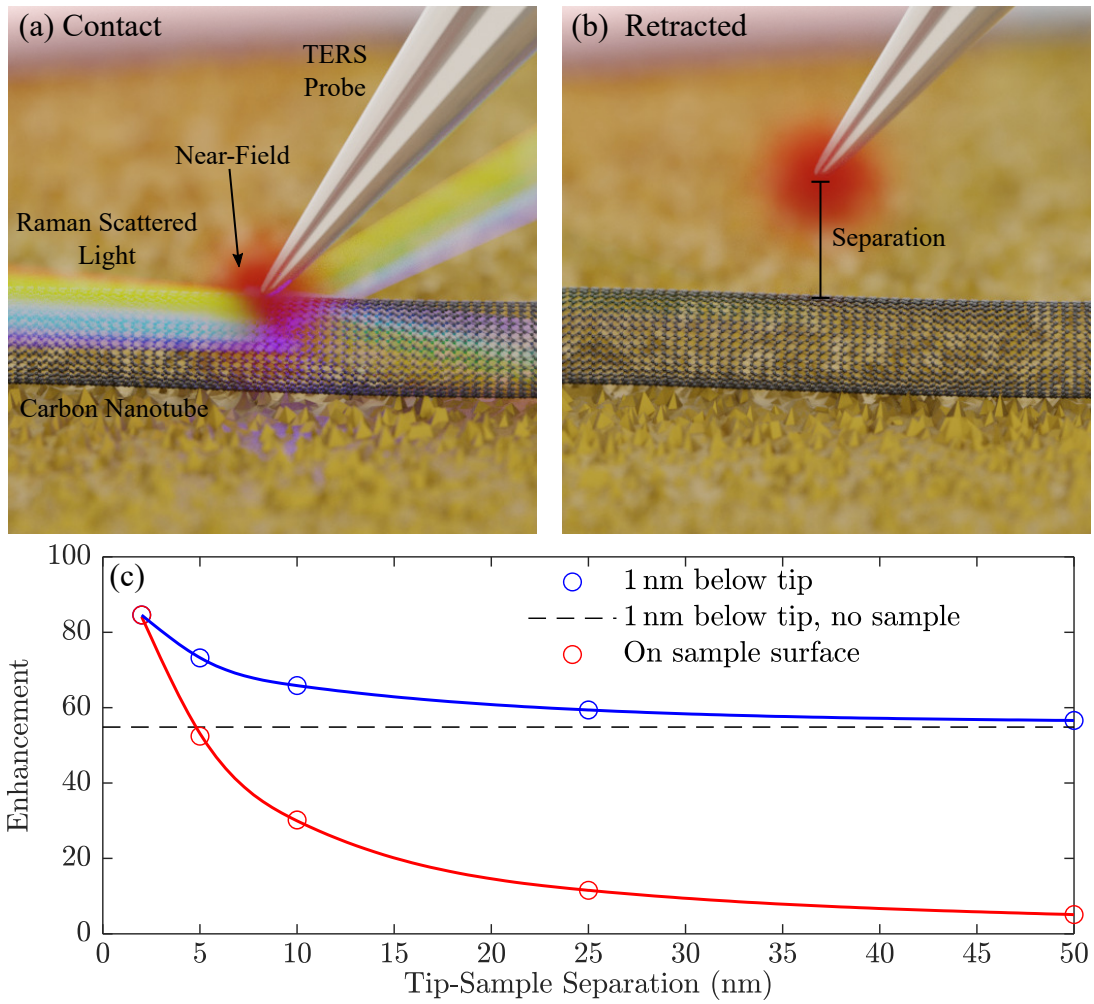

Figure 7.1: The effect of tip-sample separation on enhancement. The illustrations show Raman scattering when the tip is (a) in contact with the sample and (b) when retracted. (c) Enhancement versus separation as measured below the tip apex, at the sample and below the tip apex with no substrate present. These results were calculated using BEM simulations for a gold nanocone with an apex diameter of 20 nm and were first presented in Chapter 3.3.1.

Intermittent Contact

Intermittent, or contact mode TERS, is performed by oscillating the cantilever at its resonance frequency using a piezoelectric actuator [127]. For reference, the cantilevers used in this thesis have a resonance frequency between 50 kHz - 150 kHz and the free-air amplitude is typically between 20-60 nm. When the tip comes into contact with the sample surface, energy is dissipated and the oscillation amplitude is reduced [128]. A feedback loop is used to maintain a constant oscillation amplitude by varying the sample z-position, allowing the topography to be tracked. Intermittent contact mode reduces the tip-sample friction when compared to contact mode due to the absence of lateral tip forces. Low oscillation amplitudes reduce tip-sample contact, which decreases sample deformation. High oscillation amplitudes increase sample deformation, which is suitable for stiff samples and has the advantage of improved lateral resolution [179].

The advantage of intermittent contact mode is a reduction in tip-sample friction, which reduces shear forces. This allows intermittent contact mode to be used for softer samples than is possible using contact mode without damaging the sample [126]. Furthermore, the reduced tip-sample interaction reduces the likelihood of probe damage or contamination adhering to the probe that would reduce enhancement or introduce artefacts into the Raman spectrum [178].

The disadvantage of intermittent contact is the decreased Raman signal and signal-to-noise ratio. The average tip-sample separation is greater than contact mode for the majority of the oscillation cycle, which decreases the average electric field enhancement at the sample. Thus, the measured TERS signal will have increased far-field contributions and the system noise may obscure spectral peaks. As a result, TERS maps acquired using intermittent contact mode display poor contrast.

Hybrid Contact

The hybrid contact mode switches between contact and intermittent contact modes to maximise Raman signal and minimise damage to the probe and sample. Hybrid contact mode is performed by acquiring the Raman spectra of a pixel in contact mode before switching the z-axis feedback to constant amplitude intermittent contact mode for topography acquisition. When the next pixel is reached, the system switches back to contact mode and another spectrum is acquired. Since the Raman spectra is only acquired while the tip is in contact with the sample, the signal-to-noise ratio is maximised. However, switching between contact and tapping mode at every pixel slows acquisition and may result in poor topography measurements.

Laser beams exhibit pointing drift over time. High-frequency drift is a consequence of vibrations in the optical setup including mirrors and the laser itself, or fluctuations in the refractive index of air along the beam path. Lower frequency drift is most commonly the consequence of thermal changes in optical components. For example, the heating of a mirror or mount will result in a variation in output laser angle and position [183]. The enhancement of a TERS probe is highly dependent on the position of the excitation laser beam at the tip apex. Therefore, laser pointing drift will result in decreased enhancement as TERS scan duration increases. As a result, TERS maps acquired with long scan times often exhibit a decrease in optical contrast with time and give a poor representation of the sample. For short acquisition times, the effects

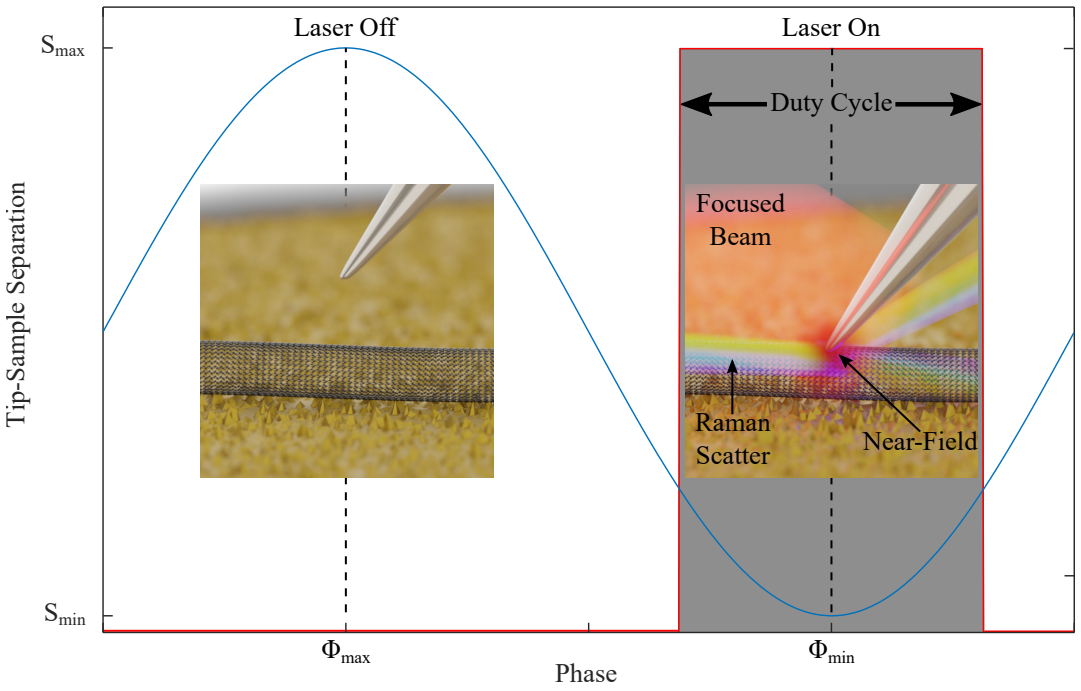

Figure 7.2: MIIC-TERS laser timing. The tip-sample separation is shown over one cantilever oscillation, the laser is off when the tip-sample separation is large, which reduces far-field scatter contributions measured by the spectrometer. The laser is on when the tip-sample separation is minimised, which results in maximum enhancement at the sample and a high near-field Raman signal detected at the spectrometer.

of pointing drift can be ignored. For large scans, the slow scan speed of hybrid contact mode TERS requires compromises to either spectrum acquisition time or scan resolution to minimise scan time and the associated optical drift.

The hybrid contact mode is a preset mode of the Horiba NanoRaman system and was used extensively in this thesis due to the high Raman enhancement that is achieved.

MIIC-TERS

In intermittent contact mode, the tip is only in contact with the sample for a small fraction of a cycle [127]. If TERS signal acquisition and tip illumination are performed over the entire cycle, the signal-to-noise ratio is reduced as the enhancement is small when the tip is not in contact with the sample. By modulating tip illumination [177] or time-gating the spectrometer [53, 118] to the tip-sample contact interval, the signal-to-noise can be kept comparable to TERS operated in contact mode.

MIIC-TERS combines the high-speed, non-destructive attributes of intermittent contact with the high-enhancement of contact mode. This is achieved by modulating the illumination laser on when the tip-sample separation is small. This increases the average enhancement at the sample over an oscillation cycle when compared to constant-illumination intermittent contact mode. The laser is off when the tip-sample separation is large, which reduces the signal collected by

the spectrometer from far-field scatter [177]. Figure 7.2 illustrates the operation of MIIC-TERS over one oscillation cycle. The duty cycle is the percentage of time that the laser is turned on.

The disadvantage of MIIC-TERS is a lower total Raman signal per unit time as the laser illumination is intermittent. However, the tip-sample shear forces are reduced compared to contact mode, which reduces the probability of sample damage or tip contamination. Compared to hybrid contact, MIIC-TERS offers improved scan speeds and improved topography estimates as the switching between contact and intermittent contact is removed. In addition, low duty cycles reduce the probe temperature, or allow higher laser power to be used to increase the Raman signal. Lower laser power is a significant advantage of MIIC-TERS compared to a time-gated spectrometer where laser illumination is constant. The following sections focus on modelling the performance of MIIC-TERS in terms of cantilever dynamics, the implementation of MIIC-TERS and the characterisation of system performance based on the cantilever dynamics.

The following sections focus on modelling the performance of MIIC-TERS in terms of cantilever dynamics, the implementation of MIIC-TERS and the characterisation of system performance based on the cantilever dynamics.

7.2 Modelling

The enhancement at the sample depends on the cantilever dynamics and the laser modulation. Large cantilever oscillation amplitudes increase the average tip-sample separation and lower setpoints will affect the tip-sample contact time. The laser modulation duty cycle and phase offset will affect the enhancement at the sample and the total amount of signal collected at the spectrometer. This section discusses the cantilever dynamics that affect the performance of a MIIC-TERS system using optical and mechanical models.

7.2.1 Optical Simulations

Boundary Element Method (BEM) simulations were used to simulate the optical response of a 1 μm long silver nanocone with a 200 nm radius tip apex and a 15^o half angle above a glass substrate with a 638 nm planewave illumination. The resulting surface charges were used to calculate the electric-field enhancement at the sample surface. This was repeated with several tip-sample separations. An exponential model of the form $f(x) = ae^{bx} + ce^{dx}$ was fit to the enhancement as a function of tip-sample separation. The resulting fit is given in Figure 7.3(a) with the following coefficients a = 42.7, b = -0.2108, c = 16.65, d = -0.0337.

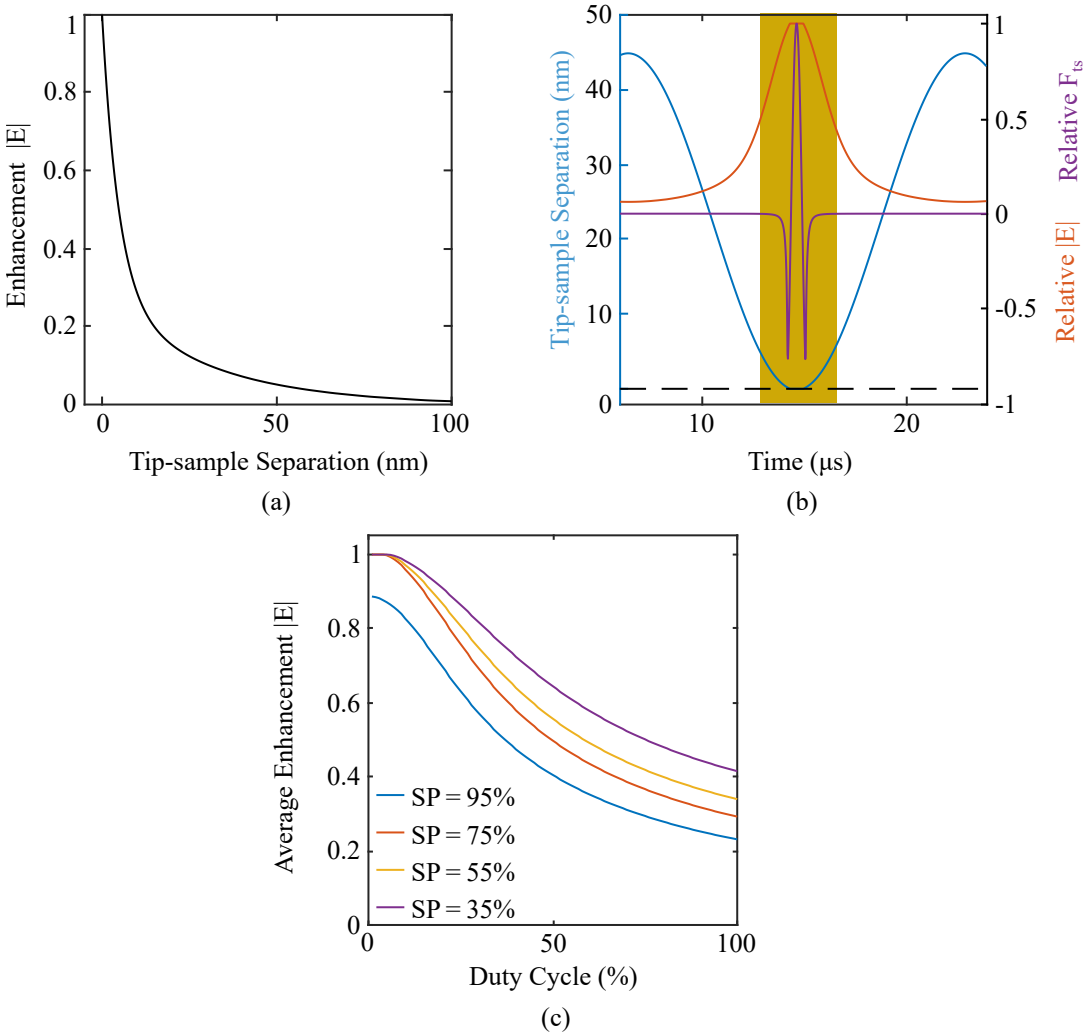

Figure 7.3: Simulations used to study the effects of AFM imaging parameters and TERS tip illumination on average electric field enhancement at the sample during tapping mode operation. (a) Shows the relative electric field enhancement at the sample as a function of tip-sample separation, calculated using boundary element method simulations. (b) Shows time domain simulations of AFM dynamics over an oscillation period. The tip-sample separation is shown in blue. The relative electric field enhancement is shown in orange and is maximised when the tip is in contact with the sample. The tip-sample force F_{ts} is shown in purple. The highlighted area illustrates the definition of the illumination duty cycle. (c) Shows the average electric field enhancement at the sample as a function of the illumination duty cycle and AFM setpoint. The highest average electric field enhancement is observed when the illumination duty cycle is limited to the interval that the tip is in contact with the sample.

7.2.2 Cantilever Dynamics

The cantilever dynamics when interacting with a gold sample are modelled by solving

$$y''(t) + \frac{\omega_0}{Q}y'(t) + \omega_0^2 y(t) = u(t), \tag{7.2.1}$$

where the input force is given by

$$u(t) = \frac{\omega_0^2}{k}[F_{\mathrm{d}} sin(\omega_0 t) + F_{\mathrm{ts}}(d,t)], \tag{7.2.2}$$

with tip-sample separation d, quality factor Q, resonance frequency f, drive force amplitude F_{d} and tip-sample force as a function of tip-sample distance $F_{\mathrm{ts}}(d,t)$ [180]. The Derjaguin-Muller-Toporov model is used for the tip-sample interaction, which uses classical Hertz contact mechanics with attractive van der Waals forces [181]. The simulations resulted in repulsive tip-sample interactions with setpoints of 35%, 55% and 75%. The repulsive interactions indicate that these setpoints produce intermittent contact with the sample. A setpoint of 95% gives an attractive tip-sample interaction, indicating no contact between the tip and sample. The model parameters are given in Table 7.1, which were adapted from published data [182]. An example of the calculated tip-sample separation and tip-sample force is shown in Figure 7.3.

Table 7.1: Parameters used for AFM cantilever dynamics simulation. Adapted from [182].

Parameter	Description	Value
A_0	Free air amplitude	30 nm
Q	Quality factor	200
k	Stiffness	10 N/m
F_{d}	Drive force amplitude	kA_0/Q
ω_0	Resonance Frequency	$2\pi 60$ kHz
SP	Setpoint	35
R	Tip radius	200 nm
a_0	Atomic separation	0.164 nm
E_{t}	Elastic modulus tip	13- GPa
v_{t}	Poisson ratio tip	0.3
E_{s}	Elastic modulus sample	80 GPa
v_{s}	Poisson ratio sample	0.3
H	Hamaker constant	$7.1\mathrm{e}^{-20}$ J

7.2.3 Combined Model

The enhancement model was incorporated into the cantilever tip-sample separation curves to calculate the relative enhancement at each separation. An example of the enhancement as a function of tip-sample separation over a cantilever oscillation cycle is shown in Figure 7.3(b). This was repeated for setpoints of 35%, 55%, 75% and 95%. The average electric field enhancement over an oscillation cycle was calculated as a function of the laser modulation duty cycle with the laser pulse aligned to the tip-sample contact time.

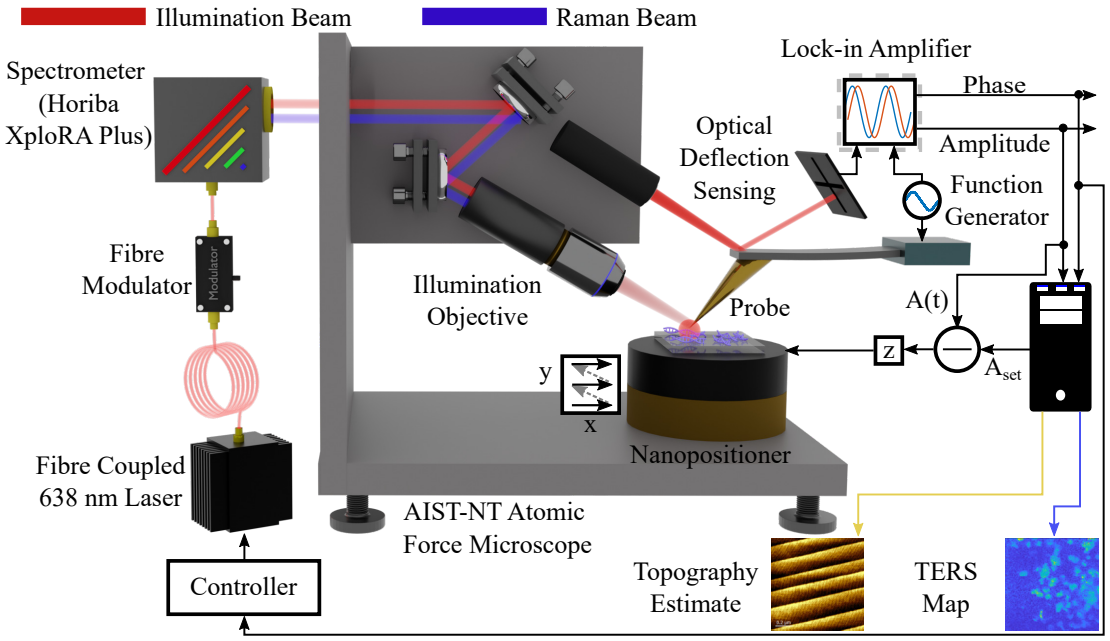

Figure 7.4: Schematic of the experimental setup used for MIIC-TERS. The lock-in amplifier phase is used to control the acousto-optic modulator (AOM). The AOM modulates the illumination laser in phase with the tip-sample contact interval. The duty cycle is adjusted to obtain an adequate Raman signal.

Figure 7.2(c) shows the simulated average electric field enhancement over an oscillation period as a function of duty cycle and AFM setpoint. The average enhancement is maximised when the duty cycle is approximately 5%, which corresponds to the tip-sample contact interval. Increasing the duty cycle will yield a higher signal as the spectrometer will collect more light. However, the TERS signal-to-noise ratio will decrease as far-field contributions will become more significant when the near-field enhancement is decreased. A 100% duty cycle represents constant tip illumination and spectrometer collection. In this case, the average enhancement at the sample ranges from 30% to 50% compared to contact mode depending on the amplitude setpoint. Thus, constant illumination will result in a poor Raman signal-to-noise ratio. In addition, the AFM setpoint must be sufficiently low to ensure the tip makes contact with the sample. This is evident by observing that the 95% setpoint does not achieve an average enhancement of 1, even with an arbitrarily small duty cycle. Finally, low setpoints give a higher average enhancement for large duty cycles. This would allow an increased signal per unit time to be acquired and higher scanning speeds to be achieved. However, low setpoints increase the tip-sample interaction and increase the likelihood of tip damage, sample damage or tip contamination.

7.3 Experimental Results

7.3.1 Experimental Setup

Figure 7.4 shows a schematic of the experimental setup used to perform MIIC-TERS. A 638 nm fibre coupled laser is used with a 40 mW power output. The lock-in amplifier acquires the cantilever deflection signal phase, which is then used to drive the acousto-optic modulator (AOM). The resulting acoustic waves act as a diffraction grating, causing the input laser beam to be diffracted. This allows the AOM to rapidly modulate the illumination beam in phase with the cantilever oscillations. The spectrometer and filters are contained in the Horiba XploRA Plus unit and the AFM scanning is controlled with the AIST-NT atomic force microscope. The phase offset of the modulator drive signal is varied to maximise the Raman signal-to-noise ratio. The duty cycle is adjusted to obtain adequate Raman counts. However, an excessive duty cycle will reduce the signal-to-noise ratio as the average electric field enhancement at the sample will be reduced.

7.3.2 Performance Analysis

Grainy Silver Probe

Figure 7.5 shows a comparison of hybrid and MIIC-TERS imaging modes. These maps were acquired using an Omni-TERS Ag probe, that features a grainy surface, and a Horiba test sample consisting of CNT bundles and graphite flakes on a gold substrate. All imaging was performed using the 638 nm laser and the average power was normalised to 1 mW. The setpoint for MIIC-TERS imaging was 50% with a 60 nm free air amplitude. A 0.5 s acquisition time was used.

The hybrid TERS maps have the highest contrast as shown in Figure 7.5(a1). The 10% duty cycle MIIC-TERS map (b1) allows the CNT loop to be identified but the contrast is lower than the hybrid image. Constant-illumination intermittent-contact TERS (c1) provides no contrast between the CNT and sample. The decreased contrast is expected as the average enhancement at the sample is reduced with an increased duty cycle, as shown in Figure 7.3(c).

The AFM maps provide a similar contrast with the CNT clearly visible in the maps from each mode. However, the Hybrid mode AFM map (a2) displays many artefacts.

Gold Nanocone Probe

Figure 7.6 shows D-band TERS (a1-c1) and AFM (a2-c2) images that compare the hybrid and MIIC-TERS imaging modes. These maps were acquired with the 150 nm gold nanocone probe described in Chapter 6.

Hybrid and 50% setpoint MIIC-TERS provide equivalent TERS image quality as shown in Figure 7.6(a1) and (b1). The 70% setpoint MIIC-TERS image (c1) provides considerably lower contrast and the CNT bundle is difficult to identify. This is likely due to the lower contact time with the higher setpoint.

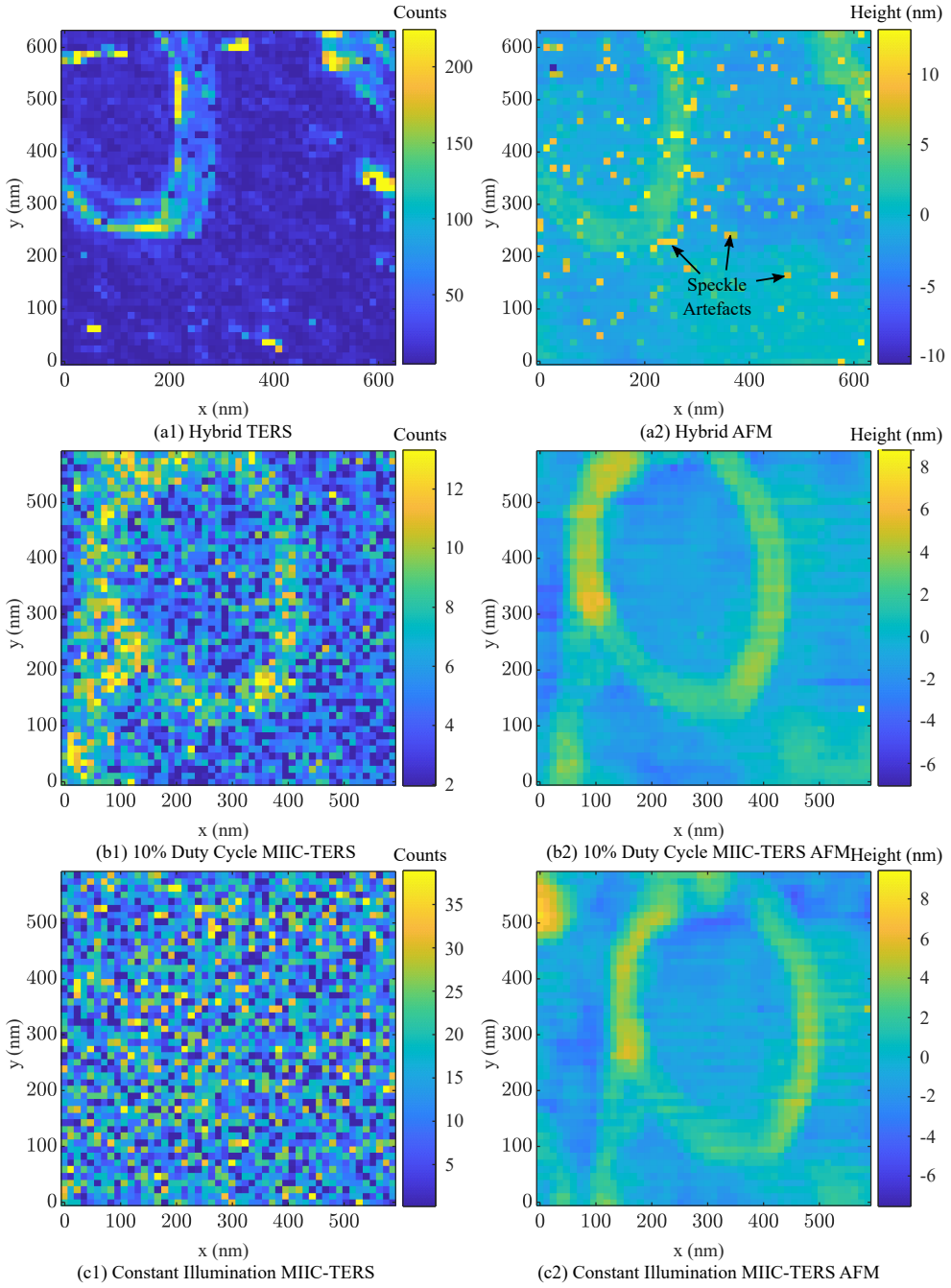

Figure 7.5: A comparison of TERS imaging modes acquired using an Omni-TERS Ag grainy probe and a sample of CNT bundles on a gold substrate with 638 nm laser excitation. MIIC-TERS was performed with a 50% setpoint. All maps were acquired with an average laser power of 1 mW. D-band TERS maps are shown for (a1) hybrid mode, (b1) 10% duty cycle MIIC TERS and (c1) constant illumination intermittent contact TERS. The associated AFM height maps are shown in (a2), (b2), (c2). The hybrid mode provides the best TERS maps with high contrast. The 10% duty cycle MIIC-TERS map shows low contrast of the CNT bundle. The constant-illumination TERS map shows no contrast of the CNT bundle. The height maps are similar except for point artefacts in the hybrid AFM map.

The Hybrid mode produced the best AFM height map with the CNT structures clearly visible in Figure 7.6(a2). The AFM images acquired using MIIC-TERS display poor contrast between the CNT structures and the substrate. The reason for the poor AFM imaging with MIIC-TERS is unknown at this stage but is believed to be due to the number signal acquisition samples used from the z-axis controller in the Horiba software and will be investigated as part of future research.

Grainy Silver vs Gold Nanocone Probe

The MIIC-TERS maps for the Omni-TERS Ag grainy probe in Figure 7.5(b1) and the gold nanocone probe in Figure 7.6(b1) were both acquired using 10% duty cycle and a 50% setpoint. The nanocone produced a map with superior contrast. Notably, the nanocone provided similar contrast with MIIC-TERS and hybrid modes. On the other hand, the grainy probe performed significantly worse with the MIIC-TERS mode.

It is believed that the grainy probe performs worse with MIIC-TERS as there is an offset between the physical tip apex and the primary hot spot located on a metal grain. This is illustrated in Figure 7.7(a). With a low sample indentation, there is a significant distance between the primary hot spot and the sample. This will reduce the Raman enhancement with the magnitude of the effect depending on the separation. As the sample indentation is increased, a point will be reached when the separation between the hot-spot and surface is minimised and the resulting Raman enhancement is maximised. Hence, MIIC-TERS with lower tip-sample indentation will result in a lower TERS signal compared to the hybrid mode where the indentation is higher. When the physical tip apex and primary hotspot are collated there is no indentation required to minimise the hot spot-sample separation. This is the case for a gold nanocone as illustrated in Figure 7.7(b). Hence, the TERS signal for hybrid and MIIC-TERS should be the same if normalised for tip-sample contact time when using the gold nanocone.

The MIIC-TERS AFM maps acquired with the gold nanocone probe show reduced contrast for the CNT bundle compared to those acquired with the hybrid mode. This issue is not present in the AFM maps acquired using the grainy probe. The cause of this is unknown at present and will be investigated as part of future research.

Duty Cycle and Setpoint

To measure the effects of setpoint and duty cycle, an experiment was conducted using the Omni-TERS Ag probe on a sample of SWCNTs on a gold substrate. The probe was positioned above a SWCNT and Raman spectra were collected for various setpoints and duty cycles.

Figure 7.8(a) shows an example TERS spectrum of a CNT bundle on a gold substrate using an Omni-TERS Ag probe. The background is estimated using a 6^{th} order polynomial from the spectrum with the D and G bands removed. The D-band contrast was calculated using:

$$C = \text{Counts}_{\text{real}}/\text{Counts}_{\text{background}}. \tag{7.3.1}$$

The D-band contrast as a function of the laser duty cycle for different AFM setpoints is shown

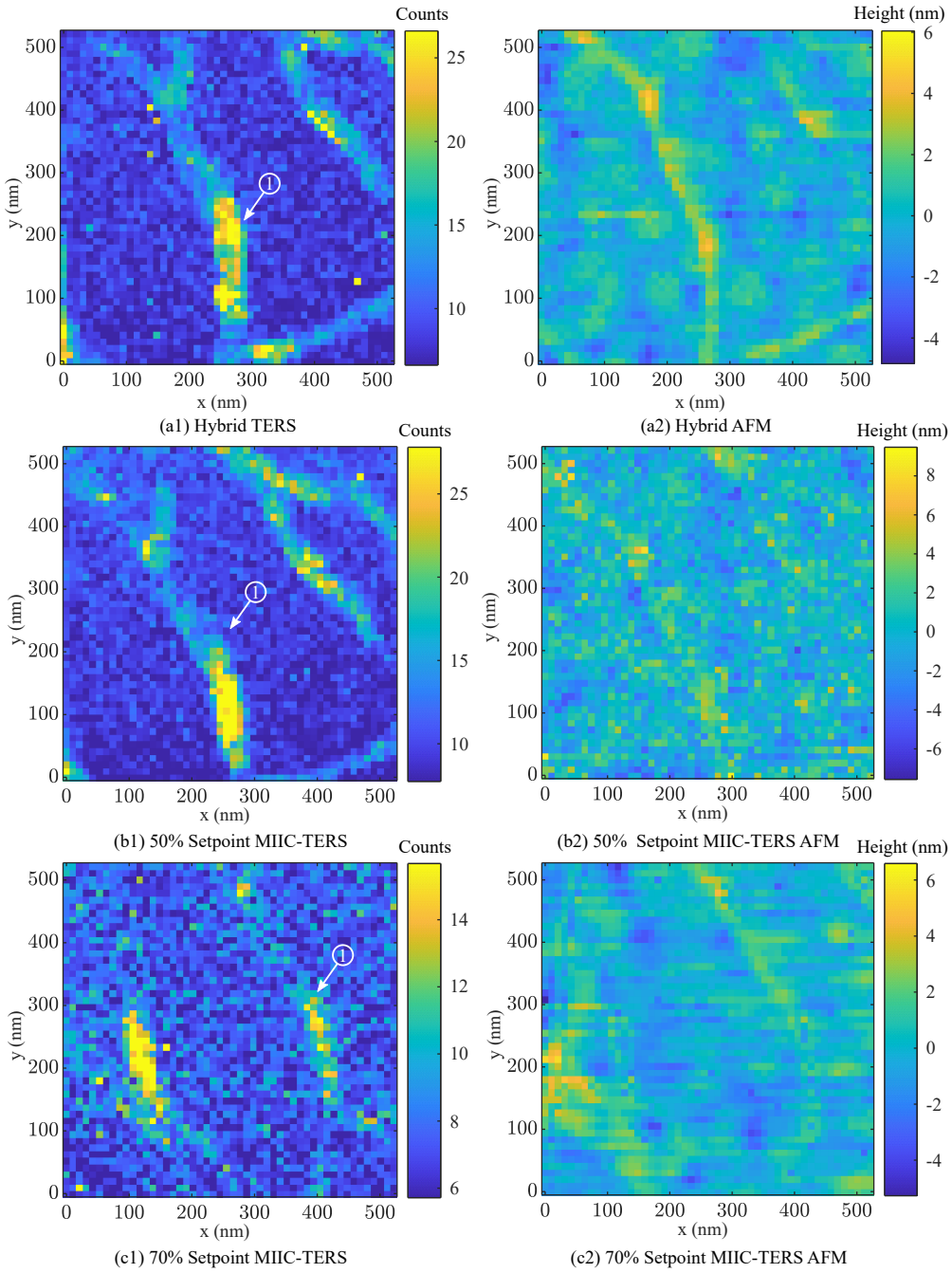

Figure 7.6: A comparison of TERS imaging modes acquired using a 150 nm long gold nanocone probe on a sample of CNT bundles on a gold substrate with 638 nm excitation. MIIC-TERS was performed with a 10% duty cycle. All maps were acquired with an average laser power of 1 mW. D-band TERS maps are shown for (a1) hybrid mode, (b1) 50% setpoint MIIC TERS and (c1) 70% MIIC-TERS respectively. The bend of the CNT bundle has been labelled in each TERS map. The associated AFM height maps are shown in (a2), (b2), (c2). The hybrid mode provides the best AFM height map with high contrast of the CNT bundle. The 50% setpoint MIIC-TERS map provides similar image quality to the hybrid mode. The 70% setpoint MIIC-TERS map displays poor contrast due to the small contact time.

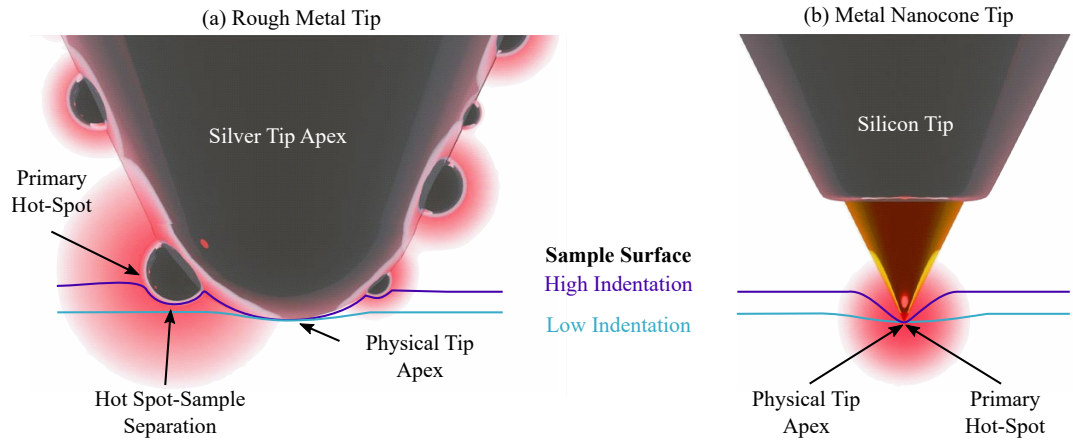

Figure 7.7: The effect of an offset between the primary hot spot and physical tip-apex as a function of sample indentation for (a) rough metal and (b) gold nanocone probes. For the grainy probe, A low indentation results in a separation between the hot spot and sample surface. A high sample indentation is necessary to reduce this separation and maximise the Raman enhancement. The nanocone geometry does not require high indentation to maximise the Raman enhancement.

in Figure 7.8(b). The contrast decreases as the duty cycle is increased. This is expected as the mean enhancement at the sample while the laser is on decreases as the duty cycle increases. In other words, there is increased far-field contribution as the duty cycle increases. The contrast increases with a decreased setpoint. This is because the minimum tip-sample separation is reduced. Furthermore, the tip-sample contact time is increased resulting in a relatively constant contrast from 10-50% duty cycles with the 35% setpoint measurements. An increased tip-sample force increases the chance of tip-contamination or sample damage. Thus, the setpoint should be lowered until acceptable Raman contrast is achieved. This will minimise tip contamination.

7.4 Conclusion

In this chapter, the MIIC-TERS mode is experimentally compared to hybrid contact mode. MIIC-TERS is found to have an equivalent optical performance to the hybrid mode with a gold nanocone probe, provided the setpoint is appropriately low. MIIC-TERS provided inferior optical performance to the hybrid mode when using a grainy silver probe. This is likely due to an offset between the hot spot and the physical tip apex, which requires increased sample indentation to minimise the distance between the hot spot and the surface. MIIC-TERS contrast was found to be inversely proportional to the laser duty cycle. Furthermore, low setpoints increase the optical contrast but may increase the likelihood of tip contamination and sample damage.

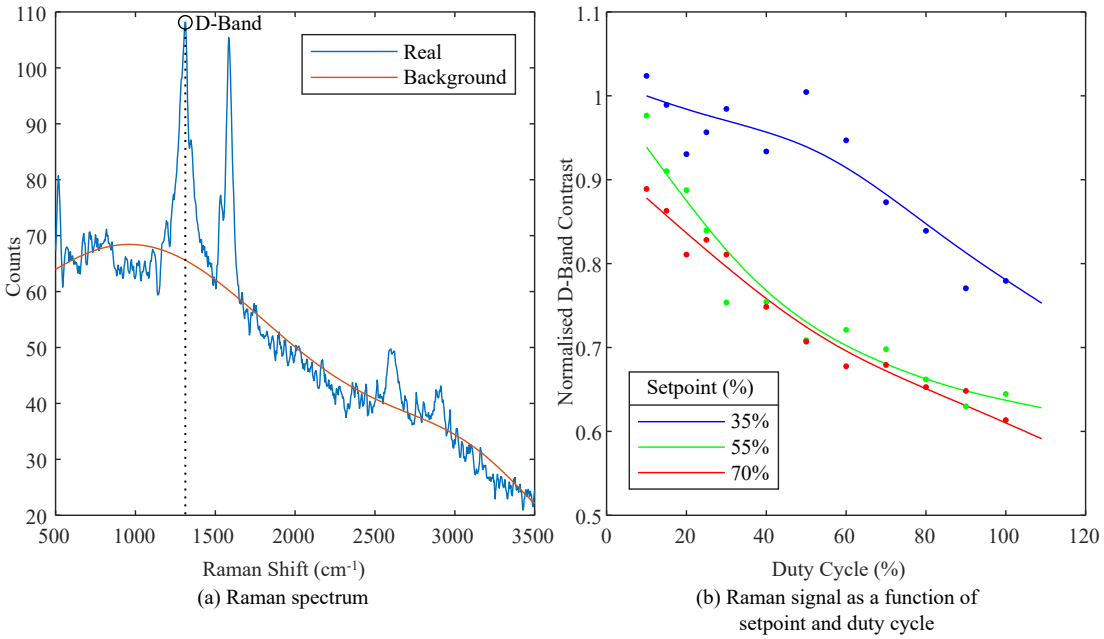

Figure 7.8: MIIC-TERS performance. (a) An example TERS spectrum of a nanotube. The contrast is given by the D-band peak height divided by the background at the same Raman shift. (b) The D-band contrast versus laser duty cycle for different AFM setpoints.

7.5 Future Work

The experimental work in this chapter discusses the performance of MIIC-TERS as a function of laser duty cycle and AFM setpoint on a sample of SWCNTs on gold. Future work should investigate the practical imaging performance on a large range of samples. It remains unclear why the nanocone probe provides poor AFM maps when acquired with the MIIC-TERS mode. The mechanism behind this issue requires further investigation.

Chapter 8

Conclusions and Future Work

The three main contributions of this thesis are the design and fabrication of improved TERS probes, the development of a new method for quantifying TERS probe performance, and the implementation and analysis of the MIIC-TERS imaging mode. These contributions are summarised in the following sections

8.1 Gold Nanocone TERS Probe

Commercially available TERS probes consist of a grainy metal layer on a silicon AFM probe. The metal is typically silver as it provides superior enhancement. However, these probes exhibit several downsides, namely unreliable TERS performance, low spatial resolution, poor lifetimes and an offset between AFM and TERS maps. In Chapter 2, boundary element method simulations were used to identify the smooth nanocone as a suitable geometry for an improved TERS probe. The length of the nanocone can be altered to tune the plasmon resonance wavelength independently of the spot size at the tip apex. Furthermore, the physical tip apex is collocated with the enhancement hot spot, which should result in collocated AFM and TERS maps. In Chapter 3, numerical models were developed for the electric field enhancement and resonance wavelength of silver and gold nanocones. It was found that gold nanocones could be designed to provide sufficient enhancement while exhibiting superior chemical stability compared to silver probes. In Chapter 6, a gold nanocone probe was fabricated using the developed models, and the TERS imaging performance was shown to be superior to commercially available probes. The nanocone probe exhibited comparable optical contrast while providing superior optical resolution and collocation of AFM and TERS maps.

8.1.1 Summary of Contributions

1. Modelling of electric field enhancement and resonance wavelength for silver and gold nanocones

2. Design of a gold nanocone TERS probe that provides superior imaging performance compared to commercially available probes

3. Demonstration of the first TERS images using a gold nanocone probe

8.1.2 Future Work

The numerical models presented in Chapter 3 predict the electric field enhancement and resonance wavelength of nanocone probes, and were used to optimise the geometry of the gold nanocone probe. To verify these models, a statistical analysis of gold nanocones with varying lengths, half angles and tip radius is required.

8.2 Quantifying TERS Imaging Performance

Chapter 5 presents a method for characterisation of TERS imaging performance. SWCNTs were used as 1D scattering objects, allowing the PSF to be measured. The PSF was used to calculate two metrics that characterise imaging performance, namely optical contrast, which quantifies the near-field to far-field contributions and spot diameter, which quantifies the spatial resolution. The method was successfully used to characterise the imaging performance of several commercially available probes and compare them to the gold nanocone probe.

8.2.1 Summary of Contributions

1. Development of a new method for characterising TERS imaging performance using SWCNTs

2. Experimental comparison of the imaging performance of commercially available probes and a gold nanocone probe

8.2.2 Future Work

The method presented has several limitations. Most notably, calculating the PSF assumes a symmetric electric field distribution in the sample plane. This assumption could be removed and the full 2D PSF recovered by collecting the TERS cross-sections over two orthogonal SWCNTs. A de-convolution would then be performed to recover the 2D PSF. Furthermore, the presented method is valid when the SWCNT diameter is smaller than the spot diameter, which was true for the work presented in this thesis. However, if sub-nanometre resolutions are investigated under high-vacuum then a new method will be required.

8.3 MIIC-TERS

The MIIC-TERS imaging mode was introduced in Chapter 7 using a combination of mechanical and optical simulations. It was shown that MIIC-TERS could provide similar Raman signal-to-noise ratios as contact mode while reducing the chance of sample damage, tip damage or tip contamination. MIIC-TERS was experimentally demonstrated using a grainy silver probe and a gold nanocone probe. Compared to contact and hybrid mode imaging, MIIC-TERS was shown to provide a similar Raman signal-to-noise ratio but with reduced sample damage and less probe contamination. The gold nanocones were found to provide higher optical contrast than grainy silver probes. It was also demonstrated that lower laser duty cycles increased the optical contrast by reducing the contribution of far-field Raman scatter.

8.3.1 Summary of Contributions

1. Implementation of the MIIC-TERS imaging mode and demonstration using grainy silver and gold nanocone probes
2. Analysis of the imaging performance as a function of laser duty cycle and amplitude setpoint

8.3.2 Future Work

A more robust analysis of the effects of laser duty cycle and amplitude setpoint are required, especially on samples of varying stiffness, which may influence the recommended parameters for optimal TERS image quality. Further experiments should be conducted to verify the hypothesis that a hot spot-tip apex separation is responsible for the poor performance of grainy silver probes.

Appendix A

Boundary Element Method

A.1 Boundary Element Method Derivation

Beginning with Eq. B.1.1, B.1.2, B.1.3 and B.1.4, the vector magnetic $\mathbf{A}$, and the scalar magnetic ϕ fields are introduced in

$$\mathbf{E} = ik\mathbf{A} - \nabla\phi \tag{A.1.1}$$

and

$$\mathbf{B} = \nabla \times \mathbf{A} \tag{A.1.2}$$

There is redundancy in Eq. A.1.2 as curl free components are ignored. To remove this the Lorenz gauge condition is used:

$$\nabla \cdot \mathbf{A} = ik\epsilon\phi \tag{A.1.3}$$

Using $\mathbf{A}$ and ϕ, Gauss' and Amperes Laws are transformed to:

$$(\nabla^2 + k^2\epsilon\mu)\phi = -4\pi(\frac{\rho}{\epsilon} + \sigma_s) \tag{A.1.4}$$

$$(\nabla^2 + k^2\epsilon\mu)\mathbf{A} = -\frac{4\pi}{c}(\mu\mathbf{j} + \mathbf{m}) \tag{A.1.5}$$

Where:

$$\sigma_s = \frac{1}{4\pi}\mathbf{D} \cdot \nabla\frac{1}{\epsilon} \tag{A.1.6}$$

$$\mathbf{m} = -\frac{1}{4\pi}(i\omega\phi\nabla(\epsilon\mu)) + c\mathbf{H} \times \nabla\mu) \tag{A.1.7}$$

σ_s and $\mathbf{m}$ are only nonzero when the gradient of ϵ is nonzero which occurs at the boundary separating two distinct dielectric functions.

Eq.s A.1.4 and A.1.5 have the following general solutions:

$$\phi(\mathbf{r}) = \frac{1}{\epsilon_j(\omega)}\int d\mathbf{r'}G_j(|\mathbf{r} - \mathbf{r'}|)\rho(\mathbf{r'}) + \int_{S_j} d\mathbf{s}G_j(|\mathbf{r} - \mathbf{s}|)\sigma_j(\mathbf{s}) \tag{A.1.8}$$

$$\mathbf{A}(\mathbf{r}) = \frac{\mu_j(\omega)}{c} \int d\mathbf{r'} G_j(|\mathbf{r} - \mathbf{r'}|)\mathbf{j}(\mathbf{r'}) + \int_{S_j} d\mathbf{s} G_j(|\mathbf{r} - \mathbf{s}|)\mathbf{h}_j(\mathbf{s}) \tag{A.1.9}$$

Where S_j is the boundary of medium j, and:

$$G_j(r) = \frac{e^{ik_j r}}{r} \tag{A.1.10}$$

which is the green function of the following wave equation:

$$(\nabla^2 + k_j^2)G_j(r) = -4\pi\delta(\mathbf{r}) \tag{A.1.11}$$

The tangential electric field and normal magnetic induction at the boundary must be continuous, and so the general solutions for ϕ and $\mathbf{A}$ must have the same value on either side of the interface. This leads to the following continuity equations:

$$G_1\sigma_1 - G_2\sigma_2 = \phi_2^e - \phi_1^e \tag{A.1.12}$$

$$G_1\mathbf{h}_1 - G2\mathbf{h}_2 = \mathbf{A}_2^e - \mathbf{A}_1^e \tag{A.1.13}$$

Where:

$$\phi_j^e(s) = \frac{1}{\epsilon_j(\omega)} \int d\mathbf{r'} G_j(|s - \mathbf{r'}|)\rho(\mathbf{r'}) \tag{A.1.14}$$

$$\mathbf{A}_j^e(s) = \frac{\mu_j(\omega)}{c} \int d\mathbf{r'} G_j(|s - \mathbf{r'}|)\mathbf{j}(\mathbf{r'}) \tag{A.1.15}$$

And these are the scalar and vector potentials that would induced at the interface, provided the entire space was filled with medium j, due to external charges.

In the nonmagnetic case, when $\mu_r = 0$, the continuity of the tangential magnetic field and the vector potential means the tangential and normal derivatives of the vector potential must be continuous. Along with the Lorenz gauge it follows that $(\mathbf{n}_s \cdot \nabla)\mathbf{A} - i\mathbf{n}_s k\epsilon\mu\phi$ is also continuous. Substituting Eq.s A.1.8 and A.1.9 into this, the following is obtained:

$$H_1\mathbf{h}_1 - H_2\mathbf{h}_2 - ik\mathbf{n}_s(G_1\epsilon_1\mu_1\sigma_1 - G_2\epsilon_2\mu_2\sigma_2) = \vec{\alpha} \tag{A.1.16}$$

where:

$$\vec{\alpha} = (\mathbf{n}_2 \cdot \nabla_s)(\mathbf{A}_2^e - \mathbf{A}_1^e) + ik\mathbf{n}_s(\epsilon_1\mu_1\phi_1^2 - \epsilon_2\mu_2\phi_2^e) \tag{A.1.17}$$

and H_j is the normal derivative of the Green function G_j, taken from both sides of the interface. This is for nonmagnetic materials only.

For magnetic materials, an adjustment must be made to the tangential part, eventually yielding the following:

$$H_1\epsilon_1\sigma_1 - H_2\epsilon_2\sigma_2 - ik\mathbf{n}_s \cdot (G_1\epsilon_1\mathbf{h}_1 - G_2\epsilon_2\mathbf{h}_2) = D^e \tag{A.1.18}$$

where:

$$D^e = \mathbf{n}_s \cdot (\epsilon_1(ik\mathbf{A}_1^e - \nabla_s \phi_1^e) - \epsilon_2(ik\mathbf{A}_2^e - \nabla_s \phi_2^e)) \tag{A.1.19}$$

which is the difference in normal displacement at the interface if the entire space was filled with either medium, j.

When the surface and current charges σ_j and $\mathbf{h}_j$ are calculated self consistently from equations A.1.12, A.1.13, A.1.16, A.1.19, then equations A.1.4 and A.1.5 give solutions to Maxwell's equations which satisfy the boundary conditions and go to zero at infinity [91], [92].

Appendix B

Near-field Derivations

B.1 Maxwell's Equations

Maxwell's equations along with the Lorentz force law, form the theoretical basis of classical electrodynamics. They will be used throughout the following derivations. In differential form they are as follows:

$$\nabla \cdot \mathbf{E} = \frac{1}{\epsilon_0}\rho, \tag{B.1.1}$$

$$\nabla \cdot \mathbf{B} = 0, \tag{B.1.2}$$

$$\nabla \times \mathbf{E} = -\frac{\partial \mathbf{B}}{\partial t}, \tag{B.1.3}$$

$$\nabla \times \mathbf{B} = \mu_0 \mathbf{J} + \mu_0 \epsilon_0 \frac{\partial \mathbf{E}}{\partial t}, \tag{B.1.4}$$

with electric field $\mathbf{E}$, magnetic field $\mathbf{B}$, current density $\mathbf{J}$, permittivity of free space ϵ_0, permeability of free space μ_0, charge density ρ and the gradient operator ∇.

The Lorentz force gives the force on a charged particle in a magnetic and electric field:

$$\mathbf{F} = q(\mathbf{E} + \mathbf{V} \times \mathbf{B}), \tag{B.1.5}$$

with the velocity of the charge $\mathbf{V}$. Additionally there are the two constitutive relations for the displacement field $\mathbf{D}$ and the magnetic field strength $\mathbf{H}$, which describe the fields in materials:

$$\mathbf{D} = \epsilon \mathbf{E} + \mathbf{P}, \tag{B.1.6}$$

$$\mathbf{H} = \frac{1}{\mu}\mathbf{B} - \mathbf{M}, \tag{B.1.7}$$

where ϵ and μ are the permittivity and permeability of the material and $\mathbf{P}$ and $\mathbf{M}$ are the

polarisation and magnetic response.

B.2 Near-field from an Aperture

Consider a two dimensional, perfect conductor in the x-y plane with a small circular aperture of diameter a as shown in Figure 1.6. The uncertainty principle in the x-y plane, with the right hand side set to 1 for simplicity is

$$\Delta(x,y)\Delta k_{x,y} \geq 1, \tag{B.2.1}$$

where k is the wavenumber: $k = 2\pi/\lambda$. As $\Delta(x,y)$ is confined to the aperture

$$\Delta k_{x,y} \geq a^{-1} \tag{B.2.2}$$

For a sub-wavelength aperture

$$\lambda = \frac{2\pi}{k} > a. \tag{B.2.3}$$

Hence,

$$\frac{k}{2\pi} < a^{-1}, \tag{B.2.4}$$

and

$$\Delta k_{x,y} \geq a^{-1} > k. \tag{B.2.5}$$

Applying this result to the dispersion relation

$$k^2 = k_x^2 + k_y^2 + k_z^2 = \frac{\omega^2}{c^2}\epsilon. \tag{B.2.6}$$

implies k_z^2 may be either positive or negative, so there become two distinct possibilities as the planewave passes through the aperture. For $k_z > 0$

$$A(z) = A_0 e^{ik_z z}. \tag{B.2.7}$$

This is the radiative wave. Alternatively, for $k_z > 0$

$$A(z) = A_0 e^{-|k_z|z} \tag{B.2.8}$$

which will decay exponentially from the aperture, and so is termed the evanescent wave.

At large distances from an aperture, the radioactive wave will dominate. This typically occurs beyond two wavelengths and is known as the far-field. Within one wavelength, the evanescent wave contributes significantly. This region is known as the near-field [41]. The relationship between the electric and magnetic fields are more complex in the near field, simplifying in the far-field where they become orthogonal to one another and the direction of propagation [42].

The near field contains an increased power density, which decays exponentially away from an aperture. This can be used in near-field applications to circumvent the diffraction limit. It is

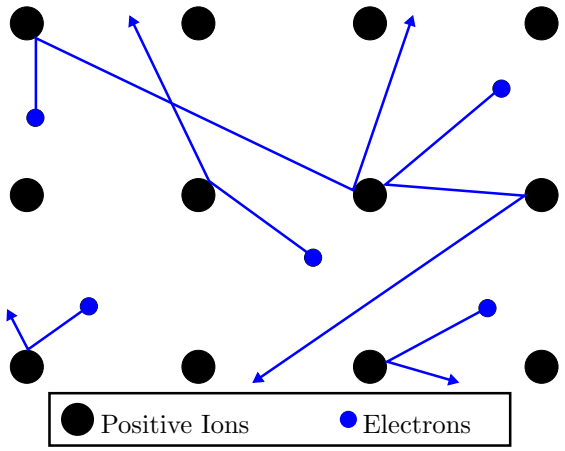

Figure B.1: Drude model consisting of a fixed lattice of positive ions • and non-interacting electrons • scattering off lattice points, arrows indicate direction of travel →.

used in imaging techniques such as TERS, where the localised field from a metallic tip improves the Raman signal by several orders of magnitude [15].

B.3 Bulk Plasmons - Unconstrained

The Drude model gives an approximation for the dielectric function of a material. The model treats conduction electrons as a non-interacting gas, which relax via collisions with the lattice, whilst the ions are stationary due to their relatively high mass, ignoring any quantum effects. This model is illustrated in Figure B.3.1. The equation of motion for the Drude model is

$$m\frac{d^2\mathbf{x}}{dt^2} = -\frac{m\gamma d\mathbf{x}}{dt} - q\mathbf{E}_{tot}(t), \tag{B.3.1}$$

with electron mass and charge m and q respectively, the decay constant τ which accounts for the average time of scattering events with γ being the inverse of this ($\gamma = 1/\tau$), and the total electric field, $\mathbf{E}_{tot}$, being the sum of internal $\mathbf{E}_{int}$ and external $\mathbf{E}_{ext}$ fields [40]).

For an oscillating external field of frequency ω, the total electric field will oscillate at the same frequency. If time harmonic excitation is assumed, i.e. $\mathbf{E}(t) = E_0 e^{-i\omega t}$, then a particular solution is $\mathbf{x}(t) = \mathbf{x}_0 e^{-i\omega t}$, with $\mathbf{x}_0$ incorporating any phase shifts via

$$\mathbf{x} = \frac{e}{m(\omega^2 + i\gamma\omega)}\mathbf{E}(t). \tag{B.3.2}$$

Using Eq. B.1.6 and the fact that the polarisation is given by

$$P = -\frac{ne^2}{m(\omega^2 + i\gamma\omega)}, \tag{B.3.3}$$

where n is the number density of electrons, then

$$\mathbf{D} = \epsilon_0 \mathbf{E} - \frac{ne^2\mathbf{E}}{m(\omega^2 + i\omega m)} = \epsilon_0(1 - \frac{\omega_p^2}{\omega^2 + i\gamma\omega})\mathbf{E}, \tag{B.3.4}$$

where ω_p is the plasma frequency

$$\omega_p^2 = \frac{ne^2}{\epsilon_0 m}. \tag{B.3.5}$$

Furthermore, $\epsilon = \epsilon_0\epsilon_r$, where ϵ_0 and ϵ_r are the free space and relative permittivities respectively. And so finally, the permittivity of the free electron gas is

$$\epsilon(\omega) = 1 - \frac{\omega_p^2}{\omega^2 + i\gamma\omega}, \tag{B.3.6}$$

with the real and imaginary components, $\epsilon(\omega) = \epsilon_R(\omega) + i\epsilon_I(\omega)$, given by

$$\epsilon_R = 1 - \frac{\omega_p^2\tau^2}{1 + \omega^2\tau^2} \tag{B.3.7}$$

$$\epsilon_I = \frac{\omega_p^2\tau}{\omega(1 + \omega^2\tau^2)}. \tag{B.3.8}$$

ϵ_I gives the loss of the material, which needs to be minimal for a strong plasmon resonance. For frequencies close to ω_p, ϵ_I will be minimised (Eq. B.3.8), hence the plasmon resonance occurs at the plasma frequency. At this point $\epsilon_1 \approx 0$. This is for an ideal non-interacting electron gas not a solid particle, and plasmon resonance will not always occur when $\epsilon_1 \approx 0$. Instead it is geometry dependent. Interestingly, bulk plasmons are longitudinal compression waves (similar to sound), and so light waves, being transverse, cannot couple directly into them. Some sort of surface defect is needed.

Deviations from the plasma frequency will lead to considerable damping. In the low frequency limit, the electric field decays exponentially into the material as

$$e^{-z/\delta},$$

where δ is the depth at which the current density falls to 1/e, known as the skin depth. In effect, the surface is screening the bulk material from the external field. In the high-frequency limit $\epsilon_1 \approx 1$ and so the material is effectively transparent to the external field [39].

B.4 Surface Plasmons - One Dimensional Constraint

Consider a bulk material terminated at a surface as in Figure B.2, with a field propagating in $\hat{x}$. The normal component of $\mathbf{D}$ must be continuous across the boundary and so

$$\epsilon_1 \mathbf{E}_{1z} = \epsilon_2 \mathbf{E}_{2z}. \tag{B.4.1}$$

Furthermore, for a transverse wave, $\mathbf{E}_x = 0$ and $k_z = 0$, so

$$k_{ix}\mathbf{E}_{ix} + k_{iz}\mathbf{E}_{iz} = 0, \tag{B.4.2}$$

where i is the material index (i.e. 1 or 2). The total dispersion in a material is given by

$$k_{ix}^2 + k_{iy}^2 + k_{iz}^2 = \frac{\epsilon_i \omega}{c^2}. \tag{B.4.3}$$

From Eqs. B.4.1, B.4.2 and B.4.3, the following dispersion relation is found

$$k_x^2 = \frac{\epsilon_1 \epsilon_2 \omega^2}{(\epsilon_1 + \epsilon_2)c^2}. \tag{B.4.4}$$

Consider a bulk metal (region 2) terminated by a dielectric (region 1). For the dielectric assume free space, $\epsilon_1 = 1$. For the metal, using the Drude model and assuming zero damping ($\gamma \to 0$), then $\epsilon_2 = 1 - \omega_p^2/\omega^2$. Hence

$$k_x^2 = (\frac{\omega^2 - \omega_p^2}{\omega^2 - \omega_s^2})\frac{\omega^2}{2c}, \tag{B.4.5}$$

where $\omega_s \equiv \omega_p/\sqrt{2}$ is the plasma frequency. For a propagating wave k_x must be positive and so $k_x^2 > 0$. This is satisfied only if:

1. $\omega \geq \omega_p$ ($\mathrm{k_{1z}}$ and $\mathrm{k_{2z}}$ both real) , or
2. $\omega \leq \omega_s$ ($\mathrm{k_{1z}}$ and $\mathrm{k_{2z}}$ both imaginary)

In the first case, there is propagation in both x and y. Incident waves are transmitted into the metal without reflection, with both materials acting as dielectrics. These are known as Brewster modes.

In the second case, the imaginary k_z in both materials means the fields will decay exponentially for $|z| > 0$, meaning the wave will be strongly localised to the surface of the metal. As k_x increases $k_z^2 \to \infty$ so the fields and charge densities become fully confined to the surface, i.e. surface plasmons. Eq. B.4.5 is plotted in Figure B.3 and shows that direct coupling into the surface plasmon is not possible as k_x is greater for the surface plasmon than in free space, giving a wavenumber mismatch. This can be overcome by using a prism or grating. Alternatively, and more importantly here, defects from a perfect planar interface can allow light to directly couple into plasmons.

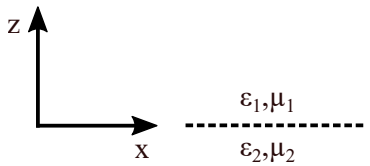

Figure B.2: Termination of bulk material (ϵ_1, μ_1) at an interface with another material (ϵ_2, μ_2).

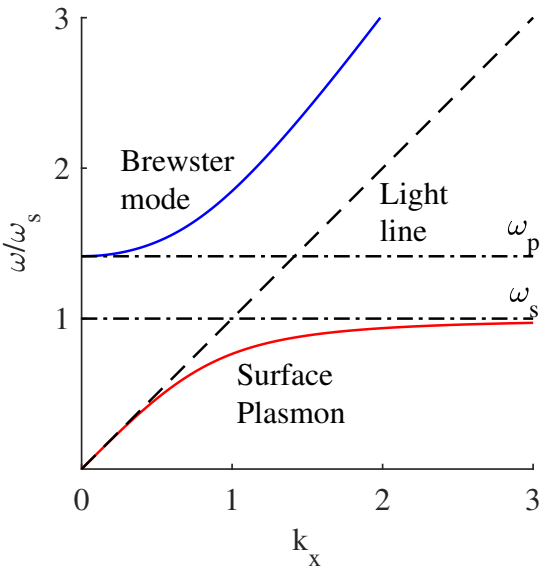

Figure B.3: Modes of propagation for a Drude metal terminated by a dielectric. Produced using Eq. B.4.5 with $c = 1$ and $\omega_s = 1$. k_x is greater for the surface plasmon than the light line, demonstrating that light cannot directly couple into these plasmon modes.

Appendix C

Unsuccessful TERS Probe Fabrication

C.1 First Attempt

This subsection details attempts made to fabricate nanocap TERS probes as illustrated in Figure 6.1(b) according to the dimensions detailed in Table 3.1 starting with an excitation wavelength of 785 nm and a cone angle of 20^o and a cone length of 220 nm.

For the first attempt, silicon AFM probes (AppNano ACCESS-FM), shown in Figure C.1(a-b), were coated with a thin layer of gold. The geometry of the AFM tips makes coating all sides of the pyramid tip with a uniform coating of gold in one static step impossible. The two-step process illustrated in Figure C.2(a-b) was used to get a more uniform gold coverage. With the thermal evaporation beam going top to bottom in the vertical axis, the top faces of the tip which are perpendicular to the beam are coated efficiently.

Figure C.1(c-d) shows images of a tip after being coated with approximately 30 nm of gold as measured using a quartz crystal monitor. energy-dispersive x-ray spectroscopy element analysis results are given in Table C.1. The energy-dispersive x-ray spectroscopy results give the element composition of the target area with a penetration depth that is typically on the order of 1μm. Hence, the results in the table extend beyond the surface layer. Figure C.1(c) shows that islands or grains have been formed during thermal evaporation. The composition of these islands is confirmed as predominantly gold as point 5 shows a mass composition of 92.7% gold. In locations where islands are not formed, for example, areas 8 and 9, there is still a gold layer of 68.2% and 57.3% by mass respectively. This indicates that a fairly uniform gold layer has been deposited on the entire tip with gold islands forming randomly on the tip surface. The formation of the islands indicates that thermal evaporation is not suitable for creating smooth metal coatings on silicon tips.

A Helios G4 PFIB UXe DualBeam system with a xenon ion beam source was used in an attempt to mill the gold-coated tips into nanocaps of the required 220 nm length. The milling method used here is illustrated in Figure C.3, which removes only the surface gold layer and

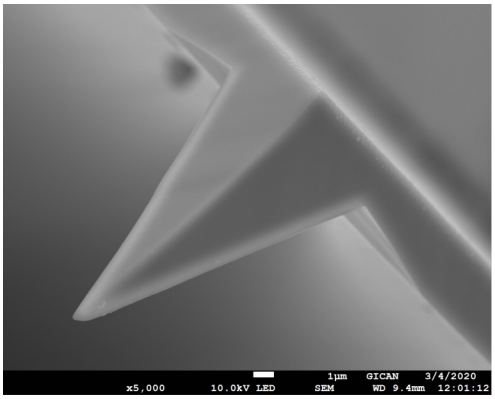

(a) Uncoated

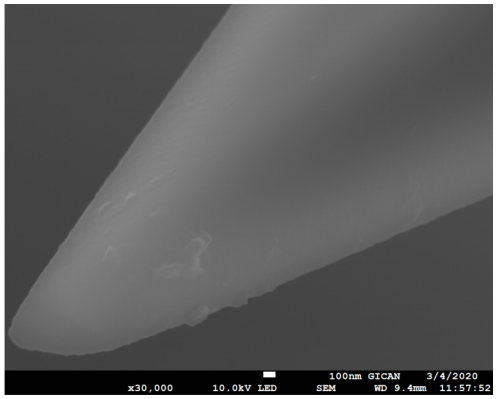

(b) Uncoated zoomed

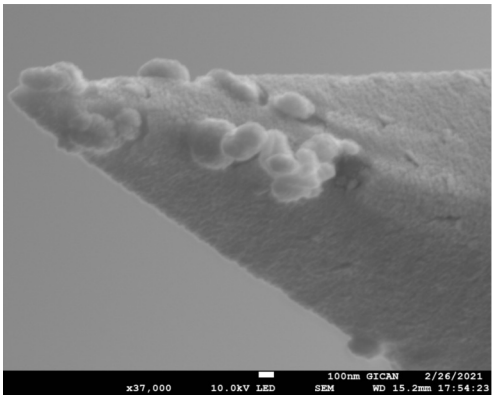

(c) Tip after gold thermal evaporation

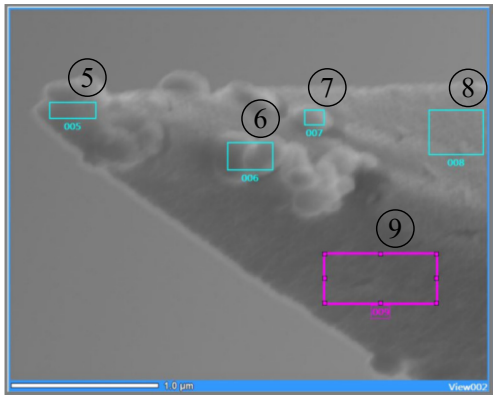

(d) Points used for energy dispersive x-ray spectroscopy of gold coated tip

Figure C.1: Scanning electron microscope images of silicon access probes (a-b) un-coated and (c) coated with approximately 30 nm of gold. (d) Shows the points used for energy-dispersive x-ray spectroscopy element analysis. The grain structures visible were confirmed to be gold nanoparticles using energy-dispersive x-ray spectroscopy.

will be referred to as the surface-milling method. This method has the advantage that drift due to charging of the tip can be mitigated by using an exposure width greater than the tip. The downside is that visual contrast must be relied upon to determine when the gold layer has been successfully removed. Figure C.4(a) shows the exposure profile in the FIB software, marked by the rectangle. The desired gold cap length is left unmilled. The blurry edges and lack of zoom were limitations inherent to the system used and resulted in poor control of the resulting structure. The precision required to produce nanocaps of specific lengths was not possible using this system. Furthermore, it was observed that the gold peeled off in clumps, showing that the gold weakly adhered to the silicon layer. This indicates that an adhesion layer will be required.

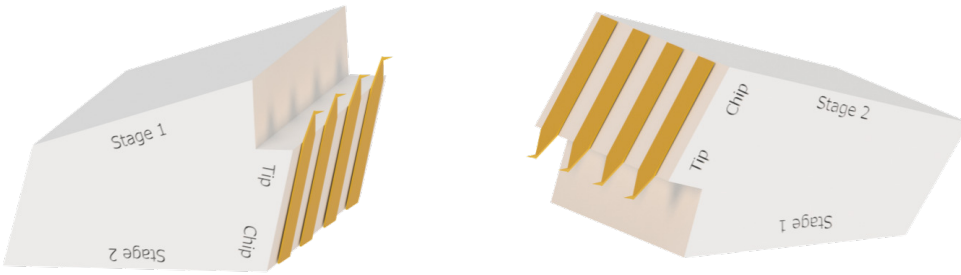

(a) Step 1 (b) Step 2

Figure C.2: Geometry for metal deposition on access AFM tips. The evaporation beam is coming down vertically. Stage 1 and stage 2 allow for a uniform coating of gold on the tips.

Table C.1: Element analysis of gold-coated silicon access tip. The points given correspond to those given in the scanning electron microscope image shown in Figure C.1(d).

Point	Gold (Mass %)	Silicon (Mass %)	Carbon (Mass %)	Oxygen (Mass %)
5	92.7	3.2	2.4	1.7
8	68.2	23.3	4.9	3.6
9	57.3	38.4	1.7	2.7

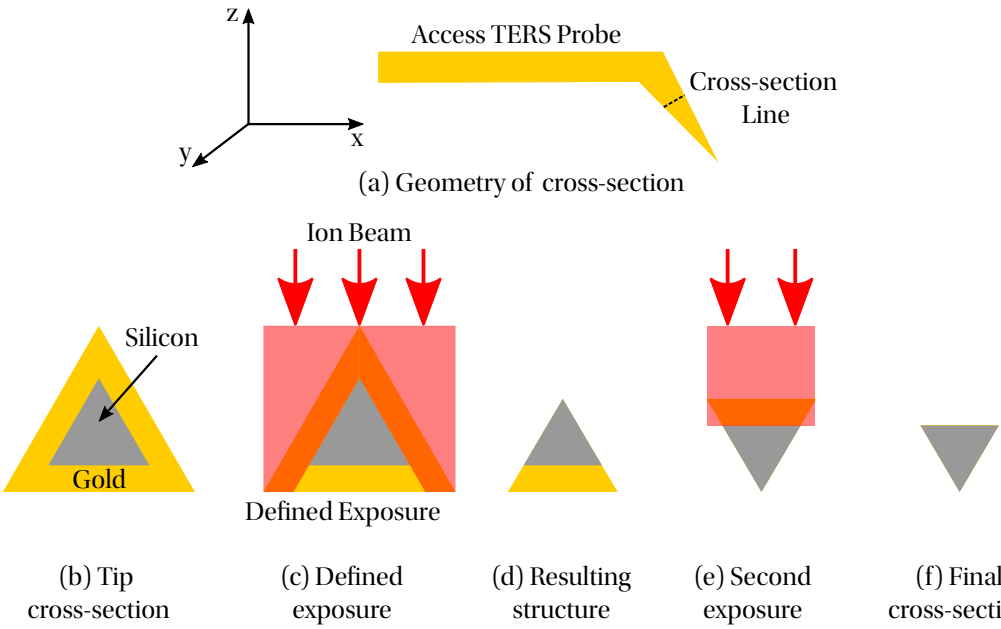

(a) Geometry of cross-section

(b) Tip cross-section (c) Defined exposure (d) Resulting structure (e) Second exposure (f) Final cross-section

Figure C.3: Illustration of the first ion beam milling procedure to form a gold nanocap probe as shown in Figure 6.1(b). This method consists of removing only the gold layer in the exposure area. (b) Shows the cross-section geometry of a gold-coated TERS probe. (b) Shows the initial cross-section consisting of a silicon base with a gold coating. (c) Shows the first ion beam exposure where the milling is terminated once the gold layer is removed. (d) Shows the resulting structure after the first exposure. Following this, the structure is rotated 90^o. (e) Shows the second exposure and (f) the final cross-section which is free of gold and non-conductive.

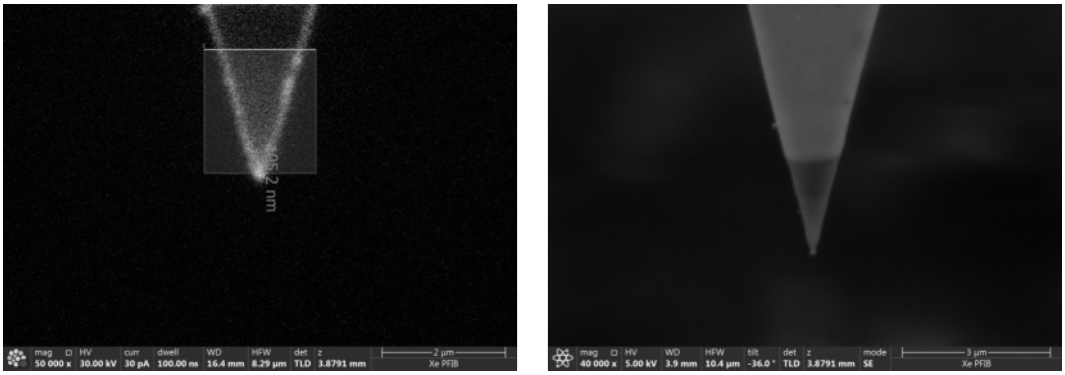

(a) Focused ion beam exposure profile (b) Post focused FIB milled gold tip

Figure C.4: Focused ion beam images of the first attempt at fabricating gold nanocap tips as illustrated in Figure 6.1(b) using a Helios G4 PFIB UXe DualBeam system with a xenon ion beam source and the surface-milling procedure outlined in Figure C.3. (a) Shows the definition of the ion beam exposure profile. The low resolution of the focused ion beam system made defining the nanocap dimensions accurately impossible. (b) Shows the resulting structure. It was assumed that the contrast seen towards the tip apex is due to the silicon layer being revealed.

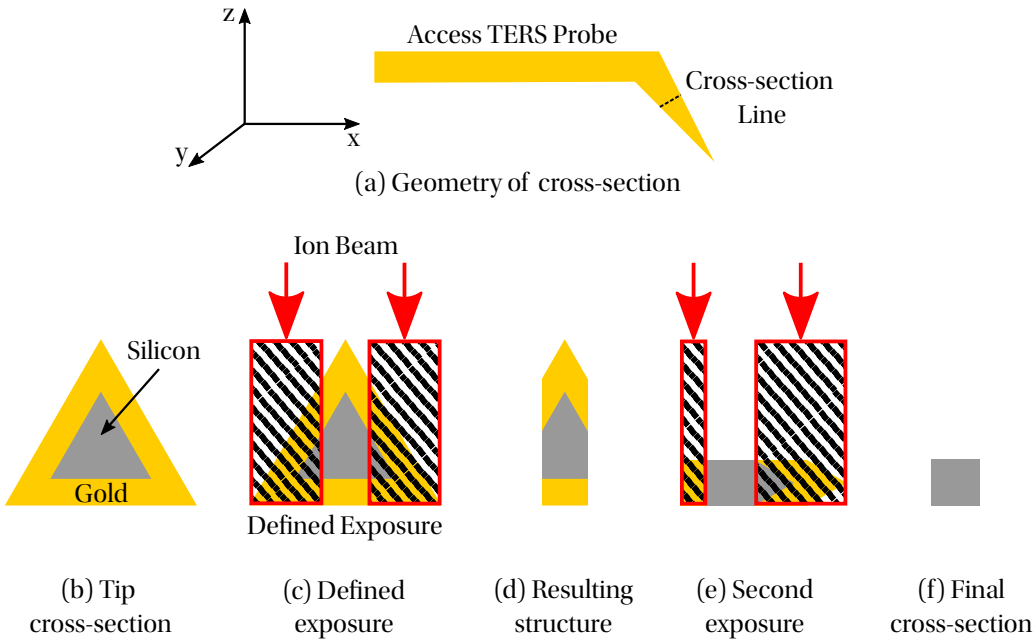

Figure C.5: Illustration of the second ion beam milling procedure to form a gold nanocap probe as shown in Figure 6.1(b). This method consists of removing all material in the exposure area. (a) Shows the cross-section geometry of a gold-coated TERS probe. (a) Shows the initial cross-section consisting of a silicon base with a gold coating. (b) Shows the first ion beam exposure where the rectangular areas are fully removed. (c) Shows the resulting structure after the first exposure. Following this, the structure is rotated 90^o. (e) Shows the second exposure and (f) the final cross-section which is free of gold and non-conductive.

C.2 Second Attempt

An alternative ion beam milling method is illustrated in Figure C.5. With this milling methodology, all material within the exposure area is removed. With this method, the gold layer can be removed without relying on visual contrast in the scanning electron microscope image to indicate that the silicon layer has been reached. This method was used for the attempt at fabricating a gold nanocap that is described in this section.

A commercially available gold-coated access AFM probe was placed into a ZEISS Crossbeam 550 with a gallium ion source. An FIB image of the AFM tip is shown in Figure C.6(a). The exposure pattern is marked as F3 and F4. F6 is a margin of error area that was calibrated to the focused ion beam width as determined by milling a small hole in the cantilever. F1 is the desired section of the probe to remain untouched and form the nanocap.

Figure C.6(b) shows the structure that resulted from the ion beam exposure. During the milling procedure, the tip has become charged, causing drift in the ion beam position. This resulted in the tip being cut in an undesired manner and no gold was left at the tip apex. This procedure was attempted with several probes but no nanocaps were successfully fabricated. This highlights the disadvantage of the through-milling method in that it is sensitive to drift.

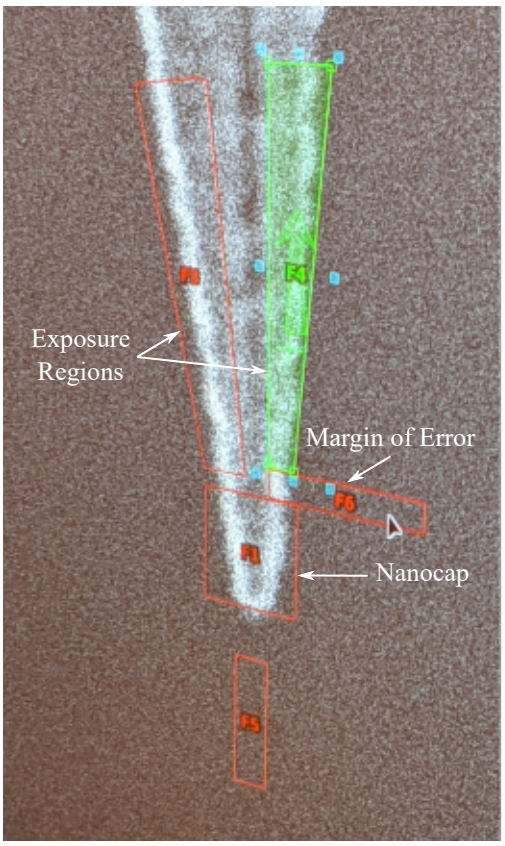

(a) Focused ion beam exposure profile

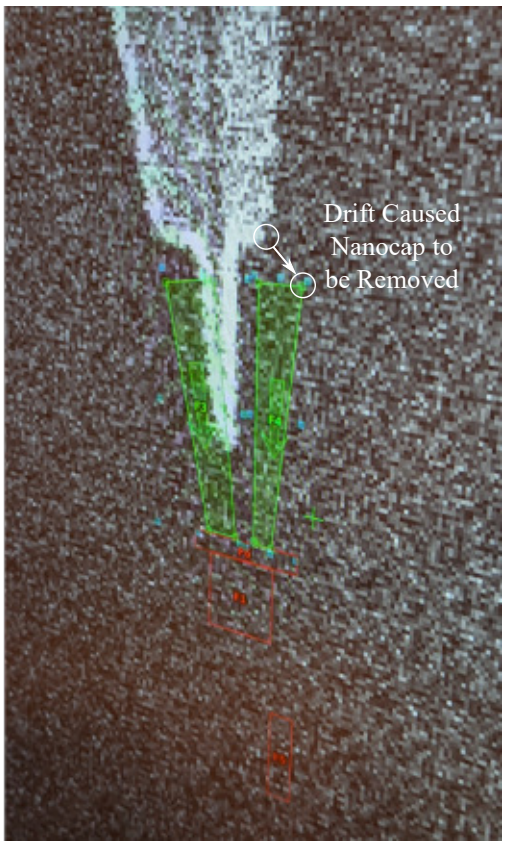

(b) Post focused ion beam milling of gold -coated tip

Figure C.6: Focused ion beam images of second attempt at fabricating gold nanocap tips as illustrated in Figure 6.1(b) using a ZEISS Crossbeam 550 with a gallium ion source and the through-milling procedure outlined in Figure C.5. (a) Shows the definition of the ion beam exposure profile. F3 and F4 are the areas to be removed while the remaining shapes are guides to create the nanocap geometry required. The high resolution of the system allowed the nanocap to be defined accurately. (b) Shows the resulting structure which resulted after drift in the ion beam caused the exposure area to cut off the tip

Bibliography

[1] C. V. Raman and K. S. Krishnan, "A new type of secondary radiation," *Nature*, vol. 121, pp. 501–502, Mar. 1928.

[2] T. M. Niemczyk, M. M. Delgado-Lopez, and F. S. Allen, "Quantitative determination of bucindolol concentration in intact gel capsules using Raman spectroscopy," *Analytical Chemistry*, vol. 70, pp. 2762–2765, July 1998.

[3] G. J. Puppels, T. C. B. Schut, N. M. Sijtsema, M. Grond, F. Maraboeuf, C. G. de Grauw, C. G. Figdor, and J. Greve, "Development and application of Raman microspectroscopic and Raman imaging techniques for cell biological studies," *Journal of Molecular Structure*, vol. 347, pp. 477–483, Mar. 1995.

[4] V. R. Kodati, G. E. Tomasi, J. L. Turumin, and A. T. Tu, "Raman spectroscopic identification of phosphate-type kidney stones," *Applied Spectroscopy*, vol. 45, pp. 581–583, Apr. 1991.

[5] C. H. Liu, B. B. Das, W. L. S. Glassman, G. C. Tang, K. M. Yoo, H. R. Zhu, D. L. Akins, S. S. Lubicz, J. Cleary, R. Prudente, E. Celmer, A. Caron, and R. R. Alfano, "Raman, fluorescence, and time-resolved light scattering as optical diagnostic techniques to separate diseased and normal biomedical media," *Journal of Photochemistry and Photobiology B: Biology*, vol. 16, pp. 187–209, Oct. 1992.

[6] E. E. Lawson, B. W. Barry, A. C. Williams, and H. G. M. Edwards, "Biomedical applications of Raman spectroscopy," *Journal of Raman Spectroscopy*, vol. 28, no. 2-3, pp. 111–117, 1997.

[7] E. C. Y. Li-Chan, "The applications of Raman spectroscopy in food science," *Trends in Food Science & Technology*, vol. 11, no. 7, pp. 361–370, 1996.

[8] L. G. Cançado, A. Hartschuh, and L. Novotny, "Tip-enhanced Raman spectroscopy of carbon nanotubes," *Journal of Raman Spectroscopy*, vol. 40, no. 10, pp. 1420–1426, 2009.

[9] Z. J. Han, S. Yick, I. Levchenko, E. Tam, M. M. Aghili Yajadda, S. Kumar, P. Martin, S. Furman, and K. Ostrikov, "Controlled synthesis of a large fraction of metallic single-walled carbon nanotube and semiconducting carbon nanowire networks," *Nanoscale*, vol. 3, pp. 3214–20, June 2011.

[10] S. Costa, E. Borowiak-Palen, M. Kruszy, A. Bachmatiuk, and R. J. Kale, "Characterization of carbon nanotubes by Raman spectroscopy," *Materials Science-Poland*, vol. 26, no. 2, pp. 433–441, 2008.

[11] G. Eckhardt and W. G. Wagner, "On the calculation of absolute Raman scattering cross sections from Raman scattering coefficients," *Journal of Molecular Spectroscopy*, vol. 19, pp. 407–411, Jan. 1966.

[12] S. L. McCall, P. M. Platzman, and P. A. Wolff, "Surface enhanced Raman scattering," *Physics Letters A*, vol. 77, pp. 381–383, June 1980.

[13] K. Kneipp, Y. Wang, H. Kneipp, L. T. Perelman, I. Itzkan, R. R. Dasari, and M. S. Feld, "Single molecule detection using surface-enhanced Raman scattering (SERS)," *Physical Review Letters*, vol. 78, no. 9, p. 1667, 1997.

[14] K. A. Willets, "Super-resolution imaging of SERS hot spots," *Chemical Society Reviews*, vol. 43, no. 11, pp. 3854–3864, 2014.

[15] R. M. Stöckle, Y. D. Suh, V. Deckert, and R. Zenobi, "Nanoscale chemical analysis by tip-enhanced Raman spectroscopy," *Chemical Physics Letters*, vol. 318, no. 1, pp. 131–136, 2000.

[16] A. Hartschuh, E. J. Sánchez, X. S. Xie, and L. Novotny, "High-resolution near-field Raman microscopy of single-walled carbon nanotubes," *Physical Review Letters*, vol. 90, p. 095503, Mar. 2003.

[17] R. Böhme, D. Cialla, M. Richter, P. Rösch, J. Popp, and V. Deckert, "Biochemical imaging below the diffraction limit – Probing cellular membrane related structures by tip-enhanced Raman spectroscopy (TERS)," *Journal of Biophotonics*, vol. 3, no. 7, pp. 455–461, 2010.

[18] B. J. Wiley, S. H. Im, Z.-Y. Li, J. McLellan, A. Siekkinen, and Y. Xia, "Maneuvering the surface plasmon resonance of silver nanostructures through shape-controlled synthesis," *The Journal of Physical Chemistry B*, vol. 110, pp. 15666–15675, Aug. 2006.

[19] P. Verma, "Tip-enhanced Raman spectroscopy: Technique and recent advances," *Chemical Reviews*, vol. 117, pp. 6447–6466, May 2017.

[20] M. McMahon, R. Lopez, H. Meyer, L. Feldman, and R. Haglund, "Rapid tarnishing of silver nanoparticles in ambient laboratory air," *Applied Physics B*, vol. 80, no. 7, pp. 915–921, 2005.

[21] P. R. Brejna and P. R. Griffiths, "Electroless deposition of silver onto silicon as a method of preparation of reproducible surface-enhanced Raman spectroscopy substrates and tip-enhanced Raman spectroscopy tips," *Applied Spectroscopy*, vol. 64, pp. 493–499, May 2010.

[22] T.-X. Huang, S.-C. Huang, M.-H. Li, Z.-C. Zeng, X. Wang, and B. Ren, "Tip-enhanced Raman spectroscopy: Tip-related issues," *Analytical and Bioanalytical Chemistry*, vol. 407, pp. 8177–8195, Nov. 2015.

[23] Z. Yang, J. Aizpurua, and H. Xu, "Electromagnetic field enhancement in TERS configurations," *Journal of Raman Spectroscopy*, vol. 40, pp. 1343–1348, Oct. 2009.

[24] B. Pettinger, P. Schambach, C. J. Villagómez, and N. Scott, "Tip-enhanced Raman spectroscopy: Near-fields acting on a few molecules," *Annual Review of Physical Chemistry*, vol. 63, pp. 379–399, May 2012.

[25] J. Steidtner and B. Pettinger, "Tip-enhanced Raman spectroscopy and microscopy on single dye molecules with 15 nm resolution," *Physical Review Letters*, vol. 100, p. 236101, June 2008.

[26] C. V. Raman and K. S. Krishnan, "Polarisation of scattered light-quanta," *Nature*, vol. 122, pp. 169–169, Aug. 1928.

[27] E. Smith and G. Dent, *Modern Raman Spectroscopy: A Practical Approach*. John Wiley & Sons, Apr. 2019.

[28] A. Kudelski, "Raman spectroscopy of surfaces," *Surface Science*, vol. 603, pp. 1328–1334, June 2009.

[29] U. J. Kim, C. A. Furtado, X. Liu, G. Chen, and P. C. Eklund, "Raman and IR spectroscopy of chemically processed single-walled carbon nanotubes," *Journal of the American Chemical Society*, vol. 127, pp. 15437–15445, Nov. 2005.

[30] H. Kuzmany, W. Plank, M. Hulman, C. Kramberger, A. Grüneis, T. Pichler, H. Peterlik, H. Kataura, and Y. Achiba, "Determination of SWCNT diameters from the Raman response of the radial breathing mode," *The European Physical Journal B - Condensed Matter and Complex Systems*, vol. 22, pp. 307–320, Aug. 2001.

[31] J. Maultzsch, H. Telg, S. Reich, and C. Thomsen, "Radial breathing mode of single-walled carbon nanotubes: Optical transition energies and chiral-index assignment," *Physical Review B*, vol. 72, p. 205438, Nov. 2005.

[32] R. H. Webb, "Confocal optical microscopy," *Reports on Progress in Physics*, vol. 59, p. 427, Mar. 1996.

[33] R. Aroca, *Surface-Enhanced Vibrational Spectroscopy*. John Wiley & Sons, May 2006.

[34] G. W. Faris and R. A. Copeland, "Wavelength dependence of the Raman cross section for liquid water," *Applied optics*, vol. 36, no. 12, pp. 2686–2688, 1997.

[35] A. M. Michaels, M. Nirmal, and L. E. Brus, "Surface enhanced Raman spectroscopy of individual rhodamine 6G molecules on large Ag nanocrystals," *Journal of the American Chemical Society*, vol. 121, pp. 9932–9939, Nov. 1999.

[36] M. D. Sonntag, J. M. Klingsporn, L. K. Garibay, J. M. Roberts, J. A. Dieringer, T. Seideman, K. A. Scheidt, L. Jensen, G. C. Schatz, and R. P. Van Duyne, "Single-molecule tip-enhanced Raman spectroscopy," *The Journal of Physical Chemistry C*, vol. 116, pp. 478–483, Jan. 2012.

[37] F. H. M. Jongsma, R. J. Erckens, J. P. Wicksted, N. J. C. Bauer, F. Hendrikse, W. F. March, and M. Motamedi, "Confocal Raman spectroscopy system for noncontact scanning of ocular tissues: An in vitro study," *Optical Engineering*, vol. 36, pp. 3193–3199, Nov. 1997.

[38] E. McLeod and A. Ozcan, "Nano-imaging enabled via self-assembly," *Nano Today*, vol. 9, pp. 560–573, Oct. 2014.

[39] M. Pelton and G. W. Bryant, "Introduction to metal-nanoparticle plasmonics," in *Introduction to Metal-Nanoparticle Plasmonics*, vol. 5, pp. xi–xii, John Wiley & Sons, 2013.

[40] V. Giannini, A. I. Fernández-Domínguez, S. C. Heck, and S. A. Maier, "Plasmonic nanoantennas: Fundamentals and their use in controlling the radiative properties of nanoemitters," *Chemical Reviews*, vol. 111, pp. 3888–3912, June 2011.

[41] C. Girard and A. Dereux, "Near-field optics theories," *Reports on Progress in Physics*, vol. 59, no. 5, p. 657, 1996.

[42] C. A. Balanis, "Antenna theory: A review," *Proceedings of the IEEE*, vol. 80, no. 1, pp. 7–23, 1992.

[43] A. Kristensen, J. K. W. Yang, S. I. Bozhevolnyi, S. Link, P. Nordlander, N. J. Halas, and N. A. Mortensen, "Plasmonic colour generation," *Nature Reviews Materials*, vol. 2, pp. 1–14, Nov. 2016.

[44] A. V. Zayats, I. I. Smolyaninov, and A. A. Maradudin, "Nano-optics of surface plasmon polaritons," *Physics Reports*, vol. 408, pp. 131–314, Mar. 2005.

[45] D. Alastair Smith, S. Webster, M. Ayad, S. D. Evans, D. Fogherty, and D. Batchelder, "Development of a scanning near-field optical probe for localised Raman spectroscopy," *Ultramicroscopy*, vol. 61, pp. 247–252, Dec. 1995.

[46] T. Schmid, L. Opilik, C. Blum, and R. Zenobi, "Nanoscale chemical imaging using tip-enhanced Taman spectroscopy: A critical review," *Angewandte Chemie International Edition*, vol. 52, no. 23, pp. 5940–5954, 2013.

[47] E. Betzig, J. Trautman, *et al.*, "Near-field optics- Microscopy, spectroscopy, and surface modification beyond the diffraction limit," *Science*, vol. 257, no. 5067, pp. 189–195, 1992.

[48] W. Noell, M. Abraham, K. Mayr, A. Ruf, J. Barenz, O. Hollricher, O. Marti, and P. Güthner, "Micromachined aperture probe tip for multifunctional scanning probe microscopy," *Applied Physics Letters*, vol. 70, pp. 1236–1238, Mar. 1997.

[49] A. A. Tseng, "Recent developments in nanofabrication using scanning near-field optical microscope lithography," *Optics & Laser Technology*, vol. 39, no. 3, pp. 514–526, 2007.

[50] L. Novotny, D. W. Pohl, and P. Regli, "Light propagation through nanometer-sized structures: The two-dimensional-aperture scanning near-field optical microscope," *Journal of the Optical Society of America A*, vol. 11, pp. 1768–1779, June 1994.

[51] B. S. Routley, J. L. Holdsworth, and A. J. Fleming, "Optimization of near-field scanning optical lithography," in *SPIE Advanced Lithography*, p. 94230F, International Society for Optics and Photonics, 2015.

[52] A. Hartschuh, N. Anderson, and L. Novotny, "Near-field Raman spectroscopy using a sharp metal tip," *Journal of Microscopy*, vol. 210, pp. 234–240, June 2003.

[53] J. Yu, Y. Saito, T. Ichimura, S. Kawata, and P. Verma, "Far-field free tapping-mode tip-enhanced Raman microscopy," *Applied Physics Letters*, vol. 102, p. 123110, Mar. 2013.

[54] A. V. Ermushev, B. V. Mchedlishvili, V. A. Oleĭnikov, and A. V. Petukhov, "Surface enhancement of local optical fields and the lightning-rod effect," *Quantum Electronics*, vol. 23, pp. 435–440, May 1993.

[55] J. I. Gersten, "The effect of surface roughness on surface enhanced Raman scattering," *The Journal of Chemical Physics*, vol. 72, pp. 5779–5780, May 1980.

[56] P. Liao and A. Wokaun, "Lightning rod effect in surface enhanced Raman scattering," *The Journal of Chemical Physics*, vol. 76, no. 1, pp. 751–752, 1982.

[57] M. Rahaman, A. G. Milekhin, A. Mukherjee, E. E. Rodyakina, A. V. Latyshev, V. M. Dzhagan, and D. R. T. Zahn, "The role of a plasmonic substrate on the enhancement and spatial resolution of tip-enhanced Raman scattering," *Faraday Discussions*, vol. 214, no. 0, pp. 309–323, 2019.

[58] P. H. McBreen and M. Moskovits, "Optical properties of silver films deposited at low temperatures," *Journal of Applied Physics*, vol. 54, pp. 329–335, Jan. 1983.

[59] J. T. Stuckless and M. Moskovits, "Enhanced two-photon photoemission from coldly deposited silver films," *Physical Review B*, vol. 40, pp. 9997–9998, Nov. 1989.

[60] E. Le Ru, E. Blackie, M. Meyer, and P. G. Etchegoin, "Surface enhanced Raman scattering enhancement factors: A comprehensive study," *The Journal of Physical Chemistry C*, vol. 111, no. 37, pp. 13794–13803, 2007.

[61] B. Yosif and A. S. Samra, "Modeling of optical nanoantennas," *Physics Research International*, vol. 2012, 2012.

[62] J. Ma, J. Song, Y. Cheng, and M. Sun, "Plexciton and electron–phonon interaction in tip-enhanced resonance Raman scattering," *Journal of Raman Spectroscopy*, vol. 52, no. 10, pp. 1685–1697, 2021.

[63] J. Ma, Y. Cheng, and M. Sun, "Plexcitons, electric field gradient and electron–phonon coupling in tip-enhanced Raman spectroscopy (TERS)," *Nanoscale*, vol. 13, no. 24, pp. 10712–10725, 2021.

[64] R. Zhang, Y. Zhang, Z. C. Dong, S. Jiang, C. Zhang, L. G. Chen, L. Zhang, Y. Liao, J. Aizpurua, Y. Luo, J. L. Yang, and J. G. Hou, "Chemical mapping of a single molecule by plasmon-enhanced Raman scattering," *Nature*, vol. 498, pp. 82–86, June 2013.

[65] W. Zhang, B. S. Yeo, T. Schmid, and R. Zenobi, "Single molecule tip-enhanced Raman spectroscopy with silver tips," *The Journal of Physical Chemistry C*, vol. 111, pp. 1733–1738, Feb. 2007.

[66] J. Stadler, B. Oswald, T. Schmid, and R. Zenobi, "Characterizing unusual metal substrates for gap-mode tip-enhanced Raman spectroscopy," *Journal of Raman Spectroscopy*, vol. 44, no. 2, pp. 227–233, 2013.

[67] L. Meng, Y. Wang, M. Gao, and M. Sun, "Electromagnetic field gradient-enhanced raman scattering in TERS configurations," *The Journal of Physical Chemistry C*, vol. 125, pp. 5684–5691, Mar. 2021.

[68] A. K. Sivadasan, A. Patsha, A. Maity, T. K. Chini, and S. Dhara, "Effect of scattering efficiency in the tip-enhanced Raman spectroscopic imaging of nanostructures in the sub-diffraction limit," *The Journal of Physical Chemistry C*, vol. 121, pp. 26967–26975, Dec. 2017.

[69] G. S. Duesberg, I. Loa, M. Burghard, K. Syassen, and S. Roth, "Polarized Raman spectroscopy on isolated single-wall carbon nanotubes," *Physical Review Letters*, vol. 85, pp. 5436–5439, Dec. 2000.

[70] A. Jorio, A. P. Santos, H. B. Ribeiro, C. Fantini, M. Souza, J. P. M. Vieira, C. A. Furtado, J. Jiang, R. Saito, L. Balzano, D. E. Resasco, and M. A. Pimenta, "Quantifying carbon-nanotube species with resonance Raman scattering," *Physical Review B*, vol. 72, p. 075207, Aug. 2005.

[71] M. Y. Sfeir, T. Beetz, F. Wang, L. Huang, X. M. H. Huang, M. Huang, J. Hone, S. O'Brien, J. A. Misewich, T. F. Heinz, L. Wu, Y. Zhu, and L. E. Brus, "Optical Spectroscopy of Individual Single-Walled Carbon Nanotubes of Defined Chiral Structure," *Science*, vol. 312, pp. 554–556, Apr. 2006.

[72] K. Lee and M. A. El-Sayed, "Gold and silver nanoparticles in sensing and imaging: Sensitivity of plasmon response to size, shape, and metal composition," *The Journal of Physical Chemistry B*, vol. 110, no. 39, pp. 19220–19225, 2006.

[73] A. Sanders, L. Zhang, R. Bowman, L. O. Herrmann, and J. Baumberg, "Facile fabrication of spherical nanoparticle-tipped AFM probes for plasmonic applications," *Particle & Particle Systems Characterization*, vol. 32, Aug. 2014.

[74] J. P. Camden, J. A. Dieringer, Y. Wang, D. J. Masiello, L. D. Marks, G. C. Schatz, and R. P. Van Duyne, "Probing the structure of single-molecule surface-enhanced Raman scattering hot spots," *Journal of the American Chemical Society*, vol. 130, pp. 12616–12617, Sept. 2008.

[75] W. Zhang, Cui, B.-S. Yeo, T. Schmid, C. Hafner, and R. Zenobi, "Nanoscale Roughness on Metal Surfaces Can Increase Tip-Enhanced Raman Scattering by an Order of Magnitude," *Nano Letters*, vol. 7, pp. 1401–1405, May 2007.

[76] A. Taguchi, J. Yu, P. Verma, and S. Kawata, "Optical antennas with multiple plasmonic nanoparticles for tip-enhanced Raman microscopy," *Nanoscale*, vol. 7, no. 41, pp. 17424–17433, 2015.

[77] T. W. H. Oates, M. Losurdo, S. Noda, and K. Hinrichs, "The effect of atmospheric tarnishing on the optical and structural properties of silver nanoparticles," *Journal of Physics D: Applied Physics*, vol. 46, p. 145308, Mar. 2013.

[78] V. J. Keast, T. A. Myles, N. Shahcheraghi, and M. B. Cortie, "Corrosion processes of triangular silver nanoparticles compared to bulk silver," *Journal of Nanoparticle Research*, vol. 18, p. 45, Feb. 2016.

[79] Z. Zhang, S. Sheng, R. Wang, and M. Sun, "Tip-enhanced Raman spectroscopy," *Analytical Chemistry*, vol. 88, pp. 9328–9346, Oct. 2016.

[80] K. Crozier, A. Sundaramurthy, G. Kino, and C. Quate, "Optical antennas: Resonators for local field enhancement," *Journal of Applied Physics*, vol. 94, no. 7, pp. 4632–4642, 2003.

[81] L. He, M. Rahaman, T. I. Madeira, and D. R. T. Zahn, "Understanding the role of different substrate geometries for achieving optimum tip-enhanced Raman scattering sensitivity," *Nanomaterials*, vol. 11, p. 376, Feb. 2021.

[82] R. M. Roth, N. C. Panoiu, M. M. Adams, R. M. Osgood, C. C. Neacsu, and M. B. Raschke, "Resonant-plasmon field enhancement from asymmetrically illuminated conical metallic-probe tips," *Optics Express*, vol. 14, pp. 2921–2931, Apr. 2006.

[83] A. Downes, D. Salter, and A. Elfick, "Finite element simulations of tip-enhanced Raman and fluorescence spectroscopy," *The Journal of Physical Chemistry B*, vol. 110, pp. 6692–6698, Apr. 2006.

[84] M. Micic, N. Klymyshyn, Y. D. Suh, and H. P. Lu, "Finite element method simulation of the field distribution for AFM tip-enhanced surface-enhanced Raman scanning microscopy," *The Journal of Physical Chemistry B*, vol. 107, pp. 1574–1584, Feb. 2003.

[85] F. Stade, A. Heeren, M. Fleischer, and D. Kern, "Fabrication of metallic nanostructures for investigating plasmon-induced field enhancement," *Microelectronic Engineering*, vol. 84, no. 5, pp. 1589–1592, 2007.

[86] A. Haidary, Y. Miyahara, and P. Grütter, "Antenna and plasmonic properties of scanning probe tips at optical and terahertz regimes," in *Proceedings of the 2014 COMSOL Conference in Boston*, (Boston), p. 6, 2014.

[87] R. L. Olmon, B. Slovick, T. W. Johnson, D. Shelton, S.-H. Oh, G. D. Boreman, and M. B. Raschke, "Optical dielectric function of gold," *Physical Review B*, vol. 86, p. 235147, Dec. 2012.

[88] I. Haddouche and L. Cherbi, "Comparison of finite element and transfer matrix methods for numerical investigation of surface plasmon waveguides," *Optics Communications*, vol. 382, pp. 132–137, Jan. 2017.

[89] S. Salon and J. D'Angelo, "Applications of the hybrid finite element-boundary element method in electromagnetics," *IEEE Transactions on Magnetics*, vol. 24, pp. 80–85, Jan. 1988.

[90] V. Myroshnychenko, E. Carbó-Argibay, I. Pastoriza-Santos, J. Pérez-Juste, L. M. Liz-Marzán, and F. J. García de Abajo, "Modeling the optical response of highly faceted metal nanoparticles with a fully 3D boundary element method," *Advanced Materials*, vol. 20, no. 22, pp. 4288–4293, 2008.

[91] U. Hohenester and A. Trügler, "MNPBEM – A Matlab toolbox for the simulation of plasmonic nanoparticles," *Computer Physics Communications*, vol. 183, no. 2, pp. 370–381, 2012.

[92] J. Waxenegger, A. Trügler, and U. Hohenester, "Plasmonics simulations with the MNPBEM toolbox: Consideration of substrates and layer structures," *Computer Physics Communications*, vol. 193, pp. 138–150, 2015.

[93] A. Trügler, U. Hohenester, and F. J. García de Abajo, "Plasmonics simulations including nonlocal effects using a boundary element method approach," *International Journal of Modern Physics B*, vol. 31, p. 1740007, Sept. 2017.

[94] P. B. Johnson and R. W. Christy, "Optical constants of the noble metals," *Physical review. B.*, vol. 6, pp. 4370–4379, Dec. 1972.

[95] M. B. Raschke and C. Lienau, "Apertureless near-field optical microscopy: Tip–sample coupling in elastic light scattering," *Applied Physics Letters*, vol. 83, pp. 5089–5091, Dec. 2003.

[96] A. Bouhelier, J. Renger, M. R. Beversluis, and L. Novotny, "Plasmon-coupled tip-enhanced near-field optical microscopy," *Journal of Microscopy*, vol. 210, pp. 220–224, June 2003.

[97] W. Haske, V. W. Chen, J. M. Hales, W. Dong, S. Barlow, S. R. Marder, and J. W. Perry, "65 nm feature sizes using visible wavelength 3D multiphoton lithography," *Optics express*, vol. 15, no. 6, pp. 3426–3436, 2007.

[98] G. W. Bryant, F. J. García de Abajo, and J. Aizpurua, "Mapping the plasmon resonances of metallic nanoantennas," *Nano Letters*, vol. 8, pp. 631–636, Feb. 2008.

[99] H. Liang, D. Rossouw, H. Zhao, S. K. Cushing, H. Shi, A. Korinek, H. Xu, F. Rosei, W. Wang, N. Wu, G. A. Botton, and D. Ma, "Asymmetric silver "nanocarrot" structures: Solution synthesis and their asymmetric plasmonic resonances," *Journal of the American Chemical Society*, vol. 135, pp. 9616–9619, July 2013.

[100] A. L. Demming, F. Festy, and D. Richards, "Plasmon resonances on metal tips: Understanding tip-enhanced Raman scattering," *The Journal of Chemical Physics*, vol. 122, p. 184716, May 2005.

[101] P. K. Jain, S. Eustis, and M. A. El-Sayed, "Plasmon coupling in nanorod assemblies: optical absorption, discrete dipole approximation simulation, and exciton-coupling model," *The Journal of Physical Chemistry B*, vol. 110, pp. 18243–18253, Sept. 2006.

[102] J. Nelayah, M. Kociak, O. Stéphan, F. J. García de Abajo, M. Tencé, L. Henrard, D. Taverna, I. Pastoriza-Santos, L. M. Liz-Marzán, and C. Colliex, "Mapping surface plasmons on a single metallic nanoparticle," *Nature Physics*, vol. 3, pp. 348–353, May 2007.

[103] L. R. McCourt, M. G. Ruppert, B. S. Routley, S. C. Indirathankam, and A. J. Fleming, "A comparison of gold and silver nanocones and geometry optimisation for tip-enhanced microscopy," *Journal of Raman Spectroscopy*, vol. 51, no. 11, pp. 2208–2216, 2020.

[104] L. R. McCourt, "Resolution and enhancement of probes for nearfield two photon apertureless lithography," in *Nanophotonics and Micro/Nano Optics International Conference 2019*, (Munich), p. 197, Sept. 2019.

[105] T.-X. Huang, C.-W. Li, L.-K. Yang, J.-F. Zhu, X. Yao, C. Liu, K.-Q. Lin, Z.-C. Zeng, S.-S. Wu, X. Wang, F.-Z. Yang, and B. Ren, "Rational fabrication of silver-coated AFM TERS tips with a high enhancement and long lifetime," *Nanoscale*, vol. 10, no. 9, pp. 4398–4405, 2018.

[106] Y. Fujita, P. Walke, S. De Feyter, and H. Uji-i, "Tip-enhanced Raman scattering microscopy: Recent advance in tip production," *Japanese Journal of Applied Physics*, vol. 55, p. 08NA02, Aug. 2016.

[107] M. G. Ruppert, B. S. Routley, L. R. McCourt, Y. K. Yong, and A. J. Fleming, "Modulated-illumination intermittent contact tip-enhanced Raman spectroscopy: Simultaneous imaging of surface and material properties," *Manuscript submitted for publication*, 2020.

[108] M. Fleischer, A. Weber-Bargioni, M. V. P. Altoe, A. M. Schwartzberg, P. J. Schuck, S. Cabrini, and D. P. Kern, "Gold nanocone near-field scanning optical microscopy probes," *ACS Nano*, vol. 5, pp. 2570–2579, Apr. 2011.

[109] J. T. Krug, E. J. Sánchez, and X. S. Xie, "Design of near-field optical probes with optimal field enhancement by finite difference time domain electromagnetic simulation," *The Journal of Chemical Physics*, vol. 116, pp. 10895–10901, June 2002.

[110] F. Festy, A. Demming, and D. Richards, "Resonant excitation of tip plasmons for tip-enhanced Raman SNOM," *Ultramicroscopy*, vol. 100, no. 3-4, pp. 437–441, 2004.

[111] A. Mohammadi, F. Kaminski, V. Sandoghdar, and M. Agio, "Fluorescence enhancement with the optical (bi-) conical antenna," *The Journal of Physical Chemistry C*, vol. 114, pp. 7372–7377, Apr. 2010.

[112] C. Schäfer, D. A. Gollmer, A. Horrer, J. Fulmes, A. Weber-Bargioni, S. Cabrini, P. James Schuck, D. P. Kern, and M. Fleischer, "A single particle plasmon resonance study of 3D conical nanoantennas," *Nanoscale*, vol. 5, no. 17, pp. 7861–7866, 2013.

[113] Y. C. Martin, H. F. Hamann, and H. K. Wickramasinghe, "Strength of the electric field in apertureless near-field optical microscopy," *Journal of applied physics*, vol. 89, no. 10, pp. 5774–5778, 2001.

[114] N. Hayazawa, Y. Inouye, Z. Sekkat, and S. Kawata, "Near-field Raman scattering enhanced by a metallized tip," *Chemical Physics Letters*, vol. 335, pp. 369–374, Mar. 2001.

[115] R. J. Hermann and M. J. Gordon, "Quantitative comparison of plasmon resonances and field enhancements of near-field optical antennae using FDTD simulations," *Optics Express*, vol. 26, pp. 27668–27682, Oct. 2018.

[116] H. Furukawa and S. Kawata, "Local field enhancement with an apertureless near-field-microscope probe," *Optics Communications*, vol. 148, no. 4, pp. 221–224, 1998.

[117] B. Pettinger, K. F. Domke, D. Zhang, R. Schuster, and G. Ertl, "Direct monitoring of plasmon resonances in a tip-surface gap of varying width," *Physical Review B*, vol. 76, Sept. 2007.

[118] T.-a. Yano, T. Ichimura, A. Taguchi, N. Hayazawa, P. Verma, Y. Inouye, and S. Kawata, "Confinement of enhanced field investigated by tip-sample gap regulation in tapping-mode tip-enhanced Raman microscopy," *Applied Physics Letters*, vol. 91, p. 121101, Sept. 2007.

[119] E. Meyer, "Atomic force microscopy," *Progress in Surface Science*, vol. 41, pp. 3–49, Sept. 1992.

[120] G. Binnig, C. Gerber, E. Stoll, T. R. Albrecht, and C. F. Quate, "Atomic resolution with atomic force microscope," *Europhysics Letters (EPL)*, vol. 3, pp. 1281–1286, June 1987.

[121] Y. L. Lyubchenko and L. S. Shlyakhtenko, "AFM for analysis of structure and dynamics of DNA and protein–DNA complexes," *Methods*, vol. 47, pp. 206–213, Mar. 2009.

[122] L. Chopinet, C. Formosa, M. P. Rols, R. E. Duval, and E. Dague, "Imaging living cells surface and quantifying its properties at high resolution using AFM in QI™ mode," *Micron*, vol. 48, pp. 26–33, May 2013.

[123] M. P. Boneschanscher, J. van der Lit, Z. Sun, I. Swart, P. Liljeroth, and D. Vanmaekelbergh, "Quantitative atomic resolution force imaging on epitaxial graphene with reactive and nonreactive AFM probes," *ACS Nano*, vol. 6, pp. 10216–10221, Nov. 2012.

[124] P. Avouris, R. Martel, T. Hertel, and R. Sandstrom, "AFM-tip-induced and current-induced local oxidation of silicon and metals," *Applied Physics A: Materials Science & Processing*, vol. 66, pp. S659–S667, Mar. 1998.

[125] N. Jalili and K. Laxminarayana, "A review of atomic force microscopy imaging systems: Application to molecular metrology and biological sciences," *Mechatronics*, vol. 14, pp. 907–945, Oct. 2004.

[126] I. Schmitz, M. Schreiner, G. Friedbacher, and M. Grasserbauer, "Tapping-mode AFM in comparison to contact-mode AFM as a tool for in situ investigations of surface reactions with reference to glass corrosion," *Analytical Chemistry*, vol. 69, pp. 1012–1018, Mar. 1997.

[127] A. Ulcinas and V. Snitka, "Intermittent contact AFM using the higher modes of weak cantilever," *Ultramicroscopy*, vol. 86, pp. 217–222, Jan. 2001.

[128] J. P. Cleveland, B. Anczykowski, A. E. Schmid, and V. B. Elings, "Energy dissipation in tapping-mode atomic force microscopy," *Applied Physics Letters*, vol. 72, pp. 2613–2615, May 1998.

[129] J. Zhao, H. Lui, D. I. McLean, and H. Zeng, "Automated autofluorescence background subtraction algorithm for biomedical Raman spectroscopy," *Applied Spectroscopy*, vol. 61, pp. 1225–1232, Nov. 2007.

[130] P. J. Cadusch, M. M. Hlaing, S. A. Wade, S. L. McArthur, and P. R. Stoddart, "Improved methods for fluorescence background subtraction from Raman spectra," *Journal of Raman Spectroscopy*, vol. 44, no. 11, pp. 1587–1595, 2013.

[131] W. Zhou, R. Apkarian, Z. L. Wang, and D. Joy, "Fundamentals of scanning electron microscopy (SEM)," in *Scanning Microscopy for Nanotechnology*, pp. 1–40, Springer, 2006.

[132] M. Schmied and P. Poelt, "Particle analysis by SEM/EDXS and specimen damage," *Microchimica Acta*, vol. 139, pp. 171–177, May 2002.

[133] N. Okai and Y. Sohda, "Study on image drift induced by charging during observation by scanning electron microscope," *Japanese Journal of Applied Physics*, vol. 51, p. 06FB11, June 2012.

[134] D. Shindo and T. Oikawa, "Energy dispersive x-ray spectroscopy," in *Analytical Electron Microscopy for Materials Science* (D. Shindo and T. Oikawa, eds.), pp. 81–102, Tokyo: Springer Japan, 2002.

[135] D. Titus, E. James Jebaseelan Samuel, and S. M. Roopan, "Chapter 12 - Nanoparticle characterization techniques," in *Green Synthesis, Characterization and Applications of Nanoparticles* (A. K. Shukla and S. Iravani, eds.), Micro and Nano Technologies, pp. 303–319, Elsevier, Jan. 2019.

[136] N. Kumar, W. Su, M. Veselý, B. M. Weckhuysen, A. J. Pollard, and A. J. Wain, "Nanoscale chemical imaging of solid–liquid interfaces using tip-enhanced Raman spectroscopy," *Nanoscale*, vol. 10, no. 4, pp. 1815–1824, 2018.

[137] J. Steidtner and B. Pettinger, "High-resolution microscope for tip-enhanced optical processes in ultrahigh vacuum," *Review of Scientific Instruments*, vol. 78, p. 103104, Oct. 2007.

[138] N. Hayazawa, Y. Inouye, Z. Sekkat, and S. Kawata, "Metallized tip amplification of near-field Raman scattering," *Optics Communications*, vol. 183, pp. 333–336, Sept. 2000.

[139] N. Hayazawa, T. Yano, H. Watanabe, Y. Inouye, and S. Kawata, "Detection of an individual single-wall carbon nanotube by tip-enhanced near-field Raman spectroscopy," *Chemical Physics Letters*, vol. 376, pp. 174–180, July 2003.

[140] D. Roy, J. Wang, and C. Williams, "Novel methodology for estimating the enhancement factor for tip-enhanced Raman spectroscopy," *Journal of Applied Physics*, vol. 105, p. 013530, Jan. 2009.

[141] B. Pettinger, G. Picardi, R. Schuster, and G. Ertl, "Surface enhanced Raman spectroscopy: Towards single molecule spectroscopy," *Electrochemistry*, vol. 68, no. 12, pp. 942–949, 2000.

[142] K. Rossmann, "Point spread-function, line spread-function, and modulation transfer function," *Radiology*, vol. 93, pp. 257–272, Aug. 1969.

[143] P. McEuen, M. Fuhrer, and H. Park, "Single-walled carbon nanotube electronics," *IEEE Transactions on Nanotechnology*, vol. 1, pp. 78–85, Mar. 2002.

[144] P. T. Araujo, I. O. Maciel, P. B. C. Pesce, M. A. Pimenta, S. K. Doorn, H. Qian, A. Hartschuh, M. Steiner, L. Grigorian, K. Hata, and A. Jorio, "Nature of the constant factor in the relation between radial breathing mode frequency and tube diameter for single-wall carbon nanotubes," *Physical Review B*, vol. 77, p. 241403, June 2008.

[145] A. Jorio, R. Saito, J. H. Hafner, C. M. Lieber, M. Hunter, T. McClure, G. Dresselhaus, and M. S. Dresselhaus, "Structural (n,m) determination of isolated single-wall carbon nanotubes by resonant Raman scattering," *Physical Review Letters*, vol. 86, pp. 1118–1121, Feb. 2001.

[146] A. G. Souza Filho, S. G. Chou, G. G. Samsonidze, G. Dresselhaus, M. S. Dresselhaus, L. An, J. Liu, A. K. Swan, M. S. Ünlü, B. B. Goldberg, A. Jorio, A. Grüneis, and R. Saito, "Stokes and anti-Stokes Raman spectra of small-diameter isolated carbon nanotubes," *Physical Review B*, vol. 69, p. 115428, Mar. 2004.

[147] H. Ajiki and T. Ando, "Aharonov-Bohm effect in carbon nanotubes," *Physica B: Condensed Matter*, vol. 201, pp. 349–352, July 1994.

[148] P. Araujo, P. Pesce, M. Dresselhaus, K. Sato, R. Saito, and A. Jorio, "Resonance Raman spectroscopy of the radial breathing modes in carbon nanotubes," *Physica E: Low-dimensional Systems and Nanostructures*, vol. 42, pp. 1251–1261, Mar. 2010.

[149] C. Chen, N. Hayazawa, and S. Kawata, "A 1.7 nm resolution chemical analysis of carbon nanotubes by tip-enhanced Raman imaging in the ambient," *Nature Communications*, vol. 5, p. 3312, Feb. 2014.

[150] A. Hartschuh, N. Anderson, and L. Novotny, "Near-field Raman spectroscopy using a sharp metal tip," *Journal of Microscopy*, vol. 210, no. 3, pp. 234–240, 2003.

[151] V. J. Keast, "Corrosion Processes of silver nanoparticles," *Applied Nanoscience*, 2022.

[152] B. Pettinger, B. Ren, G. Picardi, R. Schuster, and G. Ertl, "Tip-enhanced Raman spectroscopy (TERS) of malachite green isothiocyanate at Au(111): Bleaching behavior under the influence of high electromagnetic fields," *Journal of Raman Spectroscopy*, vol. 36, no. 6-7, pp. 541–550, 2005.

[153] Y. Wu, G. Li, and J. P. Camden, "Probing nanoparticle plasmons with electron energy loss spectroscopy," *Chemical Reviews*, vol. 118, pp. 2994–3031, Mar. 2018.

[154] J. Lee, K. T. Crampton, N. Tallarida, and V. Apkarian, "Visualizing vibrational normal modes of a single molecule with atomically confined light," *Nature*, vol. 568, no. 7750, pp. 78–82, 2019.

[155] M. Asghari-Khiavi, B. R. Wood, P. Hojati-Talemi, A. Downes, D. McNaughton, and A. Mechler, "Exploring the origin of tip-enhanced Raman scattering; preparation of efficient TERS probes with high yield," *Journal of Raman Spectroscopy*, vol. 43, pp. 173–180, Feb. 2012.

[156] A. Taguchi, "Plasmonic tip for nano Raman microcopy: Structures, materials, and enhancement," *Optical Review*, vol. 24, pp. 462–469, June 2017.

[157] A. R. Neto, C. Rabelo, L. G. Cançado, M. Engel, M. Steiner, and A. Jorio, "Protocol and reference material for measuring the nanoantenna enhancement factor in Tip-enhanced Raman Spectroscopy," in *2019 4th International Symposium on Instrumentation Systems, Circuits and Transducers (INSCIT)*, pp. 1–6, Aug. 2019.

[158] T. L. Vasconcelos, B. S. Archanjo, B. S. Oliveira, W. F. Silva, R. S. Alencar, C. Rabelo, C. A. Achete, A. Jorio, and L. G. Cançado, "Optical nanoantennas for tip-enhanced Raman spectroscopy," *IEEE Journal of Selected Topics in Quantum Electronics*, vol. 27, pp. 1–11, Jan. 2021.

[159] Y. S. Hu, J. Jeon, T. J. Seok, S. Lee, J. H. Hafner, R. A. Drezek, and H. Choo, "Enhanced Raman scattering from nanoparticle-decorated nanocone substrates: A practical approach to harness in-plane excitation," *ACS Nano*, vol. 4, pp. 5721–5730, Oct. 2010.

[160] L. Mehrvar, M. Sadeghipari, S. H. Tavassoli, S. Mohajerzadeh, and M. Fathipour, "Optical and surface enhanced Raman scattering properties of Ag modified silicon double nanocone array," *Scientific Reports*, vol. 7, p. 12106, Sept. 2017.

[161] S. Rao, M. J. Huttunen, J. M. Kontio, J. Makitalo, M.-R. Viljanen, J. Simonen, M. Kauranen, and D. Petrov, "Tip-enhanced Raman scattering from bridged nanocones," *Optics Express*, vol. 18, pp. 23790–23795, Nov. 2010.

[162] B. Hoffmann, S. Vassant, X.-W. Chen, S. Götzinger, V. Sandoghdar, and S. Christiansen, "Fabrication and characterization of plasmonic nanocone antennas for strong spontaneous emission enhancement," *Nanotechnology*, vol. 26, p. 404001, Oct. 2015.

[163] O. Tanirah, D. P. Kern, and M. Fleischer, "Fabrication of a plasmonic nanocone on top of an AFM cantilever," *Microelectronic Engineering*, vol. 141, pp. 215–218, June 2015.

[164] S. Kawata and V. M. Shalaev, eds., *Tip Enhancement*. Advances in Nano-Optics and Nano-Photonics, Amsterdam ; Boston: Elsevier, 2007.

[165] T. Mino, Y. Saito, and P. Verma, "Quantitative analysis of polarization-controlled tip-enhanced Raman imaging through the evaluation of the tip dipole," *ACS Nano*, vol. 8, pp. 10187–10195, Oct. 2014.

[166] V. L. Schlegel and T. M. Cotton, "Silver-island films as substrates for enhanced Raman scattering: Effect of deposition rate on intensity," *Analytical Chemistry*, vol. 63, pp. 241–247, Feb. 1991.

[167] Y. Saito, J. J. Wang, D. N. Batchelder, and D. A. Smith, "Simple chemical method for forming silver surfaces with controlled grain sizes for surface plasmon experiments," *Langmuir*, vol. 19, pp. 6857–6861, Aug. 2003.

[168] L. Giannuzzi and F. Stevie, "A review of focused ion beam milling techniques for TEM specimen preparation," *Micron*, vol. 30, pp. 197–204, June 1999.

[169] R. E. J. Watkins, P. Rockett, S. Thoms, R. Clampitt, and R. Syms, "Focused ion beam milling," *Vacuum*, vol. 36, pp. 961–967, Nov. 1986.

[170] T. Blom, K. Welch, M. Strømme, E. Coronel, and K. Leifer, "Fabrication and characterization of highly reproducible, high resistance nanogaps made by focused ion beam milling," *Nanotechnology*, vol. 18, p. 285301, June 2007.

[171] B. S. Archanjo, T. L. Vasconcelos, B. S. Oliveira, C. Song, F. I. Allen, C. A. Achete, and P. Ercius, "Plasmon 3D electron tomography and local electric-field enhancement of engineered plasmonic nanoantennas," *ACS Photonics*, vol. 5, pp. 2834–2842, July 2018.

[172] J. M. De Teresa, R. Córdoba, A. Fernández-Pacheco, O. Montero, P. Strichovanec, and M. R. Ibarra, "Origin of the difference in the resistivity of as-grown focused-ion- and focused-electron-beam-induced Pt nanodeposits," *Journal of Nanomaterials*, vol. 2009, p. e936863, Apr. 2009.

[173] G. Rius, "Technology basis and perspectives on focused electron beam induced deposition and focused ion beam induced deposition," *Nuclear Instruments and Methods in Physics Research Section B: Beam Interactions with Materials and Atoms*, vol. 341, pp. 37–43, Dec. 2014.

[174] I. Utke, P. Hoffmann, B. Dwir, K. Leifer, E. Kapon, and P. Doppelt, "Focused electron beam induced deposition of gold," *Journal of Vacuum Science & Technology B: Microelectronics and Nanometer Structures*, vol. 18, no. 6, p. 3168, 2000.

[175] O. Sqalli, I. Utke, P. Hoffmann, and F. Marquis-Weible, "Gold elliptical nanoantennas as probes for near field optical microscopy," *Journal of Applied Physics*, vol. 92, pp. 1078–1083, July 2002.

[176] R. Winkler, F.-P. Schmidt, U. Haselmann, J. D. Fowlkes, B. B. Lewis, G. Kothleitner, P. D. Rack, and H. Plank, "Direct-write 3D nanoprinting of plasmonic structures," *ACS Applied Materials & Interfaces*, vol. 9, pp. 8233–8240, Mar. 2017.

[177] T. Ichimura, S. Fujii, P. Verma, T. Yano, Y. Inouye, and S. Kawata, "Subnanometric near-field Raman investigation in the vicinity of a metallic nanostructure," *Physical Review Letters*, vol. 102, May 2009.

[178] M. Chaigneau, G. Picardi, and R. Ossikovski, "Tip enhanced Raman spectroscopy evidence for amorphous carbon contamination on gold surfaces," *Surface Science*, vol. 604, pp. 701–705, Apr. 2010.

[179] Á. S. Paulo and R. García, "Unifying theory of tapping-mode atomic-force microscopy," *Physical Review B*, vol. 66, p. 041406, July 2002.

[180] B. V. Derjaguin, V. M. Muller, and Y. P. Toporov, "Effect of contact deformations on the adhesion of particles," *Journal of Colloid and Interface Science*, vol. 53, pp. 314–326, Nov. 1975.

[181] H.-J. Butt, B. Cappella, and M. Kappl, "Force measurements with the atomic force microscope: Technique, interpretation and applications," *Surface Science Reports*, vol. 59, pp. 1–152, Oct. 2005.

[182] D. Kiracofe, J. Melcher, and A. Raman, "Gaining insight into the physics of dynamic atomic force microscopy in complex environments using the VEDA simulator," *Review of Scientific Instruments*, vol. 83, p. 013702, Jan. 2012.